International
Progress Report

IPR-07-18

Äspö Hard Rock Laboratory

Core disking study in the TASQ (APSE) tunnel, Äspö HRL

Jonny Sjöberg
Johan Berglund
Vattenfall Power Consultant AB

Diego Mas Ivars
Itasca Geomekanik AB

November 2007

Svensk Kärnbränslehantering AB
Swedish Nuclear Fuel
and Waste Management Co
Box 5864
SE-102 40 Stockholm Sweden
Tel 08-459 84 00
+46 8 459 84 00
Fax 08-661 57 19
+46 8 661 57 19

Äspö Hard Rock
Laboratory

Report no.	No.
IPR-07-18	F86K
Author	Date
Jonny Sjöberg Johan Berglund	November 2007
Checked by	Date
Rolf Christiansson	2008-05-14
Approved	Date
Anders Sjöland	2008-05-21

Äspö Hard Rock Laboratory

Core disking study in the TASQ (APSE) tunnel, Äspö HRL

Jonny Sjöberg
Johan Berglund
Vattenfall Power Consultant AB

Diego Mas Ivars
Itasca Geomekanik AB

November 2007

Keywords: Core disking, Ring disking, Stress measurement, Three-dimensional overcoring, Stress state, Geological modeling, Numerical modeling

Summary

This document reports work conducted to study the phenomenon of core disking and ring disking, in particular in association with overcoring rock stress measurements. Core disking occurs during core drilling in high-stress environments and results in fracturing of the core into disks (perpendicular to the core axis) of varying thickness. Ring disking is the corresponding term for disking of a hollow core, such as that obtained during overcoring rock stress measurements.

The objective of this study was to determine the stress levels at which core disking (solid cores) and ring disking (hollow cores) develop. This was to be achieved by overcoring measurements, supplemented with core drilling, in an area where stress conditions was reasonably well known, in this case the TASQ tunnel at Äspö. In addition to the field work, geological modeling and numerical stress analysis was conducted to aid in explaining field observations.

The conducted field work comprised drilling of four boreholes in the vicinity of deposition hole DQ0063G01. Pilot hole drilling (to obtain hollow cores) was made in all four of these, whereas three-dimensional overcoring measurements were attempted in three boreholes. Practical difficulties and time constraints inhibited additional planned core drilling. Detailed core logging was performed, followed by geological modeling and creating an RVS-model of the test site. The numerical modeling was conducted using the three-dimensional distinct element code *3DEC* /Itasca, 2003/.

The results from this work showed that it was not possible to fulfill the primary objective, i.e., to determine stress levels at which core disking occurs. The reasons for this were: (i) the lack of systematic core disking in the boreholes (only a few, separate, instance of disking observed), and (ii) the practical difficulties in drilling and overcoring, thus achieving only four core holes, and only one, partly successful, stress measurement. However, both this single measurement, and the observed isolated instances of core disking and borehole breakouts indicated low stresses in the test volume. An estimated upper bound of the maximum horizontal stress prior to drilling the holes, and for the majority of the rock mass volume at the test site, was 40–55 MPa. Locally, higher stresses probably exist, as evidenced by the observed core disking and the numerical stress modeling. There also appeared to be a strong link between observed core disking and the occurrence of subvertical fractures intersecting the boreholes. Slightly elevated stresses above and below a fracture coupled with (potentially) weaker rock near the fracture may be a reason for observed core disking.

The destressing of the test volume may be a result of the complex excavation and loading history of the APSE test area. The heterogeneous geology, and in particular the presence of subvertical fractures, influence the stress distribution making it more discontinuous. Together, these two factors may cause lower, and more varying, stresses in the test area, than originally anticipated. However, the governing mechanisms cannot be fully explained given the currently available data. The numerical modeling conducted could not capture the full stress-path history of the test site, and its effect on

the rock. It is believed that to do so, a model that can replicate possible permanent effects of reaching the rock strength (i.e., a plastic type of constitutive model) must be employed and all stages in the excavation-loading must be modeled. Even so, it may not be possible to describe all rock observations using a single numerical model.

Any further work along these lines must focus on achieving as low variability as possible in the factors controlling core disking. This means homogeneous geology with as few fractures as possible, well-defined stress conditions and simple stress-path history, better drilling control, and the ability to drill more tests holes and conduct more measurements (to achieve redundancy in the results). Detailed planning is essential and detailed numerical modeling, using both linear-elastic and plastic constitutive models should be carried out prior to the field work, and as an input into planning of hole locations.

Sammanfattning

I denna rapport presenteras en studie s k "disking" av borrkärnor, med särskild inriktning mot de fall då detta uppkommer i samband med överborrningsmätningar. "Disking" uppkommer vid kärnborrning under höga spänningar och resulterar i att borrkärnan sprickor upp i tunna skivor (vinkelrätt kärnans axel) med varierande tjocklek. S k "ring disking" är motsvarande fenomen för ihåliga (överborrade) kärnor, d v s av den typ som erhålls vid spänningsmätningar med överborrningsmetoden.

Målet med denna studie var att bestämma vid vilka spänningsnivåer som "disking" i olika former uppkommer. Detta skulle åstadkommas via överborrningsmätningar, kompletterade med kärnborrning, i ett område där spänningsförhållandena var relativt väl kända. I detta fall valdes TASQ-tunneln vid Äspö HRL för detta arbete. Förutom fältarbeten, har geologisk modellering och numerisk spänningsanalys utförts i syfte att förklara fältobservationerna.

Fältarbetet omfattade borrning av fyra hål i närheten av depositionshål DQ0063G01. Pilothålsborrning (för att erhålla ihåliga kärnor) utfördes i alla fyra, medan tredimensionella överborrningsmätningar gjordes i tre av borrhålen. Praktiska svårigheter och tidsbegränsningar omöjliggjorde ytterligare borrningar. Detaljerad kärnkartering utfördes, följt av geologisk modellering och skapandet av en RVS-modell över testområdet. Numerisk modellanalys utfördes med den tredimensionella distinkta-element koden *3DEC* /Itasca, 2003/.

Resultaten från denna studie visade att det inte var möjligt att uppfylla det primära målet med projektet, nämligen att bestämma spänningsnivån vid vilken "disking" uppkommer. Orsakerna till detta var: (i) avsaknaden av systematisk "disking" i borrhålen (endast ett fåtal isolerade observationer), samt (ii) de praktiska svårigheterna vid borrning och överborrningsmätningar vilket ledde till att endast fyra hål borrades och endast en, delvis lyckosam, spänningsbestämning erhölls. Både denna enstaka mätning samt de få observationerna av "disking" och skador i borrhålsväggarna visade dock på låga spänningar i testområdet. En uppskattad övre gräns för största horisontalspänningen innan borrning av hålen, och för huvuddelen av bergmassan, är 40–55 MPa. Lokalt uppkommer högre spänningar, vilket både observerad "disking" och den numeriska spänningsanalysen visat. Det förefaller också finnas en stark koppling mellan observerad "disking" och förekomsten av subvertikala sprickor som går igenom borrhålen. Observerad "disking" kan möjligen förklaras av lokalt högre spänningar ovan och under dessa sprickor, tillsammans med (möjligen) något svagare berg nära sprickorna.

Avlastningen av testområdet kan ha orsakats av den komplexa uttags- och lasthistoriken i APSE-området. Den heterogena geologin, framförallt närvaron av subvertikala sprickor, medför en mer diskontinuerlig spänningsfördelning. Tillsammans ger dessa två faktorer lägre (än förväntat), och mer varierande, spänningar i testområdet. De styrande mekanismerna kan dock ej förklaras helt med hjälp av befintlig information. Den numeriska spänningsanalysen kunde inte återskapa spänningshistoriken i testområdet och hur detta kan ha påverkat berget. För att kunna göra detta krävs en

mopdell där eventuella permanenta effekter till följd av att bergets hållfasthet uppnås kan simuleras (d v s en plastisk typ av konstitutiv modell) samt att alla steg i uttags- och lasthistoriken simuleras i modellen. Det kan även för detta fall visa sig vara svårt att kunna beskriva alla observationer med en modell.

Eventuella fortsatta arbeten av denna typ måste utgå ifrån så konstanta förhållanden som möjligt, vad gäller de faktorer som påverkar uppkomsten av "disking". Detta betyder homogen geologi med så få sprickor som möjligt, väl definierade spänningsförhållanden och enkel lasthistorik, bättre borrning, samt möjlighet att borra fler hål och göra fler spänningsmätningar (i syfte att erhålla redundans i resultaten). Detaljerad planering är nödvämndig och numerisk modellanalys med såväl linjärelastisk som plastisk konsitutiv modell bör utföras före eventuellt fältarbete, som stöd vid planering av hållägen.

Contents

1 Introduction

This document reports work conducted to study the phenomenon of core disking and ring disking, in particular in association with overcoring rock stress measurements. Core disking occurs during core drilling in high-stress environments and results in fracturing of the core into disks (perpendicular to the core axis) of varying thickness. Ring disking is the corresponding term for disking of a hollow core, such as that obtained during overcoring rock stress measurements.

Both core disking and ring disking has been observed within the site investigation program of SKB, most notably at the Forsmark site. This has posed to be a limitation of the applicability of overcoring stress measurements, as the measurement results are no longer reliable once disking is occurring. In extreme cases, it is not possible to take any measurements at all, due to severe ring disking, see Figure 1-1.

Figure 1-1. *Example of ring disking observed during overcoring rock stress measurements in borehole KFM01B (test no. 2:10:1 at 474.25 m depth) /Lindfors et al., 2005/.*

The *in situ* stress state remains, however, a key question for the siting and design of a repository for spent high-level nuclear fuel. A more in-depth study of occurrence of core disking, under controlled conditions, would help to quantify at what stress levels both core disking and ring disking develops. Such knowledge would provide additional quantitative stress data for the site investigation, and thus increase the reliability in a subsequent stress model. The present work was planned with this background, and with the notion of combining: (i) field observations of disking, (ii) overcoring stress measurements, (iii) geological modeling, and (iv) numerical modeling, to increase the knowledge of the conditions governing core and ring disking, with particular focus on stress levels.

2 Objective and scope

The primary objective of this work was to determine the stress levels at which core disking (solid cores) and ring disking (hollow cores) develop. This was to be achieved by overcoring measurements, supplemented with core drilling, in an area where stress conditions was reasonably well known, in this case the TASQ tunnel at Äspö, which was also the location for the APSE (Äspö Pillar Stability Experiment) project /Andersson, 2004, 2007/. The work comprised drilling short (5–6 m) boreholes at various distances (corresponding to different stress levels) from the deposition holes in the TASQ tunnel, thereby establishing the limits of core and ring disking. Such results would then be useful for interpreting observations of core disking and ring disking at other sites, most notably regarding the site investigation program at the Forsmark site.

As the work progressed, it became evident that interpretation of disking observations and conducted stress measurements were far from straightforward. An additional objective was thus formulated. The secondary goal of the work was to help explain the occurrence (or lack) of disking through a detailed geological model coupled with numerical modeling of the test area.

The work comprised core drilling (solid cores), overcore drilling (hollow cores), three-dimensional overcoring stress measurements, detailed core logging, geological modeling and creating an RVS-model, and numerical stress modeling. The overall strategy of the work, including method descriptions are given in Chapter 3. The geological modeling is described in more detail in Chapter 4.

All stress measurements were conducted using the three-dimensional *Borre* probe for overcoring (developed and used by Vattenfall Power Consultant AB). The method is described in detail in /Sjöberg & Klasson, 2003/. Field measurements were done during the period of January 16 to February 9, 20006. Core drilling and overcore drilling was conducted during the same field period. The results from this work are presented in Chapter 5.

The numerical modeling was conducted using the three-dimensional distinct element code *3DEC* /Itasca, 2003/ and is further described in Chapter 6. Finally, the combined results are discussed in Chapter 7, and summary conclusions, as well as recommendations are presented in Chapter 8.

All stresses presented in this report are denoted using a geomechanical sign convention with compressive stresses taken as positive, with the exception of stress plots from *3DEC*, where compressive stresses are negative. Compressive strains are, however, defined as negative (in overcoring strain records).

3 Strategy,test plan and execution

3.1 Background

The basic idea pursued in this project was to drill core holes in a high-stress environment, thus forcing core and/or ring disking to occur. Subsequently, overcoring stress measurements were to be conducted in locations where disking did not occur (where stresses were believed to be just below the limit of causing disking), thus enabling a quantification of the stress level at which disking develops. This would also enable comparisons with existing criteria, e.g., /Hakala, 1999a, 1999b/ for estimating stresses based on core disking observations.

The APSE test site (in the TASQ tunnel at Äspö HRL) provided an opportunity for conducting such a study. At this site, two deposition holes, each 1.8 m in diameter and with a 1 m rock pillar between the hole edges, have been drilled in the curved tunnel floor, to study spalling failure in hard rock (Figure 3-1). This work is described in detail in /Andersson, 2007/.

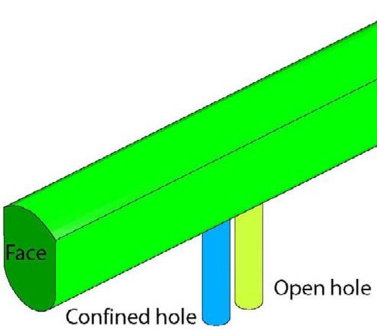

Figure 3-1. *Schematic figure showing test geometry of the APSE site, Äspö HRL /Andersson, 2007/.*

The curved tunnel floor, and the excavation of the two deposition holes, provides a rock volume with elevated stresses (as verified in Andersson, 2007), but also with high stress gradients as stresses decrease with increasing distance from the deposition holes. Thus, it would, in theory, be possible to find areas where both extensive core disking would develop (highest stresses) to areas with only ring disking (intermediate stresses), and finally areas with no disking at all (lowest stresses). Existing numerical modeling results could be used to estimate stresses beforehand, thus enabling boreholes to be located at positions where core disking and ring disking was to be expected.

3.2 Plan for field tests

The test site is schematically shown in Figure 3-2. It was decided to conduct the core disking tests near deposition hole DQ0063G01, since this provided easy access and stresses were deemed to be slightly higher in this area /Andersson, 2007/. A test hole (named KQ0062G01) was drilled in close proximity of this deposition hole. The location of the test hole, as well as the geometry of the test site is shown in Figure 3-3.

The recovered core showed core disking in one side of the core at approximately 2.25–2.70 m depth. Disks with a thickness of around 10 mm were observed, which was taken as a verification that disking was likely to occur also in other boreholes, and a decision was made to move on with the project.

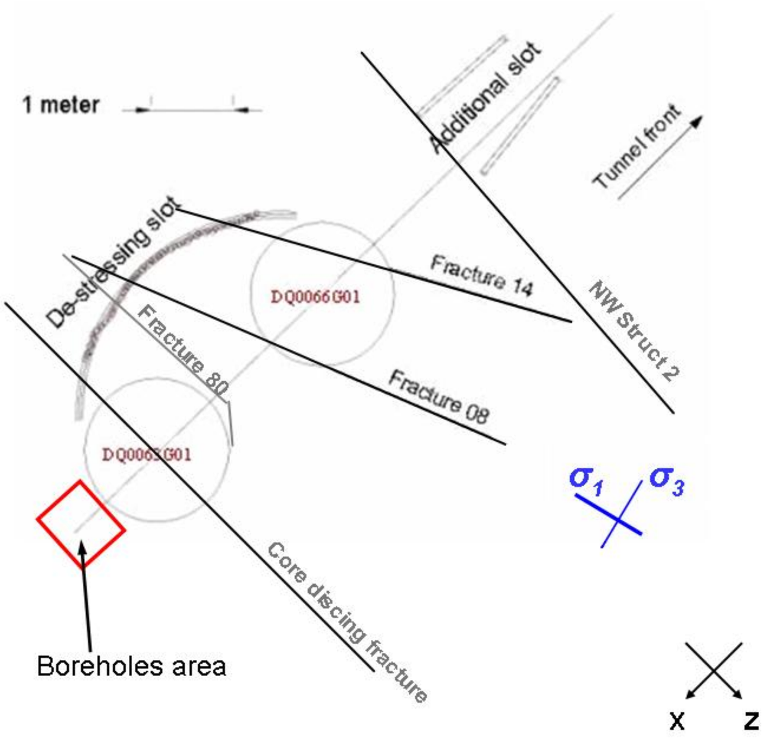

Figure 3-2. *Schematic plan view of test site, showing deposition holes ad mapped fractures as of 2005 (prior to this study).*

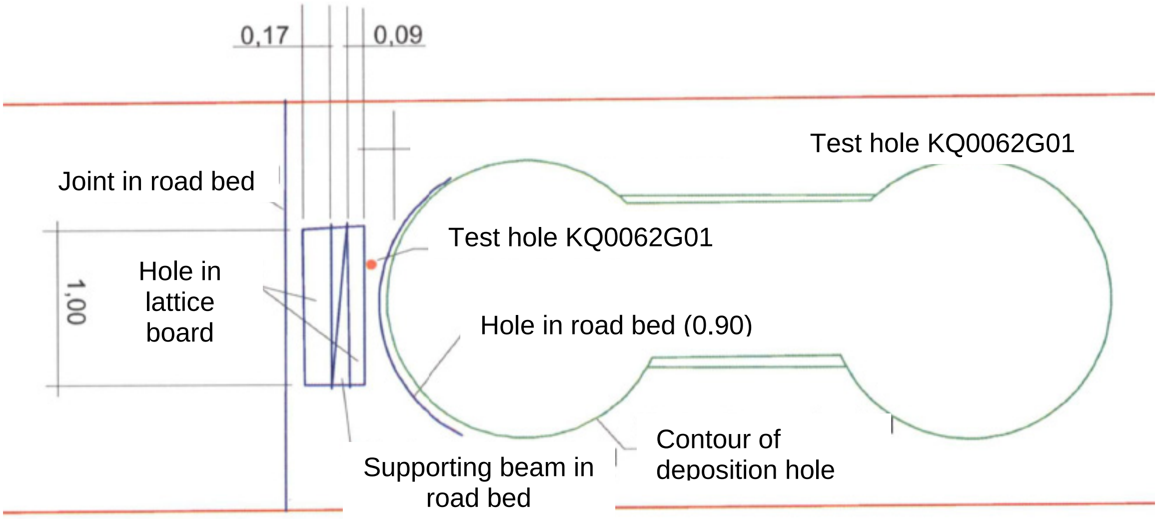

Figure 3-3. *Geometry of test site and location of first test hole (KQ0062G01).*

To be able to assess the stress levels beforehand, numerical modeling results were reviewed. An existing continuum model (no fracture slip allowed) in *3DEC* /Itasca, 2003/ conducted by /Mas Ivars, 2006/ was used. The situation after drilling the destressing slot and removing the pillar between the two deposition holes, was modeled. The calculated stresses were used to select hole locations. Using the stress criteria for core and ring disking proposed by /Hakala, 1999a, 1999b/ as a starting point, and comparing these with the observed disking in the test hole, it could be assumed that core disking (in solid cores) could be expected in an area where the major principal stress was higher than 75 MPa, see Figure 3-4. The high-stress area is relatively limited, but the high-stress zone is larger around deposition hole DQ0063G01, which indicates that the field work should focus on this area. Practical restrictions limit the available area to a width of 0.90 m at a distance of 0.40 to 1.0 m from the edge of the deposition hole (see Figure 3-4). Proposed hole locations are shown in Figure 3-5 and Figure 3-6. Holes were located so as to reduce stress interference between boreholes; thus, a minimum center-to-center distance of 270 mm (for 76 mm hole diameter) was used, corresponding to 2.5 times the hole diameter between hole edges.

An example of calculated stresses along the position of the first planned hole (named A1) is shown in Figure 3-7. The calculated maximum stresses at the location of the above holes is between 65 and 75 MPa, discarding the upper 1 m, as this portion in reality is believed to be destressed /Andersson, 2007/. Using the nomograms of /Hakala, 1999b/, this was judged sufficient to cause systematic core disking along the borehole, see also Figure 3-8. Here it has been assumed that core disking is caused by pure tensile failure, and that continuous, homogeneous, linear-elastic and isotropic conditions (up to the point of failure) apply. Furthermore, one principal stress is assumed to be aligned with the borehole, Poisson's ratio is set to 0.25, and the tensile strength is 15 MPa /Andersson, 2004, 2007/, see also Table 4-3. The vertical stress is around 20 MPa along borehole A1, and the minimum horizontal stress generally about the same, or slightly lower. Given this, core disking with an estimated thickness of between 8 and 10 mm should be expected (Figure 3-8). This is similar to the actual disk thickness observed in the test hole. The lowest stresses at 3 m depth are 40–50 MPa, which should be low enough that overcoring measurements are possible at, or below, this depth.

Since stresses along the borehole gradually decreases with increasing hole depth, the strategy for drilling was to first drill solid cores to a depth at which core disking no longer occurred, followed by hollow core drilling to a depth at which no longer ring disking occurred. Below this depth, overcoring rock stress measurements were to be performed. It is assumed that these three activities can be conduced within a zone of similar stress conditions and geology.

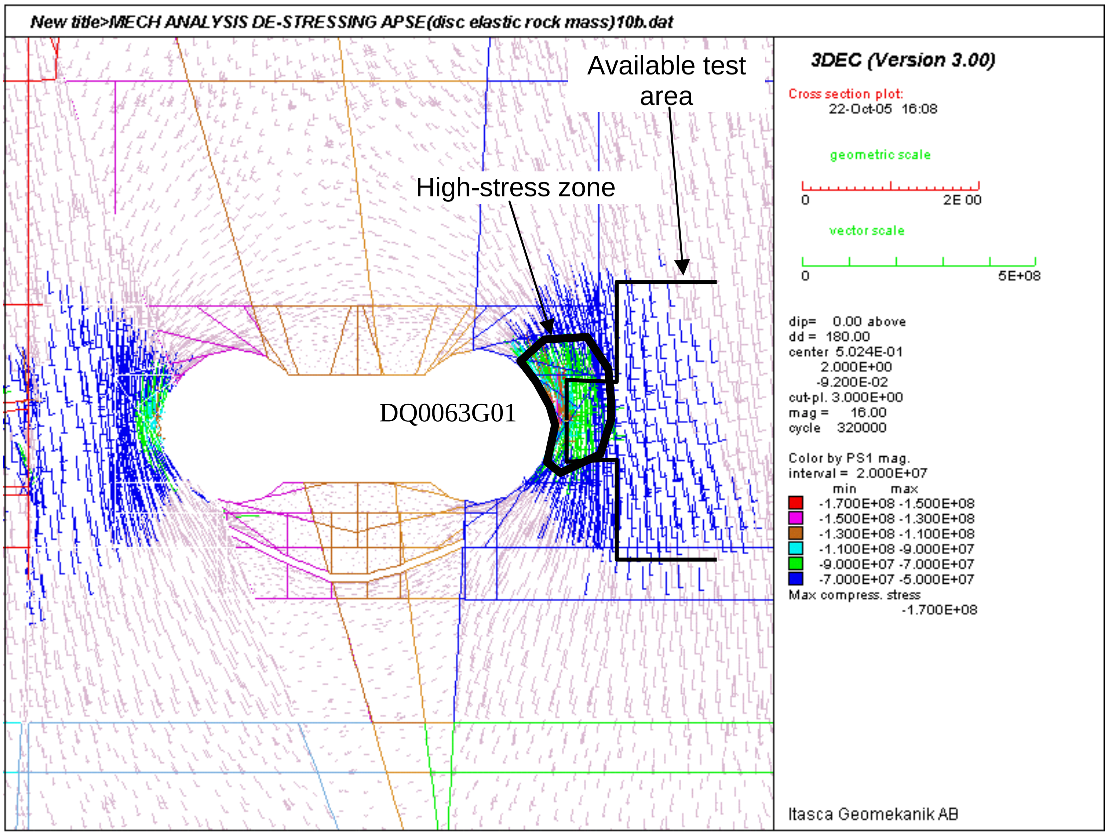

Figure 3-4. *Example of calculated stresses around deposition holes. Horizontal section at 1 m depth (below tunnel floor) showing projections of the principal stress vectors, colored with respect to magnitude of the major principal stress.*

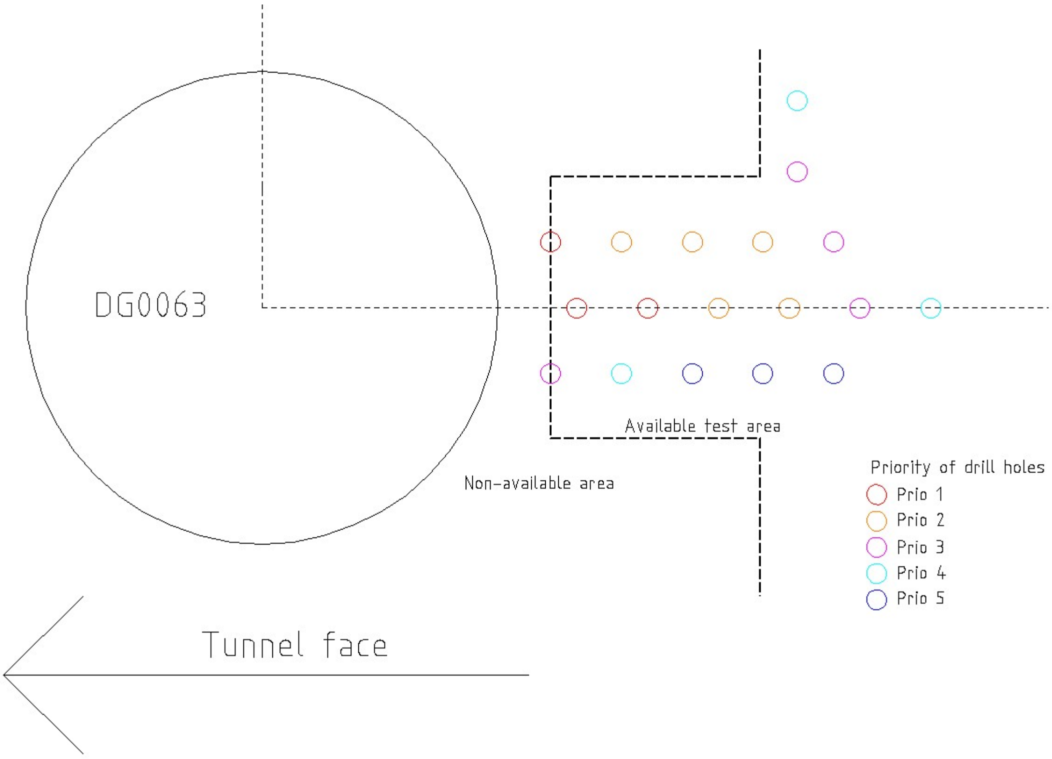

Figure 3-5. *Proposed hole locations for core disking study (holes colored by priority).*

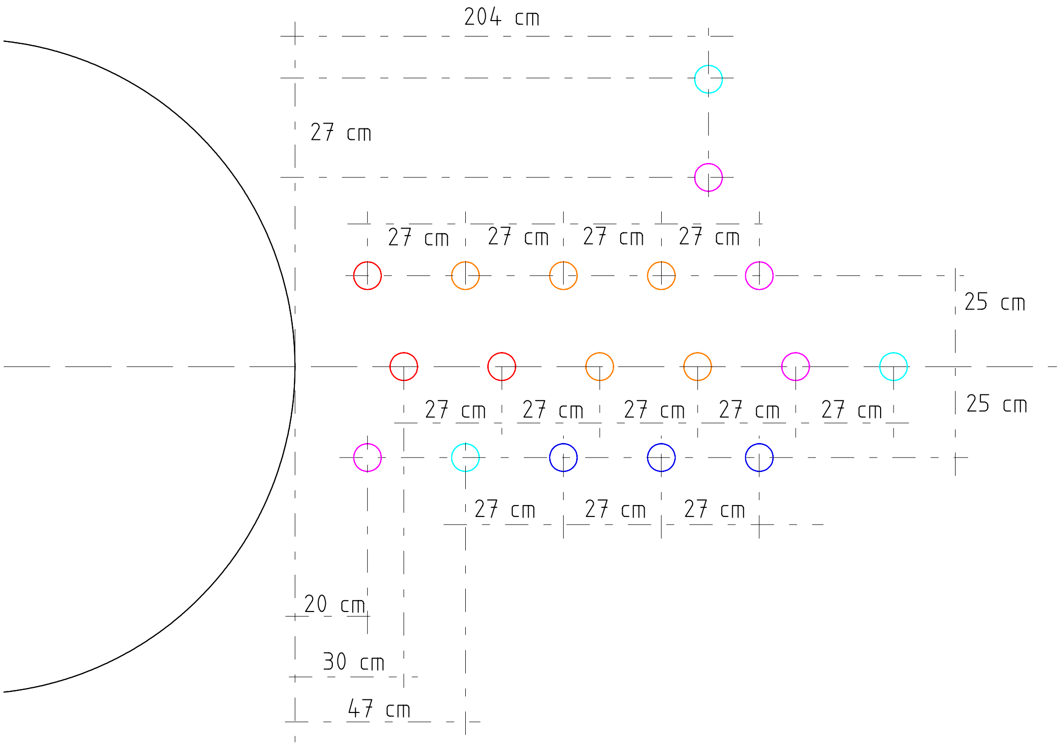

__Figure 3-6.__ Proposed hole locations and distances for core disking study (holes colored by priority).

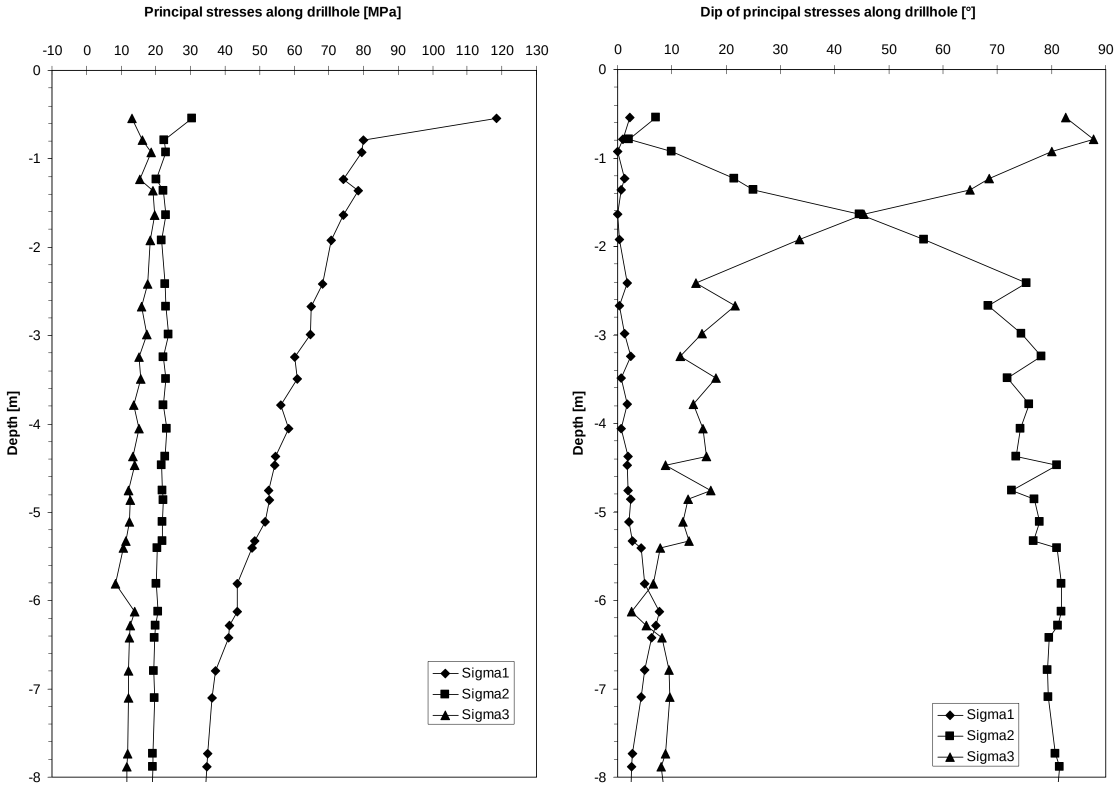

__Figure 3-7.__ Calculated principal stresses (from 3DEC model) along the position of the first planned borehole in the test area (A1, cf. Figure 3-5). It should be noted that calculated stresses are before holes are drilled (along the centerline of the proposed hole location).

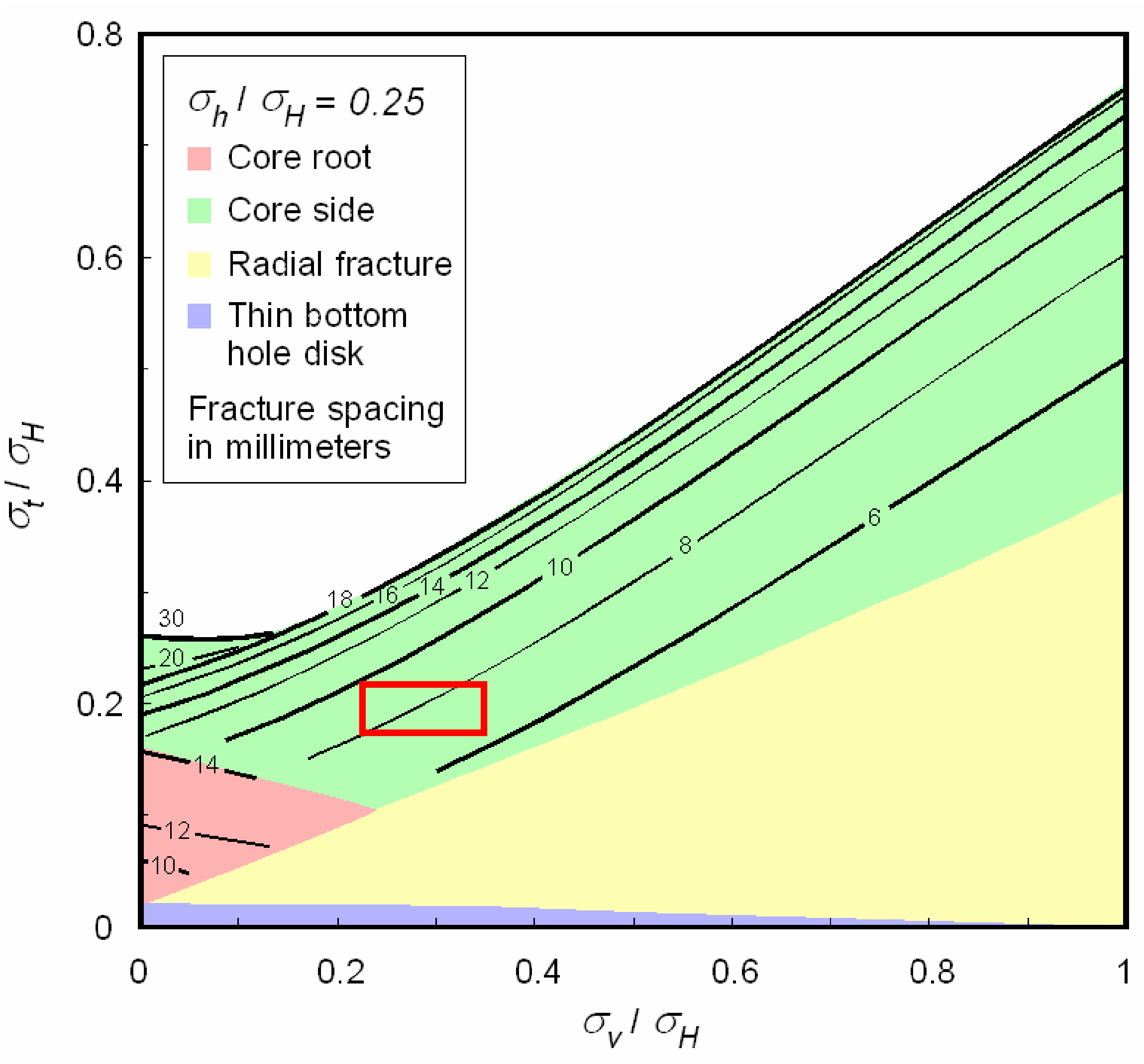

***Figure 3-8.** Estimation of core disking (solid core) potential based on calculated stresses along borehole A1 (cf. Figure 3-5 and Figure 3-7). The red box shows the range of anticipated disk thickness in this borehole, based on assumed values on in situ stress and tensile strength.*

Ideally, five to six holes should be drilled to a depth at which solid core disking no longer occurred. These should be spread out in the area to capture possible geological variations. Subsequently, selected holes should be lengthened using overcoring drilling (hollow cores), and finally, overcoring stress measurements conducted in some of these. However, this would require several re-locations of the drill rig with associated problems of aligning the rig to the exact same position at a drilled hole. An alternative procedure was adopted in which all three moments are conducted in one hole, before re-locating the drill rig. Each borehole is drilled in short extensions (0.5 to 1.0 m at a time) to record, as closely as possible, changes in disking behavior. The priority in which the holes were to be drilled is indicated in Figure 3-5 and Figure 3-6 (based on calculated stresses). Obviously, this priority may change as results are obtained. At least one successful overcoring measurement should be attempted in each hole. It should also be noted that the geology in the test area is not homogeneous. Fractures, dikes and local zones of ductile deformation structures, which may affect the results.

3.3 Drilling, core logging, and overcoring stress measurements

3.3.1 Field conditions and conducted work

Core drilling was conducted with a drill rig supplied by a contractor of SKB. Practical problems prevailed, in particular during overcoring drilling, as sufficient feed force could not be obtained. The rig was bolted to the tunnel floor, but on several occasions, bolts were pulled out during overcoring drilling. While this made the practical work more difficult, it is not believed to have influenced the results with respect to core disking observations, to any significant degree. However, it is possible that the drill rig problems may have influenced the results of the overcoring measurements. A photo of the test site is shown in Figure 3-9.

Due to the practical difficulties and time constraints for the work (other activities planned in the TASQ tunnel), only four boreholes were drilled. Pilot hole drilling (to obtain hollow cores) were made in all four of these, whereas overcoring measurements were attempted in three boreholes, see Figure 3-10. It should be noted that the original, preliminary, hole names, were supplemented with official hole names for Äspö HRL.

In general, the amount of disking observed was much less than anticipated in all core holes. No systematic core disking (over long stretches) was observed, and no ring disking at all occurred. This finding necessitated additional work in geological modeling and numerical stress modeling, as described below.

3.3.2 Core logging

Preliminary core logging was conducted in the field, immediately after holes were drilled. This focused on the occurrence of disking, including an overview of the salient geological conditions. Additional core logging was then conducted at two occasions: (i) a preliminary geological logging approximately two weeks after completed field work, and (ii) a detailed Boremap logging of all cores. BIPS imaging of the boreholes were also made to supplement core logging. This also enabled a rough assessment of possible borehole damage (so-called borehole breakouts).

Moreover, a simple video camera was used in order to try to get a visual view of water seepage into the boreholes. The video photography was conducted during the overcoring campaign. The VHS tapes from the video recordings were analyzed in conjunction with the visualization of fractures.

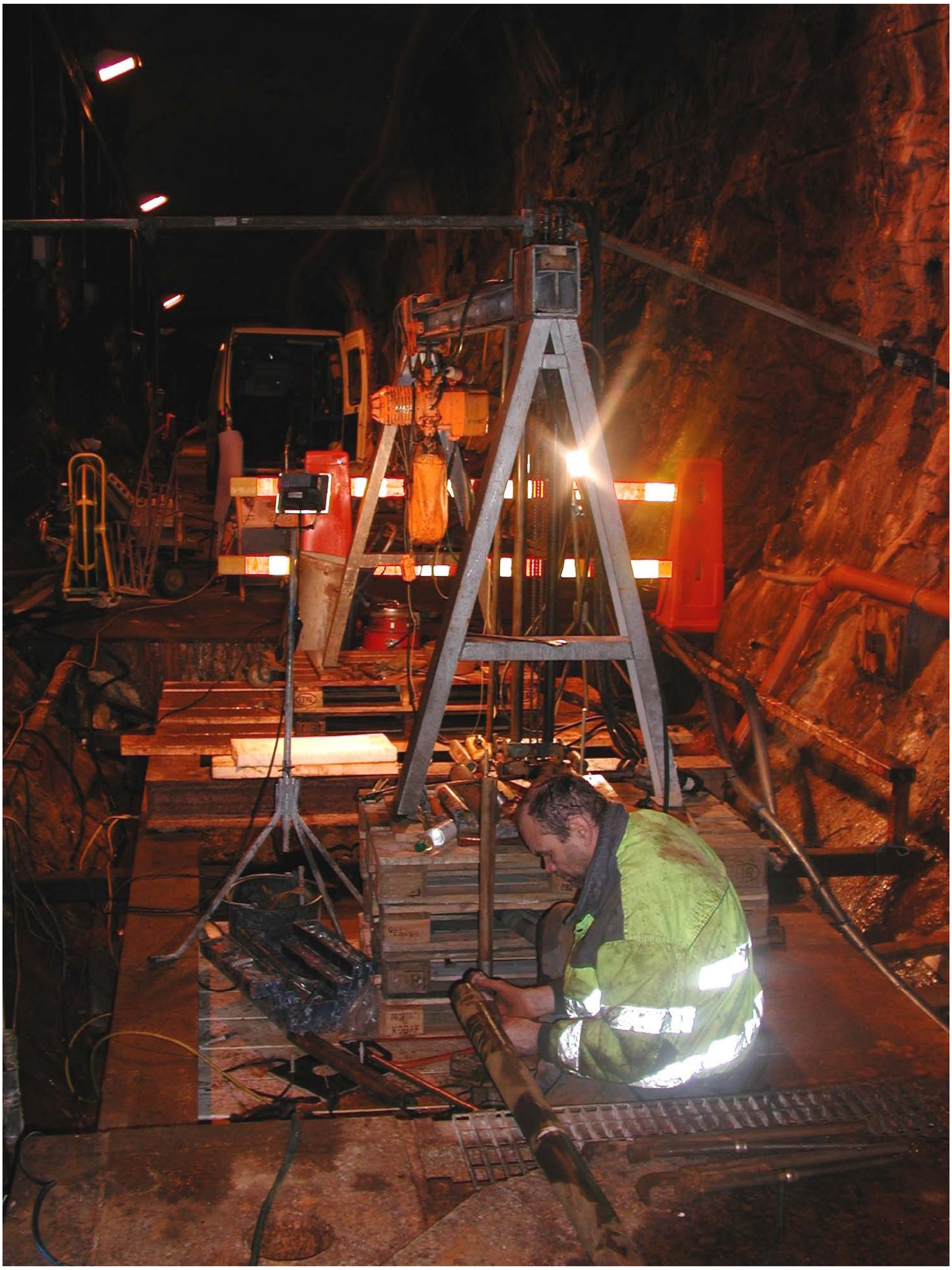

***Figure 3-9.** Photo of test site.*

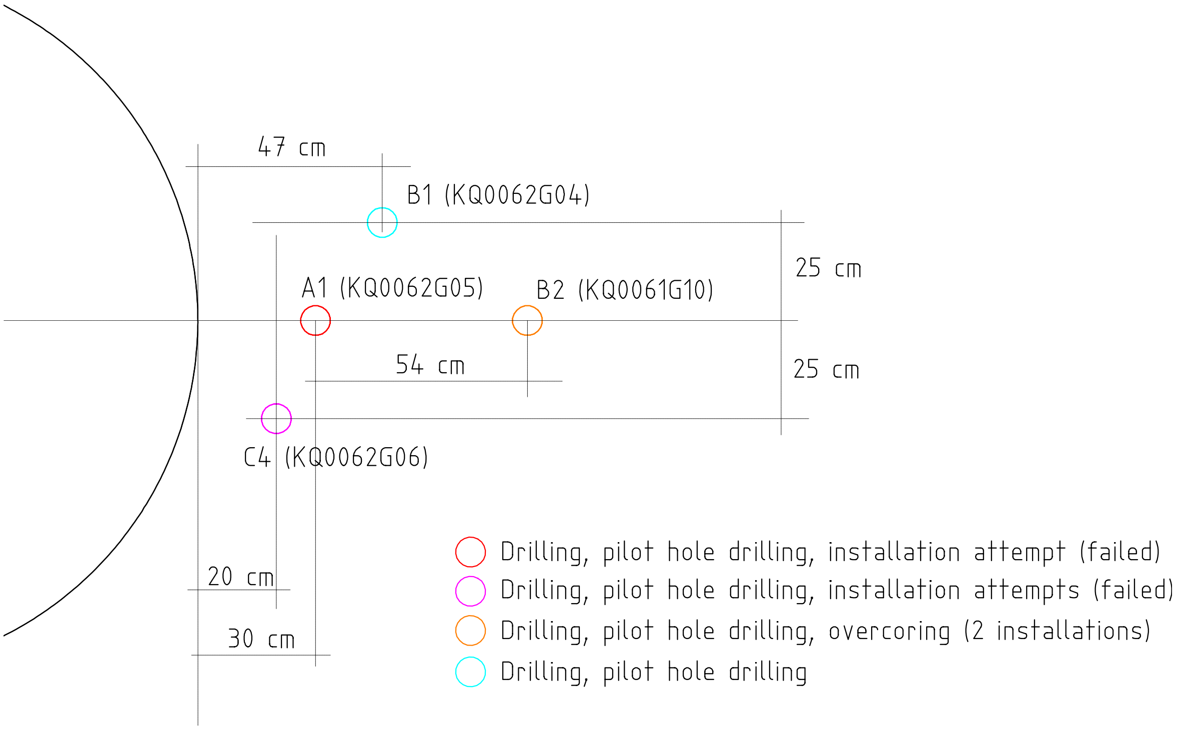

Figure 3-10. *Results of core drilling and overcoring stress measurements.*

3.3.3 Overcoring stress measurements

Measurement procedure

Overcoring stress measurements were conducted using the three-dimensional *Borre* probe for overcoring /Sjöberg & Klasson, 2003/. Measurements were conducted in accordance with extensive quality operating procedures for the method used, see also SKB MD 181.001 (SKB internal controlling document). Briefly, the measurement procedure consists of: (i) drilling a pilot hole at the designated measurement position, (ii) inspecting the pilot core and deciding on installation (fracture-free rock), (iii) attaching strain gauges, programming data logger, and installing probe into pilot hole (Figure 3-11), (iv) allowing glue to cure, (v) overcoring and measuring resulting strains, (vi) retrieving core to surface and conducting biaxial testing (Figure 3-12) to determine elastic constants, and (vii) stress calculation using recorded strains and elastic constants.

Calculation of stresses is carried out using another in-house developed *Microsoft Excel* application, with input in the form of strain differences, values on elastic constants, and borehole and recorded strain gauge orientation from the probe installation. The stress calculations are based on the theory presented by /Leeman, 1968/.

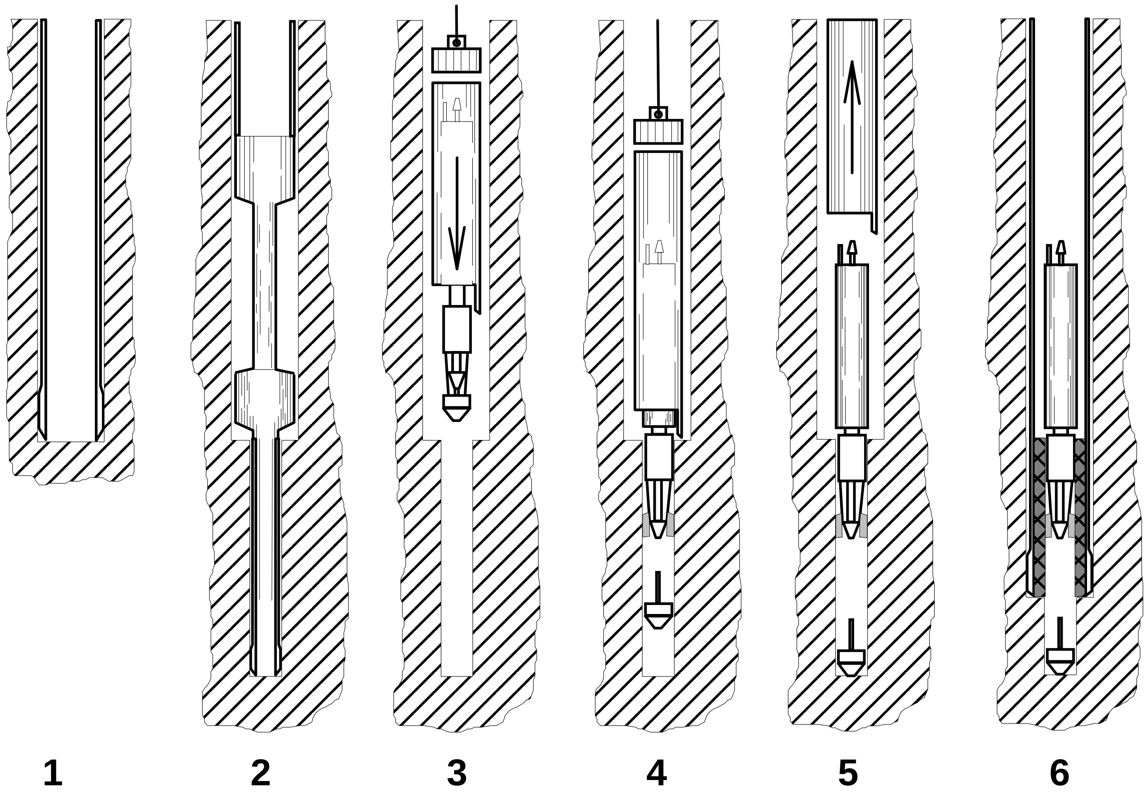

Figure 3-11. *Installation and measurement procedure with the Borre probe /Sjöberg & Klasson, 2003/:*

1. *Advance 76 mm-diameter main borehole to measurement depth. Grind the hole bottom using the planing tool.*
2. *Drill 36 mm-diameter pilot hole and recover core for appraisal. Flush the borehole to remove drill cuttings.*
3. *Prepare the Borre probe for measurement and apply glue to strain gauges. Insert the probe in installation tool into hole.*
4. *Tip of probe with strain gauges enters the pilot hole. Probe releases from installation tool through a latch, which also fixes the compass, thus recording the installed probe orientation. Gauges bonded to pilot hole wall under pressure from the nose cone.*
5. *Allow glue to harden (usually overnight). Pull out installation tool and retrieve to surface. The probe is bonded in place.*
6. *Overcore the Borre probe and record strain data using the built-in data logger. Break the core after completed overcoring and recover in core barrel to surface.*

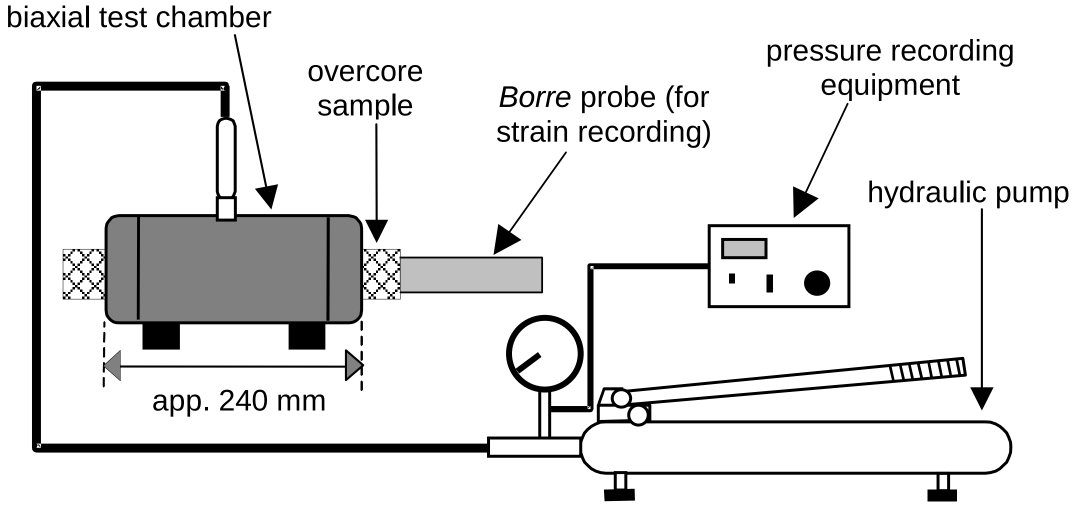

Figure 3-12. *Schematic drawing of the biaxial load cell with pressure generator and recording equipment.*

Data analysis

The *Borre* probe is a "soft" stress cell, which means that the stiffness of the strain gauges is negligible in comparison to the stiffness of the rock. Thus, only the strains induced by overcoring and the elastic constants of the rock, in addition to the orientation of the probe in the borehole (including borehole orientation), are required to determine the complete stress tensor. Calculation of stresses from strain is done under the assumption of continuous, homogeneous, isotropic, and linear-elastic rock behavior /Leeman, 1968/. The stress relief is identical in magnitude to that produced by the *in situ* stress field but opposite in sign.

The analyses of obtained test data comprise (i) analysis of overcoring strain data, (ii) analysis of biaxial test data, and (iii) stress calculation, using data from the first two tasks. For each task, quality control checks and data assessments are included. Detailed descriptions of each step are given in SKB MD 181.001 (SKB internal controlling document), and are briefly summarized below.

The recorded strain gauge response and temperature are plotted vs. recorded time, and the strain differences due to overcoring and stress relief are calculated for each strain gauge for later use as input to the stress calculation. The overcoring strain change is normally determined as the difference between (i) recorded strain after completed overcoring with flushing on, and (ii) recorded strain at the start of overcoring with flushing on. It is important that all conditions, except the overcoring stress relief itself, are as similar as possible for these two instances (e.g., flushing, water pressures, temperatures, etc.). Furthermore, the strain values should be stable (little or negligible strain drift) at these instances. In some cases, stable and ideal strain response can be observed during the first portion (typically 20-30 cm) of the overcoring process, whereas significant strain drifts occur during the rest of the overcoring. In theory, practically all of the strain relief takes place during the first 24 cm of overcoring (with gauge positions at 16 cm), see e.g., /Hakala et al., 2003/. For such cases, strain differences may be determined from stable values of this portion of the strain response curve (corresponding to approximately 20–30 cm drill bit position or more). However, temperature effects (heating of the rock due to drilling) are more prevalent at this stage, which must be considered. It should also be noted that small changes in strains (a few μstrains), which may arise from choosing slightly different start- and stop-times for the overcoring, have very small influence on the calculated magnitudes and orientations of the *in situ* stress state.

Recorded strain and pressure data from biaxial testing are plotted and examined. Elastic constants are determined from recorded strain and pressure data from the biaxial testing. For this, the theory for an infinitely long, thick-walled circular cylinder subjected to uniform external pressure is employed (see e.g., KTH, 1990). Since the *Borre* probe incorporates three pairs of circumferential and axial strain gauges, three pairs of elastic property-values are obtained from each biaxial test. The aim is to obtain rock parameters that apply to the relaxation experienced by the rock during overcoring. Therefore, the values of E (Young's modulus) and ν (Poisson's ratio) are taken to be secant values, calculated from strain data obtained during unloading of the core specimen. Usually, the secant values between the pressures of 8 and 3 MPa are calculated and averaged for the three strain rosettes. However, elastic constants may be calculated for other pressure intervals, if recorded strain readings are significantly unstable and/or display notable non-linearity for certain pressures.

Calculation of stresses from measured strains is based on the classical theory by /Leeman, 1968/. The details of the formulation can also be found in e.g., /Amadei & Stephansson, 1997/ and are not repeated here. Strain measurements from at least six independent directions are required to determine the stress tensor (which has six components). When all nine gauges of the *Borre* probe function properly during a measurement, redundant strain data are obtained. A least square regression procedure is used to find the solution best fitting all the strain data, from which the stress tensor components are calculated. For each test, one tangential or inclined gauge and/or two axial gauges may be rejected or recalculated without impairing the determination of the stress tensor. Recalculation is only performed if evidence of malfunctioning gauges exists, see also /Sjöberg & Klasson, 2003/ and SKB MD 181.001 (SKB internal controlling document). Subsequently, the magnitude and orientation vector of each of the three principal stresses are calculated, as well as the stresses acting in the horizontal and vertical planes.

For the case of several measurements on one test level, the mean stress state is calculated. This is conducted by first taking the stress tensor components for each of the measurements (defined in a common coordinate system, e.g., the site coordinate system), and averaging each of the stress tensor components. From these mean values, the mean principal stresses, as well as the mean horizontal and vertical stresses, are determined. Thus, the primary data reported from the overcoring stress measurements are:

- magnitudes of the three principal stresses;
- orientations of the three principal stresses (bearing and dip);
- magnitudes and orientations of the stresses acting in the horizontal and vertical planes; and
- values on elastic constants from biaxial testing.

3.4 Geological modeling

3.4.1 Aim and scope

The aim of the geological study was to:

1. Compile the geological information mapped in the tunnel, deposition holes, pillar, and boreholes drilled in this area.
2. Visualize the geology in the area.
3. Create a model of geological structures relevant for the stress situation in the area.

The model was done in the local, "Äspö96" coordinate system, which has been used at Äspö HRL since the start. Coordinates may, however, be exported from RVS to other coordinate systems as well.

The model boundaries (Table 3-1) were chosen to incorporate the deposition holes, the boreholes drilled for stress measurements and the closest surroundings.

Table 3-1. Model boundaries.

Model boundary	Easting	Northing	Elevation	Extent (m)
Origin	2115.000	7310.000	-455.000	
dx	2135.000			20
dy		7330.000		20
dz			-435.000	20

Existing RVS-models at the –450 level were used as background models during start-up of the modeling work. These were:

- Geomod 2002, latest full-scale model at Äspö HRL, covering regional, local major and local minor deformation zone.
- APSE-model, which is the model created prior to the excavation of the APSE tunnel (=TASQ tunnel). Covering both deformation zones and larger fractures.
- Update on the –450 level. Ongoing work that aims to analyze and update the hydraulic structures in the lower parts of Äspö HRL. Include a compilation of small-scale models concentrated around separate project areas at these levels. Only these latter where used here.

3.4.2 Visualization

The mapping of tunnel sections (in TMS, the Tunnel Mapping System), the TASQ tunnel, the deposition holes (KQ0063 and KQ0066) and the pillar wedge has been draped on the theoretical tunnel geometry in 3D. The objects (fractures and lithological boundaries) all have the same color in these visualizations. A light blue color is used for the tunnel objects, a dark blue for the deposition holes and black is used for the pillar wedge. During modeling a connection to the TMS database made it possible to get information on the characteristics of each object.

The visualization of fractures in cored boreholes has been done by representing them by slightly exaggerated, planar spherical discs, centered at the position of each mapped fracture. Fractures interpreted (in the Boremap system) to have an aperture were color coded so that fractures dipping 0-45° are green and steeper fractures are light blue in color, see also Figure 3-13 for legend.

The same kind of visualization was done for structural measurements, i.e., foliations, including regional foliation and shear zone related foliations. These were visualized in the point where they were measured during mapping.

Lithology ("Rock Type" and "Rock Occurrences") was visualized as narrow cylinders in specific colors along the borehole. Cylinders with wider diameter were used for sections mapped as Sealed Network (brown color), Core Loss (black), Crushed rock (grey) and core disking (yellow). The upper contact of each rock occurrence was accompanied by visualization of the orientation of the contact by a spherical disc. It should be noted that most core losses correspond to mechanical planning made during the overcoring tests.

Often, sealed fractures are geometrically complex, as they splay and undulate. When individual fractures cannot be fitted to planar surfaces in the mapping system, sealed fracture network is an alternative. Sealed networks are mapped in sections of the core, with average piece length and the two most common fracture orientation given. Such sections are visualized as brown cylinders along the borehole and with average orientation as brown discs in their centre.

Analysis of video photography from the boreholes showed that the quality of the video images was generally rather poor and although a few seepages are seen it is normally difficult to pinpoint the exact location of these. At a few locations, however, it was considered probable that a correlation between image and visualized fracture could be made with a reasonable high confidence. These water-bearing fractures are visualized in the model as larger dark blue, spherical discs.

3.4.3 Modeling

The modeling of the geological structures was done as an iterative process. Geology considered to be of importance for the local stress situation was marked up by using the "Fracture Observation" tool in RVS, visualized as circular discs. By small adjustment of size and orientation of these it was possible to interpolate between observations at different locations in the 3D model volume space, in order to estimate the probability of correlation. In this manner a confidence was achieved when relating separate observation to a specific geological object. However, since geological objects only rarely are planar over longer distances a certain degree of uncertainty still exists for modeled objects.

All modeled objects are modeled as planar surfaces with zero thickness. They terminate either at the model boundary or against another modeled object. Obviously, this is a significant simplification from what is generally found in the field, where every fracture and most other geological objects have at least a slight irregularity, have variable thickness with variable mineral infilling and display irregular endings.

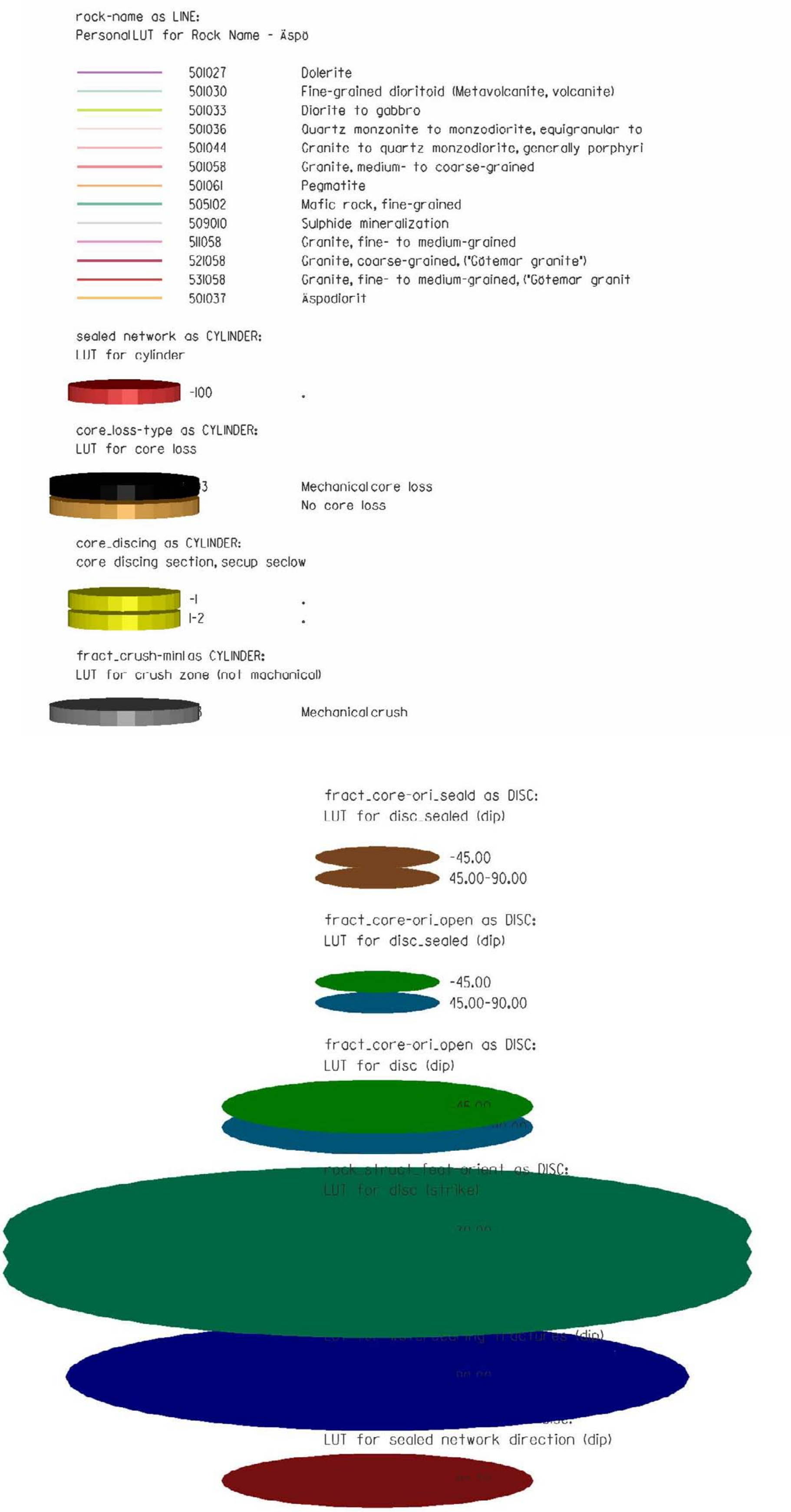

Figure 3-13. Legend for visualized parameters in the boreholes.

3.4.4 Fracture statistics

The fracture characteristics as documented during mapping have been analyzed and are being presented as tables, stereographic plots and describing text in the result section.

Existing tunnel sections in the TMS database used as input when the present RVS work started was; the APSE tunnel (TASQ, also data outside model volume), deposition holes (DQ), Pillar (AQ) and the Pillar wall (VQ).

3.5 Texture and mineralogy

The outcome of a regular Boremap mapping is qualitative in its character and not fully complete in this respect either, even less so for earlier versions of Boremap used for some of the boreholes concerned. In order to get a somewhat more detailed qualitative picture of the geology related to the core-disking fracturing, three thin sections were prepared from three separate core sections (at 2.97-3.01 m in KQ0062G05, 0.25-0.32 m in KQ0062G06 and 5.17-5.20 m in KQ0061G10). They where studied under microscope, with polarized light facilities in order to look for relations between core-disking phenomena and mineralogy and texture.

3.6 Numerical modeling

During planning of the APSE experiments, overcoring stress measurements were conducted in a pilot hole, and convergence measurements and back-calculation of stresses were conducted during tunneling /Sjöberg, 2003; Andersson, 2004/. There were, however, no stress measurements conducted during the actual experiment or during the drilling of the de-stressing slot or the cutting and removal of the pillar. For these stages of the work, numerical modeling was extensively employed as a means to understand the stress evolution during the whole APSE project /Andersson, 2007/. In the previous simulations for the APSE experiment, the *in situ* stress tensors shown in Table 3-2 were used.

Table 3-2. Summary of in situ stresses used in previous simulations for the APSE experiment /Fredriksson et al., 2004; Rinne et al., 2004; Wanne et al., 2004/.

σ_1		σ_2		σ_3	
Magnitude [MPa]	Trend/Plunge [°]	Magnitude [MPa]	Trend/Plunge [°]	Magnitude [MPa]	Trend/Plunge [°]
27	310/07	15	090/83	10	208(00

The modeling performed for the present project was aimed at helping to interpret the core disking and borehole breakout observations at the APSE site, as it was realized that existing numerical models /Andersson, 2007; Mas Ivars, 2006/ could not fully explain the observed core disking at the test site.

Due to the three-dimensional nature of the problem studied, a three-dimensional model was judged appropriate to be able to simulate the complex stress re-distribution during the drilling of the de-stressing slot and the pillar removal. It was also judged important to capture the influence of the major fractures in the APSE volume. For this reason the three dimensional distinct element code *3DEC* /Itasca, 2003/ was chosen for the numerical modeling exercise.

3.7 Results and evaluation

The results of each of the conducted subtasks are presented in Chapter 4 (geology, core disking, geological modeling), Chapter 5 (stress measurements), and Chapter 6 (numerical stress modeling). A summary evaluation of the combined results is given in Chapter 7, along with a discussion of the results. This includes a comparison of stress measurements, numerical modeling results, and disking observations, and a discussion of the lessons learnt from this study.

4 Geology and borehole observations

4.1 Fractures

The orientation and mineralogy mapped in the separate parts of the TASQ tunnel is graphically shown in Figure 4-1. In boreholes the cut-off level of fracture length corresponds to approximately 2 cm, whereas it is about 0.5 m in the deposition holes and pillar wedge, and about 1 m in the tunnel. The data is therefore not completely comparable.

There are a total of 62 broken fractures (defined as fractures that part the core) in the four mapped core-disking boreholes, which gives an average of 3.9 fractures per m. There are also 82 mapped unbroken fractures (defined fractures that do not part the core) and 22 "sealed networks" with a total core length of about 3.4 m. The sealed networks, which can be described as a fine network of unbroken fractures that are too intricate to be mapped separately, thus make up more than 20 % of the total core length.

It should be noted that broken fractures are mapped as such since they part the core, although some most probably have been parted during the drilling and management of the core. Of the 62 broken fractures 20 are mapped as planar, 38 as irregular and four as stepped or undulating. All are mapped as rough fractures. A total of 44 of the fractures have a fresh surface, whereas the rest display slightly or moderately altered surfaces.

The mineralogy in fracture infillings in broken fractures is dominated by calcite and chlorite. Calcite is found in most fractures. Clay minerals are also rather common as joint infillings. Less common is epidote, adularia and oxidized walls, in order of decreasing abundance. The mineralogy of unbroken fractures is similar to that found for broken fractures, with the exception that that epidote and oxidized walls is more frequent in unbroken fractures.

4.2 Core disking — observations, mineralogy, and texture

4.2.1 Mapping

During the Boremap mapping core-disking were registered in boreholes KQ0062G05 and KQ0062G06. Also in KQ0062G01, which is not mapped in Boremap, a section of core-disking is registered. This section has been manually visualized in RVS. A summary of observed core disking is given in Table 4-1. An example of the observed disking is shown in Figure 4-2 and Figure 4-3.

It should be noted that no ring disking (of hollow cores) was observed in any of the boreholes. In the upper part of KQ0062G06 several tendencies to core-disking appear as narrow sections located in close relation to naturally occurring fractures. These have not been mapped as core-disking. At a few locations of mapped core-disking it is uncertain whether it actually is core-disking or not, which is noted in the comments of the mapping database. There are also some registrations of what has been noted as initial core disking. This is where the core disks not actually split the core and may only have developed on one side of the core. It was noted during mapping (and stress measurement) that at several locations (>4) the core-disking phenomena coincides with steeply dipping fractures, particularly broken fractures.

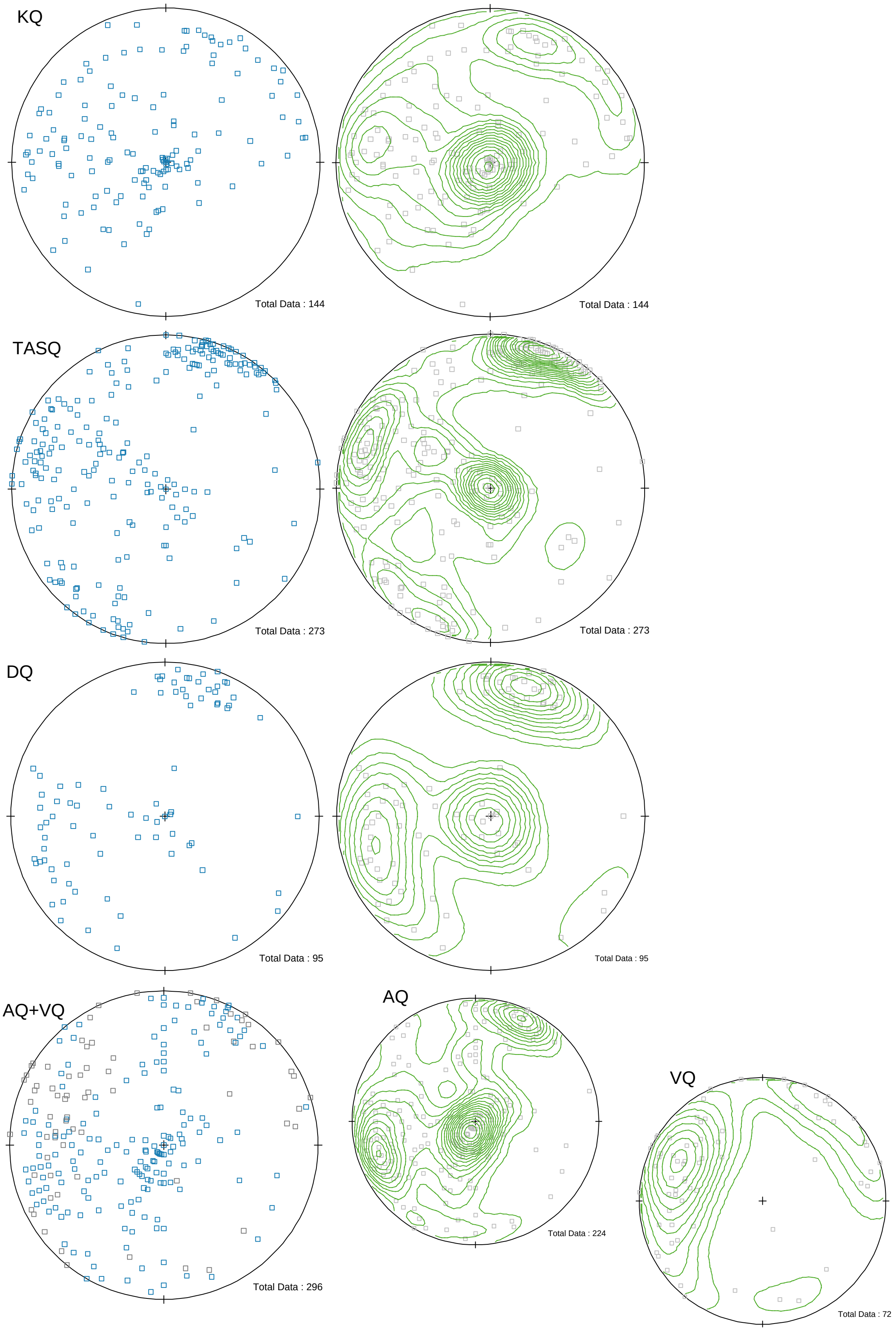

***Figure 4-1.** Stereographic projection (lower hemisphere, equal area) showing poles to fractures in the separate areas in the TASQ tunnel (Core disking boreholes=KQ, Tunnel=TASQ, Deposition holes=DQ, Pillar wall=AQ and Pillar wall=VQ). To the right, Kamb contour plots of the same data.*

Table 4-1. Observed core disking (solid core) at the test site in the TASQ tunnel, Äspö HRL.

Borehole	Location (vertical depth) (m)	Disk thickness (mm)	Comments
KQ0062G01	2.26–2.71	10	Disking primarily on one side of the core (core split by steeply dipping fracture).
KQ0062G05 (A1)	2.50–2.70	7–15	-
KQ0062G06 (C4)	0.56–0.64	15–30	Slightly concave, disking close to fracture plane.
KQ0062G06 (C4)	2.51–2.67	5–20	Disking starts at location of steeply dipping fracture. Crushed rock at end of section.
KQ0062G06 (C4)	4.24–4.27	12–25	Disking not fully developed for all disks.
KQ0062G06 (C4)	4.86–5.02	15	Disking near fracture plane.
KQ0062G06 (C4)	6.01–6.04	-	-

Figure 4-2. *Observed core disking in borehole KQ0062G06 at 0.56–0.64 m depth.*

Figure 4-3. *Observed core disking in borehole KQ0062G06 at 2.51–2.67 m depth.*

4.2.2 Observations in thin sections

Sample A1 Sample from Borehole KQ0062G05, at 2.97-3.01 length.

The rock is a Quartz-monzodiorite to granodiorite, with feldspar phenocrysts, i.e. a typical "Äspö diorite". The mineralogy is composed of larger feldspar-grains (a few millimeter wide, both plagioclase and potassium feldspar), in a partly mylonitic matrix of grain-size reduced quartz and feldspar, as well as some epidote and chlorite. Minor amounts of euhedral sphene and opaque phases are also present. Plagioclase has normally suffered from rather strong sericitic and partly also from chloritic alteration.

Obvious core-disking factures are running at right angle to the core axis. There are three persistent fractures in the thin section. One of these represents a single plane, whereas the two others have a slight “en echelon” character. All three fractures lie in an angle of ~80° to the metamorphic fabric in the rock, apparently unaffected by texture and mineralogy. Their orientation seemed, only occassionally, to be guided along grain boundaries or internal crystallographic orientations. No mineral infilling or signs of pre-existing fracture planes was detected. The width of the fractures is narrow and even.

Sample C4 Sample from Borehole KQ0062G06, at 0.25-0.32 length.

The rock is a Quartz-monzodiorite to granodiorite, with feldspar phenocrysts, i.e. a typical "Äspö diorite". Similar mineralogy, deformation and texture as in sample A1.

Two fractures caused by initial core-disking (failed rock but not parted core) were mapped in the core, apparently with a slight saddle shape. The fractures are at approximately 80° to the fabric in the rock. In thin section, however, these fractures are only barely visible. They display a slight ‘en echelon’ fabric and appear to run essentially unaffected by grain boundaries. However, locally there seem to be mineral infilling that has crystallized along the fracture. Because of its narrow width it is difficult to decide the exact mineralogy in the fracture, but calcite is a major constituent and probably also quartz.

Sample B2 Sample from Borehole KQ0061G10, at 5.17-5.20 length, close to a conducted stress measurement.

The rock is a Quartz-monzodiorite to granodiorite, with feldspar phenocrysts, i.e. a typical "Äspö diorite", with similar texture as sample A1 and C4. Somewhat lower content of potassium feldspar then in the two other samples. In this sample, however, the matrix is dominated by biotite with mm-large grains of sphene. It also contain a few, very fine-grained bands with biotite and epidote.

In the core there is a fracture running approximately 10-20º to the fabric in the rock. It has an irregular course. The fracture is hard to detect in thin section. However, slightly offset and sub-parallel to the macroscopically visible fracture another fracture is found in the thin section. It is irregular with variable width and ends in a lithological band rich in biotite. The fracture runs across most grain boundaries. A minor part of the fracture contains calcite, but elsewhere it has no infillings.

4.2.3 Conclusions regarding core-disking

From three thin sections alone it is not possible to make any decisive conclusion regarding core disking phenomena appearing in the area in general. However, the following may be concluded:

1. The rock in the area has suffered from severe ductile and brittle deformation in the geological past and because of this there are a lot of ductile structures that potentially could guide newly formed fractures. Likewise there are a high frequency of sealed (and open) fractures with lower shear and tensile strength than the intact rock.

2. The observations in the thin sections seem to indicate that fractures related to core-disking are not guided by grain boundaries or crystallographic planes when passing through hard minerals such as quartz and feldspar, but are possibly guided when passing through softer minerals such as phyllosilicates, at least when the rock is fine grained.

3. Occasionally core-disking fractures run along pre-existing fractures and other structures, but generally not.

4.3 Borehole breakouts

The BIPS logging conducted in the boreholes enabled a crude assessment of possible damages to the borehole walls, so-called borehole breakouts. Breakouts could be found sporadically in the boreholes, as shown in Table 4-2. As locations are uncertain, only approximate orientations have been given.

Table 4-2. Observed borehole breakouts the test site in the TASQ tunnel, Äspö HRL.

Borehole	Location (vertical depth) (m)	Orientation	Comments
KQ0062G05 (A1)	2.25–2.45	SW	Near fractures
KQ0062G05 (A1)	2.75–3.15	NE	Uncertain, may be longer
KQ0062G04 (B1)	0.80–1.00	ENE	Very uncertain, near fracture
KQ0062G04 (B1)	1.00–1.25	NE	Very uncertain
KQ0061G10 (B2)	2.70–3.00	NE	-
KQ0062G06 (C4)	2.80–2.95	SSW & NNE	-
KQ0062G06 (C4)	5.15–5.25	S & ENE	Very uncertain

4.4 RVS modelling

The components and geometry of the model is best understood when viewed in 3D on a computer screen. In Appendix B a set of 2D figures give a brief view of the model and also tables listing the visualized and modeled objects.

There are basically three different kinds of objects that have been modeled; ductile shear zones, open (water-bearing) fractures and sealed complex fractures. Whether a fracture is water-bearing or not has been used as a criterion for inclusion in the model, a decision taken in an early project meeting. In addition there are also two non water-bearing fractures that are included with the model, structures inherited from earlier models. These latter may or may not be used in the *3DEC* model.

The major structure passing through the model volume is a ductile shear zone. This has earlier been modeled as faulted along a fracture to the southwest of the core-disking boreholes. Both the part of the shear zone to the southwest of the fault and the fault itself has been left unchanged from previous models in the present model. The continuation of the shear zone has been remodeled as two separate splays as indicated in the mapping of deposition hole DQ0066, one with approximately the same orientation as in the outer part of the tunnel and one steeper splay. Both splays are simplified being modeled as planar surfaces at the approximate centre of the zone.

In the lower part of the model volume two gently dipping fractures have been interpolated, between deposition holes and boreholes. These structures are mapped as single fractures, but are actually narrow complex network or breccias sealed by primarily epidote. They are not water-bearing.

The other modeled structures are all steeply dipping water-bearing fractures. Although these are modeled as single planar objects, they normally show a slight irregularity or undulation and also often show an ‘en echelon’ character at several locations in the tunnel, deposition holes and pillar.

Most structures have been modeled as running through the full model volume. A few terminate towards other modeled structures and one ends in the rock matrix beneath the tunnel floor. The considerations made when decisions in these matters where done is based on an iterative process of extrapolation of structures out from a known location, using model surfaces of slightly different orientation and location.

The shear zone that runs along the tunnel has a local orientation of 038/55 (Äspö96, 023/55 magnetic north) when passing through the tested rock volume. In the mapping it is detected in the upper part of KQ0062G04 and KQ0062G05.

One water-bearing fracture has been modeled across all boreholes in the test volume. It has been interpolated with fractures mapped in the tunnel and deposition hole DQ0063G01. In the boreholes it is particularly obvious in KQ0062G05 and KQ0062G06, but also in KQ0061G01 although this hole has not been mapped in Boremap. In the latter borehole the fracture, running steep across the hole, coincides with the upper boundary to a section of core-disking and in KG0062G06 the fracture also runs through a section of core-disking. In KQ0062G05 the fracture is close to a section of core-disking. The fracture is located below KQ0062G04 and in KQ0061G10 the location of the fracture is more difficult to pinpoint, if present at all.

4.5 Mechanical properties

A summary of the mechanical properties of the rocks at the test site is given in Table 4-3 /Andersson, 2007/. An important outcome of that work was also the determination of spalling strength in the deposition hole scale. Back calculations of spalling observations showed that spalling initiated when the tangential stress (at the boundary of the deposition hole) reached 122 MPa, or 58% of the uniaxial compressive strength. No additional tests have been conducted as part of the present work.

Table 4-3. Summary of mechanical properties for the rock at the APSE site /Andersson, 2004, 2007/.

Parameter	Mean value	Range
Uniaxial compressive strength [MPa]	211	187–244
Young's modulus, intact rock [GPa]	76	69–79
Young's modulus, rock mass [GPa]	55	-
Poisson's ratio, intact rock	0.25	0.21–0.28
Friciton angle, intact rock [°]	49	-
Cohesion, intact rock [MPa]	31	-
Tensile strength [MPa]	14.9	12.9–15.9
Density [kg/m^3]	2750	2740–2760
Crack initiation stress, AE [MPa]	121	80–160
Crack initiation stress, strain gauge [MPa]	95	83–112

5 Overcoring stress measurements

5.1 Overview

Overcoring stress measurements were conducted during the period of January 16 to February 9, 20006. Measurements were attempted in three boreholes, see Figure 3-10. A brief summary of the measurement attempts is given in Table 5-1. All tests have been numbered as follows: *hole number: test no. : pilot hole no.* Thus, e.g., test KQ0061G10:1:2 denotes hole number KQ0061G10, test (or measurement) no. 1 at that level, and pilot hole no. 2 (to reach an acceptable measurement location for this test). Each test is presented with a rating reflecting successfulness and reliability of that particular measurement. Ratings were assigned per the following criteria:

Rating	Description and criteria
a	**Successful test**
	• Geometrical conditions achieved (strain gauges at correct position, etc).
	• Stable strain response prior to, and during, overcoring with minimal strain drift (strain change less than 10 μstrain per 15 min for undisturbed conditions).
	• No fractures and/or core disking observed in the overcore sample (at least 24 cm intact core).
	• Linear and isotropic (20-30% deviation acceptable) strain response during biaxial testing. Minor hysteresis (< 100 μstrain) accepted.
	• Stress calculation possible with classical analysis (Section 4.4.1). Values on elastic constants may be assumed from nearby tests if biaxial test data are lacking, and all other criteria above are satisfied.
b	**Partly successful test**
	• Signs of debonding but fairly stable strain response up until peak value (typically at 24-30 cm drill bit position).
	• Stress calculation possible with classical analysis (Section 4.4.1) but results judged uncertain and/or less reliable.
	• Additional stress determination may be conducted using inverse solution of transient strain analysis (Section 4.4.2).
c	**Failed test**
	• Installation failed or incomplete.
	• Debonding of strain gauges and/or large strain drift.
	• Fractures/joints detected in overcore sample.

It should be noted that measurement conditions were difficult at the test site. Practical problems of securing the drill rig to obtain sufficient feed force prevailed, making overcoring drilling less reliable. Also, geological conditions were adverse, with several sub-vertical, sometimes open, fractures intersecting the boreholes. This inhibited measurements at several locations and may also have affected the results of the measurements that were possible to take.

Table 5-1. General test data from measurements in the TASQ tunnel, Äspö HRL.

Test no. (pilot hole no. *)	Vertical depth (m) **)	Overcoring	Biaxial testing	Rating	Comments
KQ0061G05:1:3 (A1)	224.22	No	No	-	Installation failed, compass did not lock.
KQ0062G06:1:5 (C4)	6.20	No	No	-	Many pilot holes required to reach a good measurement location. However, overcoring not possible due to obstruction in the borehole.
KQ0062G06:2:1 (C4)	6.98	Yes	No	-	Logger malfunction, data not saved. Subsequent biaxial test failed.
KQ0061G10:1:2 (B2)	4.13	Yes	Yes	*c*	Successful installation but unrealistic strain response for strain rosette nos. 1 and 3. Fair response for rosette no. 2. Large temperature increase during overcoring. Biaxial test OK for rosette no. 2.
KQ0061G10:2:1 (B2)	5.18	Yes	Yes	*b*	Successful installation and fair strain response. Large temperature increase during overcoring. Good biaxial test, excluding rosette no. 3.

*) numbering *scheme: (hole number : test no. : pilot hole no.) Alternative hole names in parenthesis (cf. Figure 3-10)*

**) vertical depth (below tunnel floor) in each hole

5.2 Overcoring test data

A total of five attempts were made, with successful installation and strain data retrieved from two of these. Results from these tests (regardless of rating) are presented in the following and in Appendices C through G. Key measurement data (recorded times for borehole activities) are presented in Appendix C. Furthermore, photos of core samples are presented in Appendix G.

The strain response for each test is shown in Appendix D. Each test is presented with two plots displaying (i) the complete strain record (from activation of probe to core recovery), and (ii) the strain response from overcoring start to overcoring stop. The latter was used to define strain differences for later input to stress calculation. In the Figures, the given times reflect the events recorded during overcoring. The times for which the strain differences have been determined ("OC Start" and "OC Stop") are shown in Appendix C.

The first test (KQ0061G10:1:2) gave unrealistic strain response during overcoring, in particular for strain rosette nos. 1 and 3. This may be a sign of debonding. The temperature increase during overcoring was large (15°C increase), which may be due to insufficient flushing capacity. The second test gave a better strain response, but temperature increase was still large (around 10°C increase)

5.3 Biaxial test data

All suitable overcore rock samples were tested in the biaxial cell to determine the elastic properties. Thus, biaxial tests were conducted for test nos. KQ0061G10:1:2 and KQ0061G10:2:1. Test no. KQ0061G10:1:2 gave highly unrealistic strain response for rosette nos. 1 and 3. However, rosette no. 2 showed fairly linear and stable strain behavior and could be used to determine the elastic constants. Test no. KQ0061G10:2:1 yielded results with good linearity and isotropic behavior, when excluding rosette no. 3. This test also showed fairly small hysteresis. The resulting elastic constants are presented in Table 5-2. The biaxial test results are presented in Appendix E.

Table 5-2. Results from biaxial testing on overcore samples from measurements in the TASQ tunnel, Äspö HRL.

Measurement no. (pilot hole no. *)	Vertical depth (m) **	Young's modulus, *E* (GPa)	Poisson's ratio, *ν*
KQ0061G10:1:2 (B2)	4.13	64.4	0.26
KQ0061G10:2:1 (B2)	5.18	51.7	0.27

*) numbering *scheme: (hole number : test no. : pilot hole no.) Alternative hole names in parenthesis (cf. Figure 3-10)*

**) vertical depth (below tunnel floor) in each hole

5.4 *In situ* stress state

The *in situ* stress state was calculated using (i) the measured strain response (difference between strain gauge readings after and prior to overcoring), (ii) recorded orientation of strain gauge rosettes in the borehole, and (iii) values on elastic constants determined from biaxial testing. Strain differences were determined from stable strain values before overcoring vs. stable values after completed overcoring. In this particular case, strain values had to be taken at the end of the flushing period (before core break), as strain fluctuated highly in earlier stages. This would also act to minimize the possible influence of temperature on the strain readings (cf. Appendix C in which the times for which strain differences were calculated are given). No mean stress calculation was performed. The resulting stresses for each test are shown in Appendix F, and in Table 5-3, Table 5-4, and Table 5-5. All orientations are given relative to geographic north.

The resulting stresses for the first measurement, at 4.13 m depth, are clearly unrealistic (as manifested e.g., by the extremely high vertical stress component). This was to be expected, given that the strain response was very unstable and that the measurement was given a *c* rating. The second measurement, at 5.18 m depth, is judged to be more realistic. Stresses are fairly low, with a maximum horizontal stress of only 14 MPa, which is significantly lower than expected from the numerical modeling carried out prior to the measurements, and also lower than the *in situ* stresses used in previous modeling for the APSE project, cf. Sections 3.2 and 3.6. Further discussions on this are provided in Section 7.3.

Table 5-3. Magnitudes of principal stress as determined by overcoring in the TASQ tunnel, Äspö HRL.

Measurement no. (pilot hole no. *)	Vertical depth (m) **	σ_1 (MPa)	σ_2 (MPa)	σ_3 (MPa)
KQ0061G10:1:2 (B2)	4.13	82.3	47.4	14.6
KQ0061G10:2:1 (B2)	5.18	18.1	5.3	1.5

*) numbering *scheme: (hole number : test no. : pilot hole no.) Alternative hole names in parenthesis (cf. Figure 3-10)*

**) vertical depth (below tunnel floor) in each hole

Table 5-4. Orientations of principal stress as determined by overcoring in the TASQ tunnel, Äspö HRL.

Measurement no. (pilot hole no. *)	Vertical depth (m) **	σ_1 Trend/Plunge (°)	σ_2 Trend/Plunge (°)	σ_3 Trend/Plunge (°)
KQ0061G10:1:2 (B2)	4.13	285/73	149/12	056/11
KQ0061G10:2:1 (B2)	5.18	300/33	153/52	040/16

*) numbering *scheme: (hole number : test no. : pilot hole no.) Alternative hole names in parenthesis (cf. Figure 3-10)*

**) vertical depth (below tunnel floor) in each hole

Table 5-5. Horizontal and vertical stress components calculated from measured principal stresses in the TASQ tunnel, Äspö HRL.

Measurement no. (pilot hole no. *)	Vertical depth (m) **	σ_H (MPa)	σ_h (MPa)	σ_v (MPa)	Trend σ_H (°)
KQ0061G10:1:2 (B2)	4.13	49.0	17.0	78.3	144
KQ0061G10:2:1 (B2)	5.18	14.3	1.8	8.8	123

*) numbering *scheme: (hole number : test no. : pilot hole no.) Alternative hole names in parenthesis (cf. Figure 3-10)*

**) vertical depth (below tunnel floor) in each hole

6 Numerical modeling

6.1 Introduction

Numerical modeling has been extensively employed as a means to understand the stress evolution during the whole APSE project /Andersson, 2007/. The reason for this is that there were no stress measurements during the actual APSE experiment (drilling of canister holes, heating, drilling of de-stressing slot, and cutting and removal of the pillar).

A complete numerical study of the stress evolution during the APSE experiment can be found in /Andersson, 2004; Fredriksson et al. 2004; Rinne et al. 2004 and Wanne et al. 2004/. An additional evaluation of the thermal induced stresses is reported in /Fälth et al. 2005/.

In the present project, numerical modeling has been performed to help interpret the core disking and borehole breakouts observations at the APSE site.

It was decided not to model the thermal loading explicitly and rather remove the areas of the model where spalling occurred during this stage of the APSE experiment. Any further damage to the rock during the thermal stage was considered to be transient.

The model includes the stages of tunnel excavation, deposition hole excavation, removal of the spalled parts of the wall of deposition hole DQ0063G01, excavation of the two additional slots, drilling of the de-stressing slot and removal of the pillar.

Due to the specific geometry of the APSE experiment, which is non-symmetrical, and the three-dimensional nature of the problem studied, a three-dimensional model was judged appropriate to be able to simulate the complex stress re-distribution during all the stages of the APSE project. It was also judged important to capture the influence of the major fractures in the APSE volume (cf. Figure 3-2). The fractures shown in this figure were included explicitly in the *3DEC* modeling study presented in this report. The X and Z axis in Figure 3-2 refer to the model coordinate system.

For this reason, the three-dimensional distinct element code *3DEC*, /Itasca, 2003/ was used to perform the numerical simulations. This code is suited to simulate the behavior of rock masses containing multiple, intersecting discontinuities.

6.2 Conceptual model

Based on the latest version of the RVS model of the TASQ tunnel and the available data on the *in situ* stress field and rock mass mechanical properties, the conceptual model of the study volume was created.

6.2.1 Geometry

The geometrical model consisted of the TASQ tunnel, the two individual deposition size holes at the APSE site, the two additional slots excavated before the drilling of the de-stressing slot, the de-stressing slot, and the part of the pillar that was removed. All these elements were embedded in a parallelepiped of rock of 34m x 50m in horizontal section and 40m in height, considered large enough to avoid any mechanical boundary effects. A schematic view of the model containing the tunnel and the deposition holes can be seen in Figure 6-1.

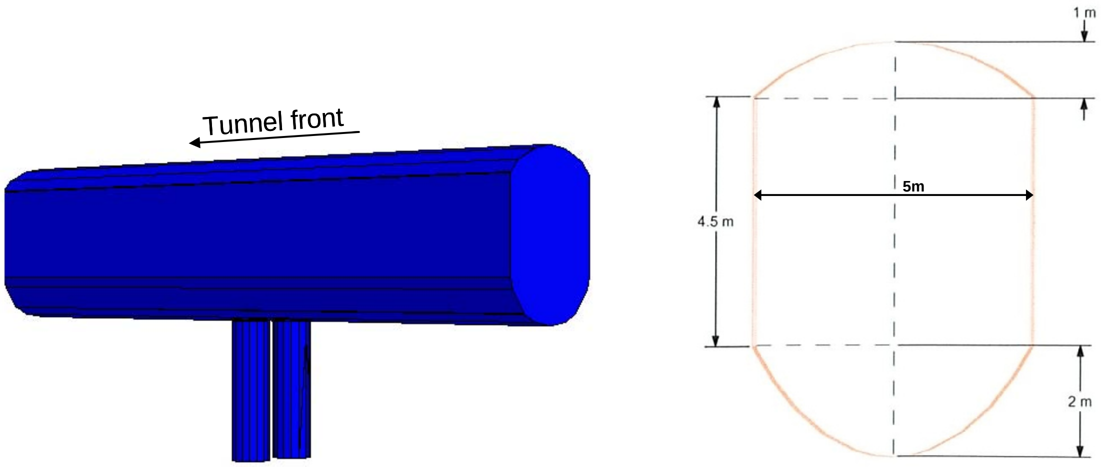

a)

b)

Figure 6-1. *Schematic view showing a) three-dimensional model of the TASQ tunnel and the APSE deposition holes, and b) vertical section of the TASQ tunnel /Staub et al, 2004/.*

Two additional slots, each 0.5 m deep, were cut prior to the drilling of the de-stressing slot to study the EDZ at the TASQ tunnel.

The mesh, shown in Figure 6-2, consisted of four-node tetrahedral elements, which had an average side length of 0.1m in the center of the model, in an area that comprised the deposition holes, the pillar and the de-stressing slot. The mesh becomes gradually coarser with the increase of the distance to the center of the model. The model was discretized in a total number of 1959530 tetrahedral elements and 525809 vertices.

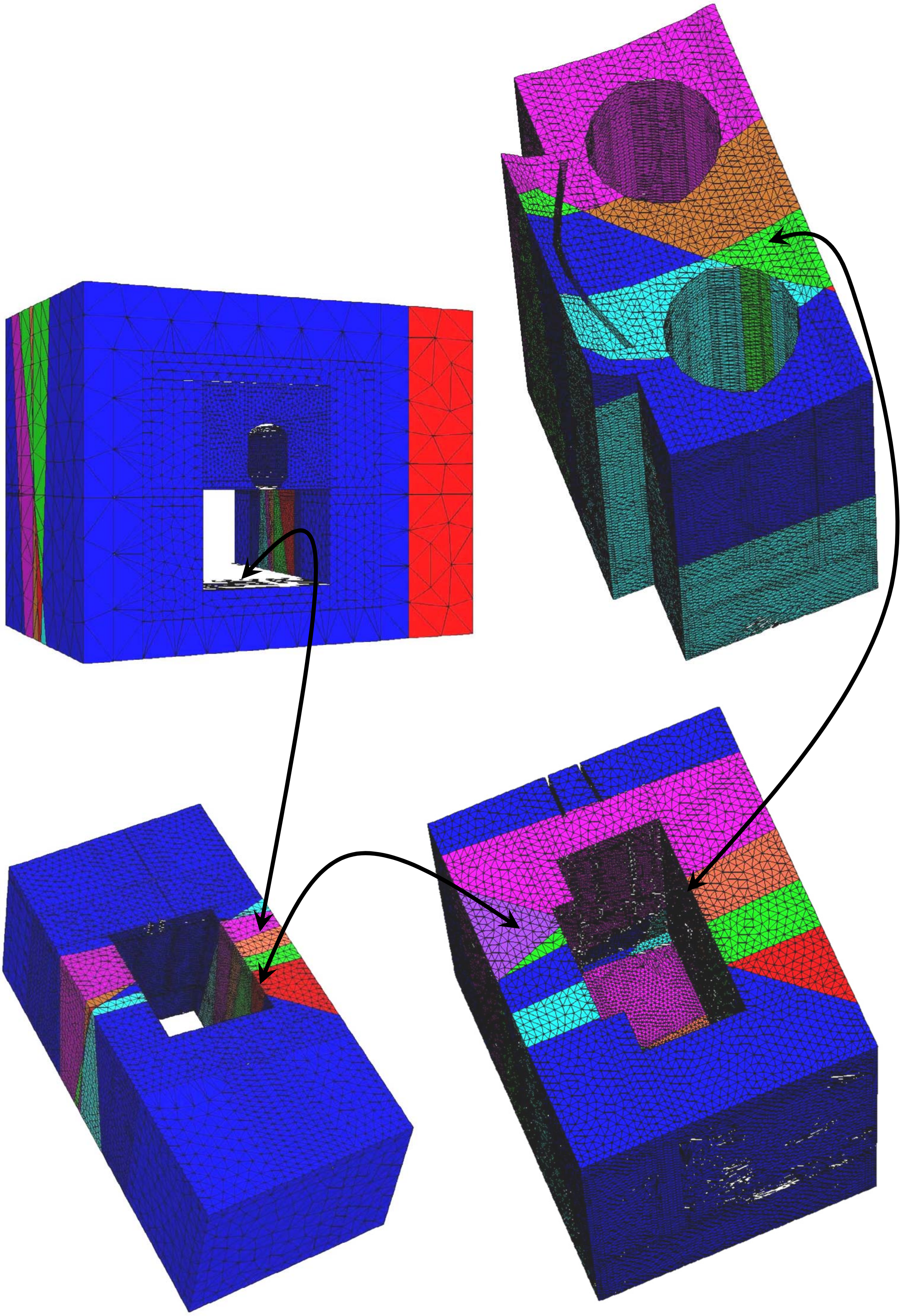

Figure 6-2. *The model mesh.*

The fractures included in the *3DEC* model based on the RVS model are listed in Table 6-1. Their location relative to the APSE area is shown in Figure 3-1.

Table 6-1. Fractures included in the model.

	Dip (degrees)	Dip direction (degrees)	Comments
Fracture 08	84.4	83	
Fracture 14	85	250	
Fracture 80	90	87	Active after part 2 of de-stressing slot is excavated.
Core discing	72.8	89.6	
NW structure 2	81	93	

The model has a continuum rock mass buffer of 4m thickness in each of the boundaries. This is included to represent the far field rock mass. This means the plane that represents each of these fractures in the model can prolong only until it reaches this rock buffer in any direction. Figure 6-3 shows the model of the tunnel and the deposition holes including the fractures listed in Table 6-1.

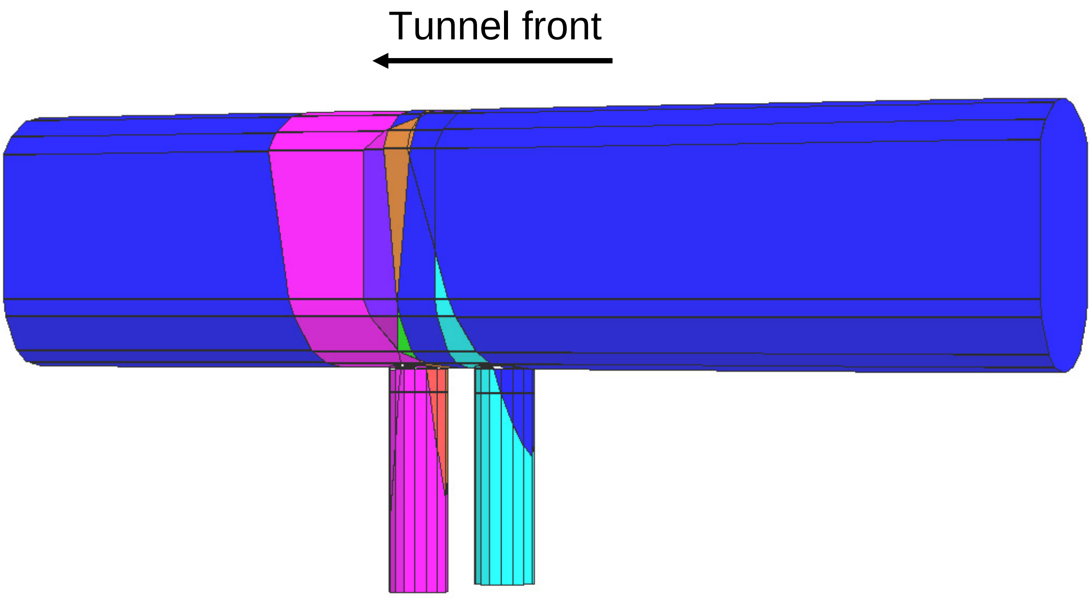

***Figure 6-3.** Three-dimensional model of the TASQ tunnel and the APSE deposition holes including the fractures listed in Table 6-1.*

6.2.2 *In situ* and boundary conditions

The *in situ* and boundary conditions considered in the model are as follows:

- Hydrostatic water pore pressure (4.5MPa at the depth level considered) was applied in the fractures. The water pore pressure in the Äspö HRL at the 450m depth ranges from 2MPa to 4.5MPa according to the HMS measurements. Therefore the chosen value of the water pore pressure in the fractures in the model might be slightly overestimated. This implies that the effective normal stress acting on the fractures in the model might be lower in some locations that the one in-situ. In general, lower normal effective stress acting on the fractures causes larger shear fracture displacements. However, due to the high stresses induced during the different stages of the simulation, the possible water pore pressure overestimation will only amount to a small percentage of the normal stress acting on the fractures, so its influence will be minimal. The normal fracture displacement will not be affected in this case because it only depends on the relative change in normal stress and not in its absolute value..

- Based on the *in situ* stress tensors used in the previously reported simulations (see Table 3-2) and in the stress tensor obtained from the back-calculation of the convergence measurements made during the excavation of the TASQ tunnel /Andersson, 2004/, two different *in situ* stress tensors were applied in the present models (Table 6-2). The approximate orientation of the major and minor principal stress relative to the APSE tunnel axis is shown in Figure 3-2

Table 6-2. In situ principal stress tensors used in the models.

	Sigma 1		Sigma 2		Sigma 3	
	Magnitude (MPa)	**Trend/Plunge (°)**	**Magnitude (MPa)**	**Trend/Plunge (°)**	**Magnitude (MPa)**	**Trend/Plunge (°)**
In situ stress tensor 1*	30	310/00	15	090/90	10	220/00
In situ stress tensor 2**	27	310/00	12	090/90	10	220/00

TASQ tunnel orientation is 046˚

* Derived by back-calculation of the convergence measurements using a Young's modulus of 55Gpa.

** From previous models of the APSE experiment /Christiansson & Jansson, 2003/.

- In the lateral and lower boundaries no displacement in the normal direction to their respective surfaces was allowed. They may move freely in the other directions.

- In the upper boundary the vertical principal stress (σ_2) was applied as boundary condition.

6.2.3 Rock material properties

A linear elastic constitutive model was adopted for the rock. Two different rock material cases were modeled in combination with the two different *in situ* stress tensors in Table 6-2. The material parameters used in each of these cases are shown in Table 6-3 (see also Section 4.5).

Table 6-3. Material parameters of the rock (/Andersson, 2004/).

	E (GPa)	*v*	*P* (kg/m^3)
Rock mass	55	0.26	2731
Intact rock	76	0.25	2731

As this project is mainly concerned about the stresses in an area very close to the walls of the deposition holes forming the APSE pillar experiment, it is considered that, in this particular problem, the intact rock material is more representative of the rock in this small area (see boreholes area in Figure 3-1). However, both intact rock and rock mass cases have been modeled in order to see the sensitivity of the results to the rock material parameters.

The fractures followed a Coulomb slip model in which zero tensile strength was assumed. The fracture parameters are shown in Table 6-4. The values are chosen from available published data / Staub et al. 2003 and 2004; Jacobsson and Flansbjer, 2005; SKB, 2006; Olofsson et al. 2007/ and properly adjusted, taking into account that laboratory properties are often not representative of *in situ* properties due to scale effect /Fardin, 2003/, difference in boundary conditions (laboratory tests having often stress boundary conditions while there are stiffness boundary conditions *in situ*), the fact that laboratory tests derived properties are usually taken at large displacements while the displacements *in situ* are relatively small (friction angles are typically much larger for small displacements), fractures *in situ* are not perfectly planar, they are undulated to a higher or lower degree, etc.

Table 6-4. Fracture parameters.

	Kn (GPa/m)	Ks (GPa/m)	Cohesion (MPa)	Friction angle (degrees)	Dilation angle (degrees)
Fracture 08	200	100	0.9	36	3
Fracture 14	200	100	0.9	36	3
Fracture 80*	200	100	0.9	50	3
Core discing fracture	200	100	0.9	40	3
NW structure 2	200	100	0.9	40	3

*Fractured induced when the second part of the de-stressing slot was excavated completely.

6.2.4 Simulation sequence

The simulation sequence followed in this numerical study is as follows:

1. Calculation to initial equilibrium of the parallelepiped of rock mass (all fractures in the model considered non-active).
2. Excavation of the TASQ tunnel. Calculation to equilibrium (all fractures active except for fracture 80 in Figure 3-1).
3. Excavation of the deposition holes. Calculation to equilibrium (all fractures active except for fracture 80 in Figure 3-1).
4. Removal of the portion of the deposition hole DQ0063G01 that fell from the pillar wall due to spalling and calculation to equilibrium (all fractures active except for fracture 80 in Figure 3-1).
5. Excavation of both additional slots (Figure 3-1). Calculation to equilibrium (all fractures active except for fracture 80 in Figure 3-1).
6. Excavation of the de-stressing slot. The actual de-stressing slot was composed of 27 boreholes of 64 mm diameter and 26 boreholes of 76 mm diameter (Figure 6.4). Detailed information about the de-stressing slot borehole drilling sequence can be found in /Mas Ivars, 2005/. In the *3DEC* model the boreholes in the de-stressing slot were grouped according to the drilling sequence into five slots: The excavation of these slots in the model followed the borehole drilling sequence (Figure 6-5). The following stages were included in the model:
    a. Excavation of the central part of the de-stressing slot (1). Calculation to equilibrium (all fractures active except for fracture 80 in Figure 3-1).
    b. Excavation of the lateral right middle part (2). Calculation to equilibrium (all fractures active, including fracture 80 in Figure 3-1).
    c. Excavation of the lateral left middle part (3). Calculation to equilibrium (all fractures active).
    d. Excavation of the extreme right part (4). Calculation to equilibrium (all fractures active).
    e. Excavation of the extreme left part (5). Calculation to equilibrium (all fractures active).
7. Removal of the pillar. Calculation to equilibrium (All fractures active).

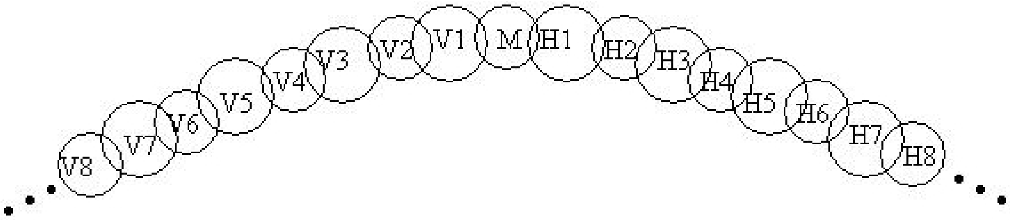

Figure 6-4. *Schematic plot showing the de-stressing slot borehole-drilling sequence. V stands for Vänster (Left in Swedish) and H for Höger (Right in Swedish). M is the first central borehole.*

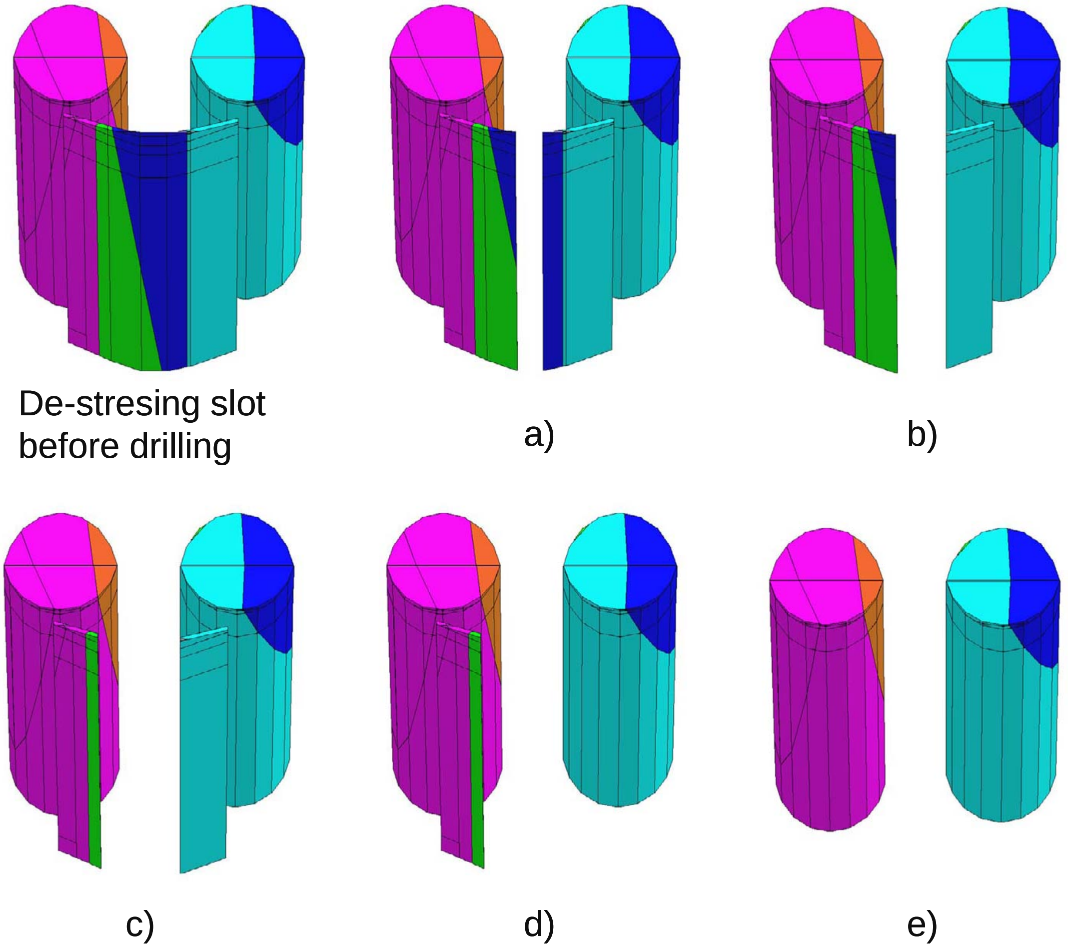
De-stresing slot before drilling

a)

b)

c)

d)

e)

Figure 6-5. *Modeling steps for the excavation of the de-stressing slot in the model, a) central part (1), b) middle right part (2), c) middle left part (3), d) extreme right part (4) and e) extreme left part (5).*

6.3 Modeling results

This section contains the main results of the modeling study described in the previous sections. Further results can be found in Appendix H. It must be taken into account that the results reported are dependent on the assumptions made and the simplified fracture geometry and geology of the conceptual model.

As previously mentioned, four different simulations were performed varying the elastic properties of the rock material and the *in situ* stress field. The four cases are presented in Table 6-5.

Table 6-5. In situ stress and elastic material properties of the different simulations run.

	***In situ* Stress ***	**Elastic properties**
Run3	Sigma1=27Mpa Sigma2=12Mpa Sigma3=10Mpa	E= 76Gpa *v*=0.25
Run4	Sigma1=30Mpa Sigma2=15Mpa Sigma3=10Mpa	E= 76Gpa *v*=0.25
Run5	Sigma1=27Mpa Sigma2=12Mpa Sigma3=10Mpa	E= 55Gpa *v*=0.26
Run6	Sigma1=30Mpa Sigma2=15Mpa Sigma3=10Mpa	E= 55Gpa *v*=0.26

* The orientation of the principal stress was the same in every case. It followed Table 6-2.

6.3.1 Simulated stress response

As *3DEC* is a three-dimensional discontinuum code, it allows stresses to change in a discontinuous manner, creating non-smooth contours. A proper way to show stresses in a discontinuous rock mass is by using principal stress vector plots colored by magnitude. It must be noted, however, that in vector plots (principal stress, traction, velocity, displacement, etc) the length of a vector is affected by the perspective and orientation of observation. This implies that, in cross-section plots, the displayed vectors are projections onto the view plane and, consequently, their length is not indicative of their absolute magnitude. For this reason, the vectors are colored by magnitude. It should be noticed that the maximum compressive stress magnitude shown under the legend menu is only a very local value and it can be caused by stress concentration in a very small corner of the model due to the complex geometry. For this reason, quantitative evaluation of the results should be based on the ranges on the legend. It should be pointed out that, in *3DEC*, a negative value of stress means compressive stress, and a positive value means tensile stress.

The first set of figures shows the principal stress, colored by magnitude of σ$_1$ (Figure 6-6 to Figure 6-9) projected on a vertical cross-section through the center of the deposition holes, at the moment when the pillar has been excavated. Results are shown for all the cases in Table 6-5.

The second set of figures shows the principal stress, colored by magnitude of σ$_1$ (Figure 6-10 to Figure 6-13) projected on a horizontal cross-section at 1.5m depth from the floor of the TASQ tunnel when the pillar has been excavated. Similar to the previous figures, results are shown for all the cases in Table 6-5.

The third set of figures (Figure 6-14 to Figure 6-17) shows the principal stress magnitudes along lines corresponding to the location of boreholes A1, B1, B2 and C4 (see Figure 3-10) in the model.

The final set of figures (Figure 6-18 to Figure 6-21) in this section shows the tangential stress along lines corresponding to the location of boreholes A1, B1, B2 and C4 (see Figure 3-10) in the model as well as the average yield strength at the APSE site from /Andersson 2007/.

The results show that the influence of the two different *in situ* stresses applied is more significant than the difference in elastic properties. Besides, it is important to notice the influence of the steeply dipping fracture intersecting the locations of the study boreholes (core disking fracture in Figure 3-1) in the principal stresses (Figure 6-14 to Figure 6-17) and in the tangential stresses (Figure 6-18 to Figure 6-21). This influence diminishes with increasing distance from the deposition hole.

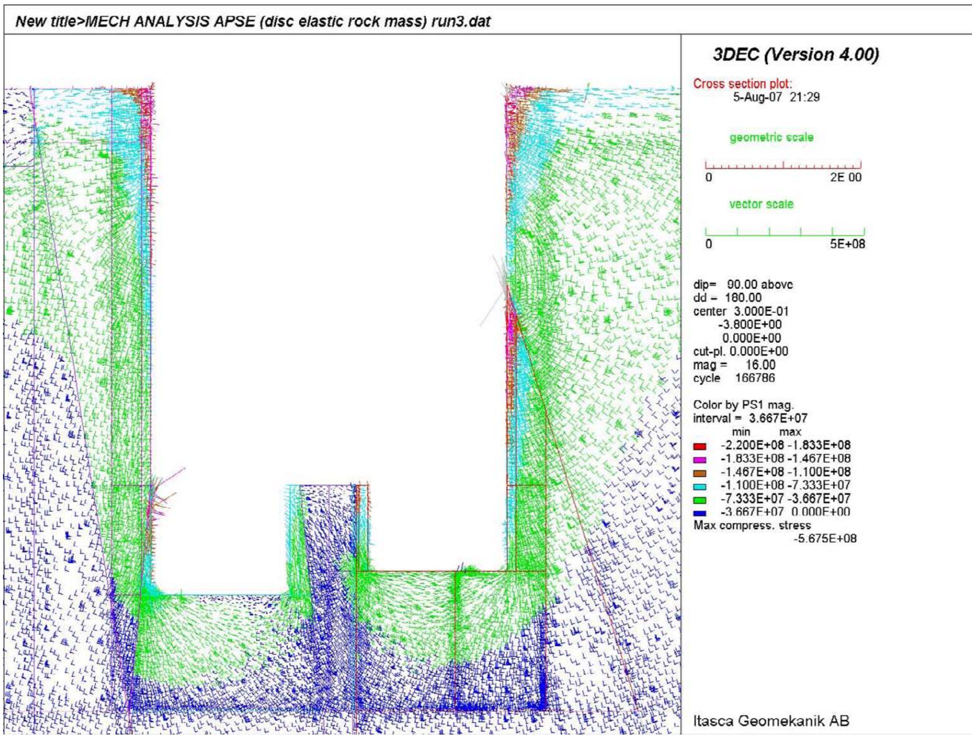

Figure 6-6. *Vertical cross-section showing the projected principal stress along the axis of the tunnel after the central pillar has been removed for case Run3 (Colors by magnitude of σ$_1$).*

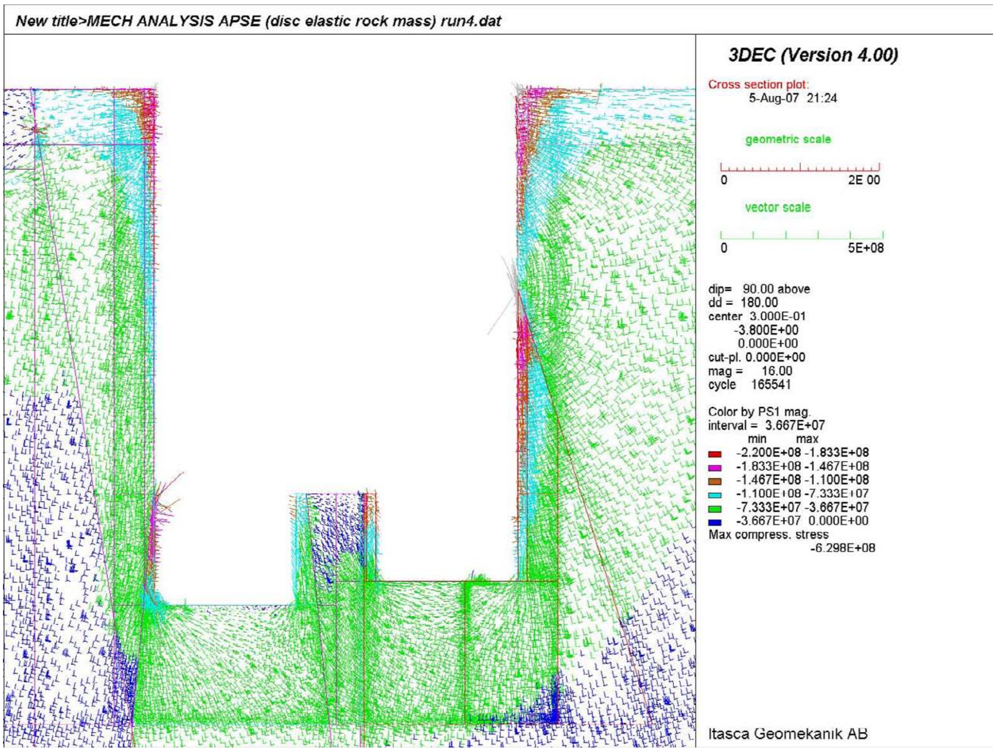

Figure 6-7. *Vertical cross-section showing the projected principal stress along the axis of the tunnel after the central pillar has been removed for case Run4 (Colors by magnitude of* σ_1*).*

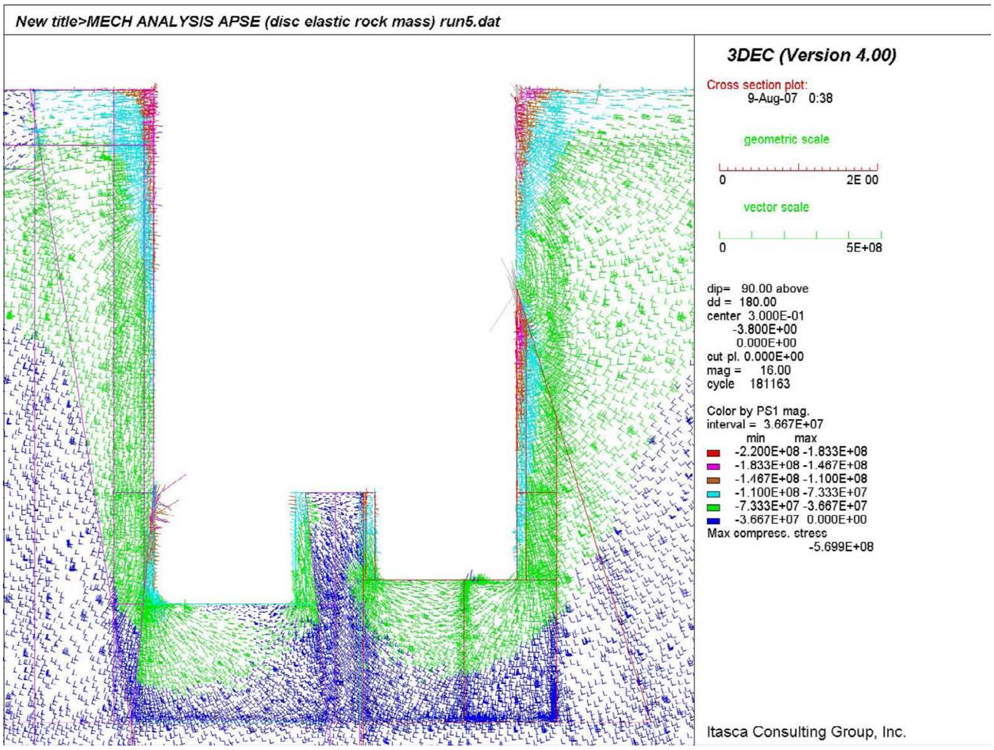

Figure 6-8. *Vertical cross-section showing the projected principal stress along the axis of the tunnel after the central pillar has been removed for case Run5 (Colors by magnitude of* σ_1*).*

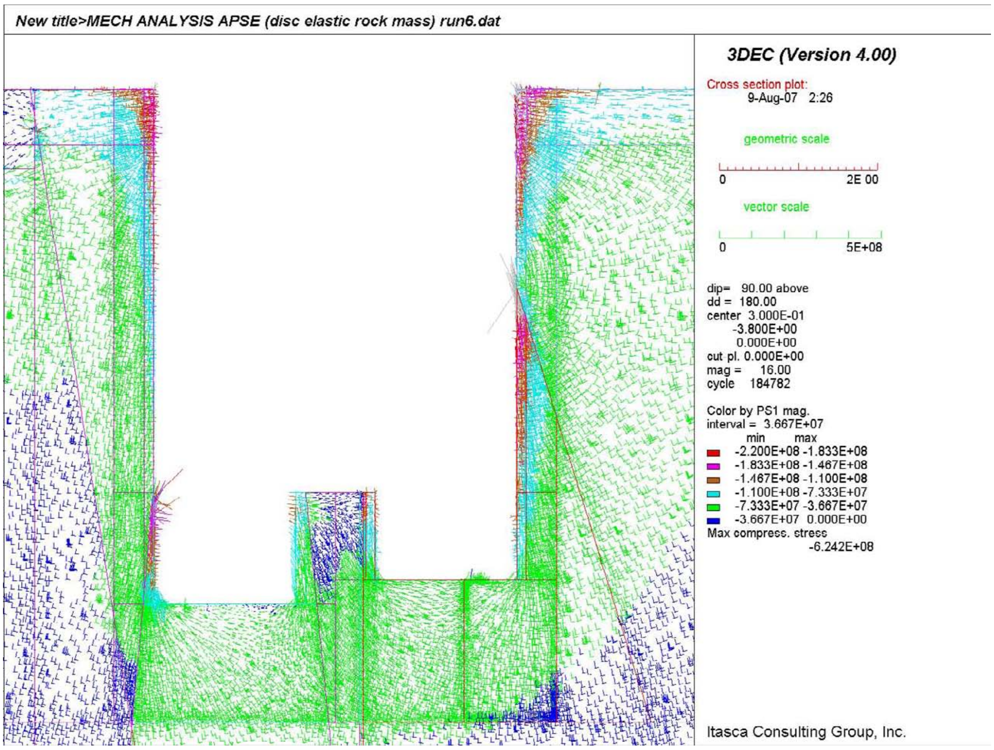

Figure 6-9. *Vertical cross-section showing the projected principal stress along the axis of the tunnel after the central pillar has been removed for case Run6 (Colors by magnitude of σ_1).*

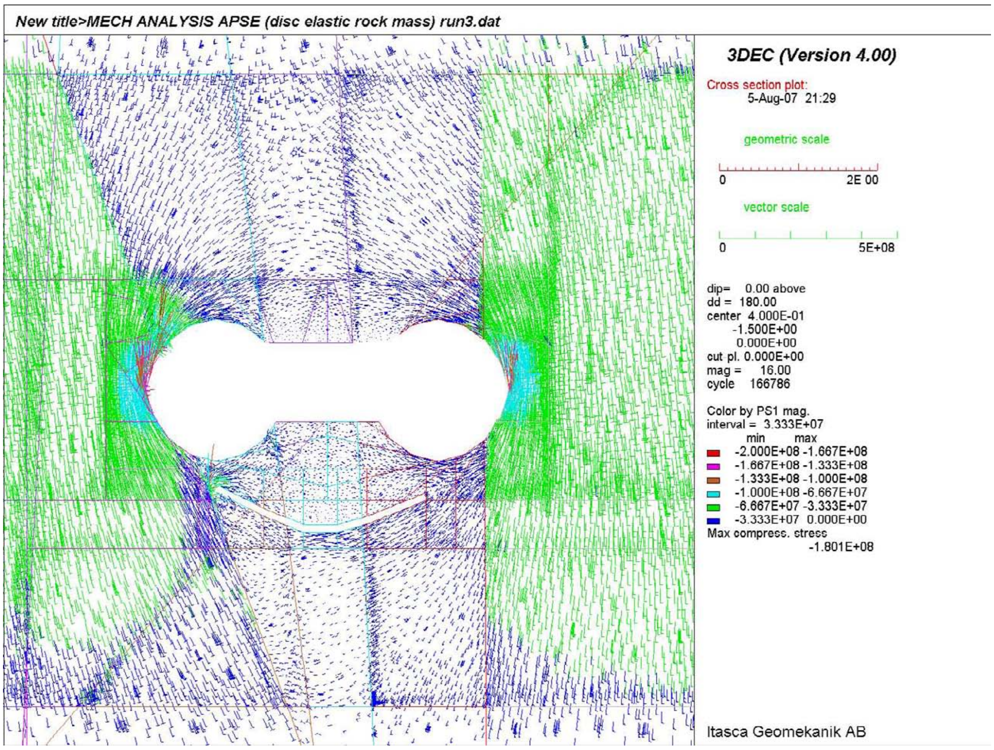

Figure 6-10. *Horizontal cross-section showing the projected principal stress at 1.5 m depth from the floor of the TASQ tunnel after the pillar has been removed for Run3 (Colors by magnitude of σ_1).*

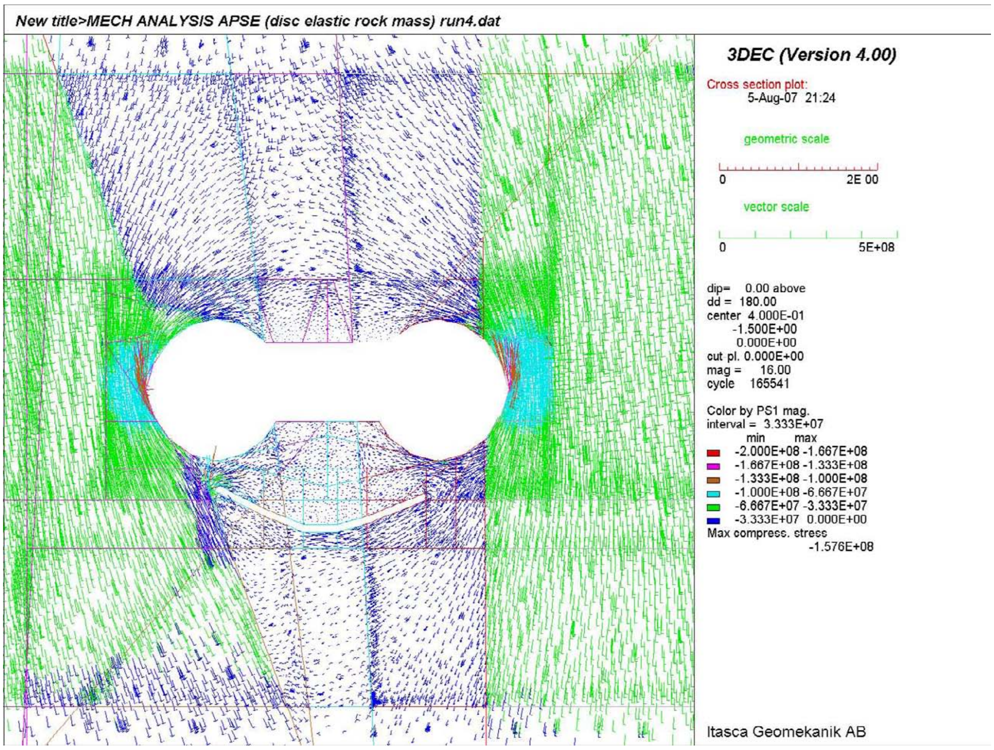

Figure 6-11. *Horizontal cross-section showing the projected principal stress at 1.5 m depth from the floor of the TASQ tunnel after the pillar has bee removed for Run4 (Colors by magnitude of σ_1).*

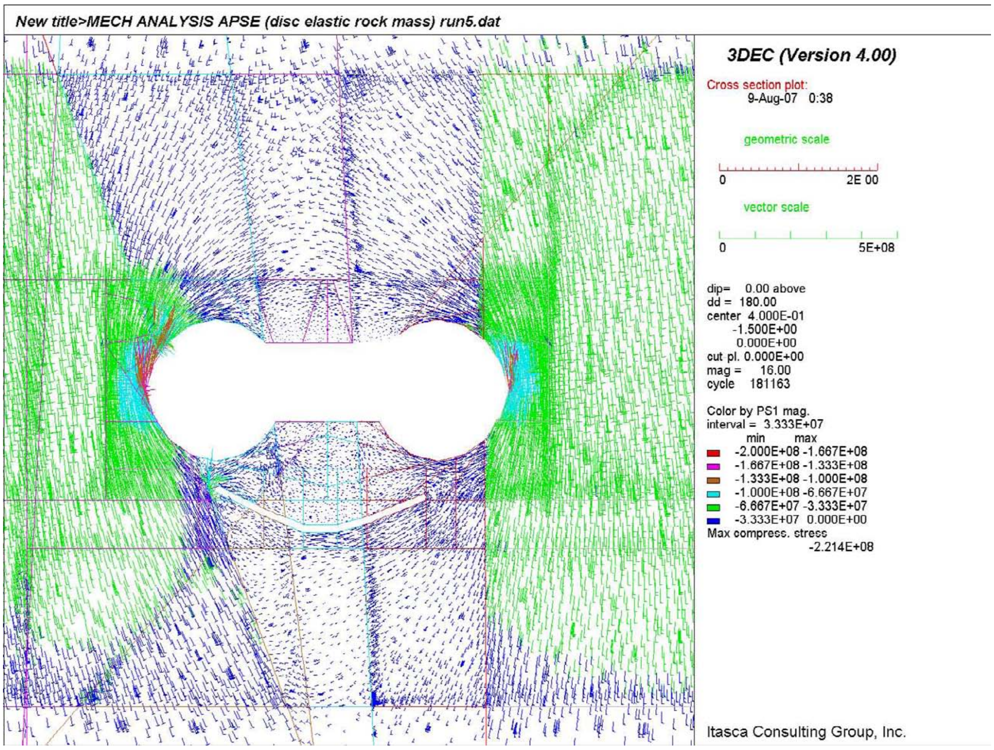

Figure 6-12. *Horizontal cross-section showing the projected principal stress at 1.5 m depth from the floor of the TASQ tunnel after the pillar has been removed for Run5 (Colors by magnitude of σ_1).*

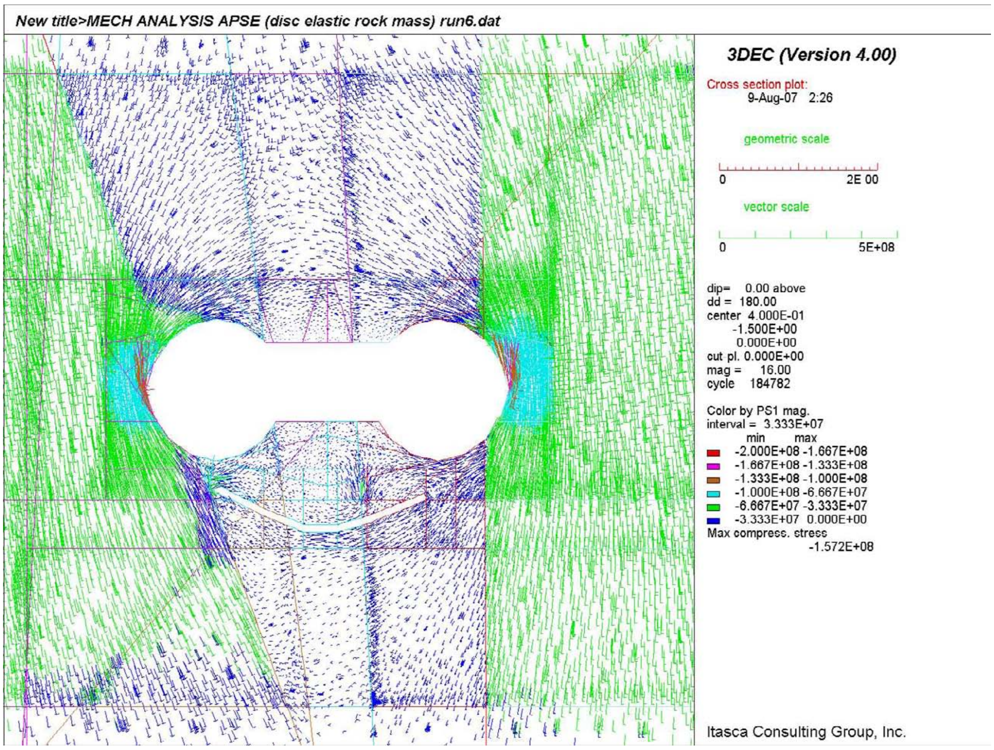

Figure 6-13. *Horizontal cross-section showing the projected principal stress at 1.5 m depth from the floor of the TASQ tunnel after the pillar has bee removed for Run6 (Colors by magnitude of* σ_1*).*

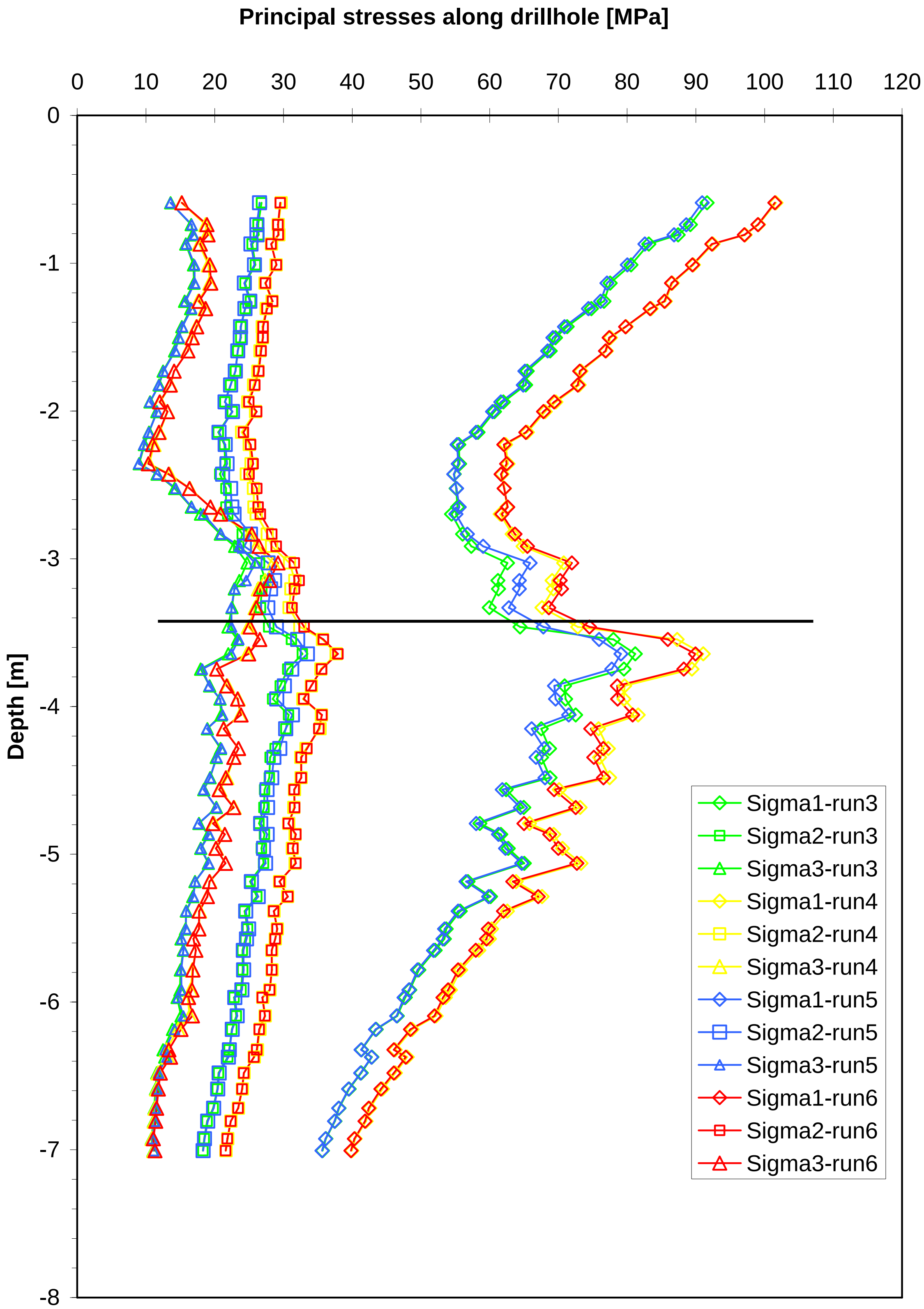

Figure 6-14. *Principal stress magnitudes corresponding to the location of borehole KQ0062G05 (A1) in the model for all the simulation cases. The black line represents the approximate intersection with the core discing fracture in Figure 3.2.*

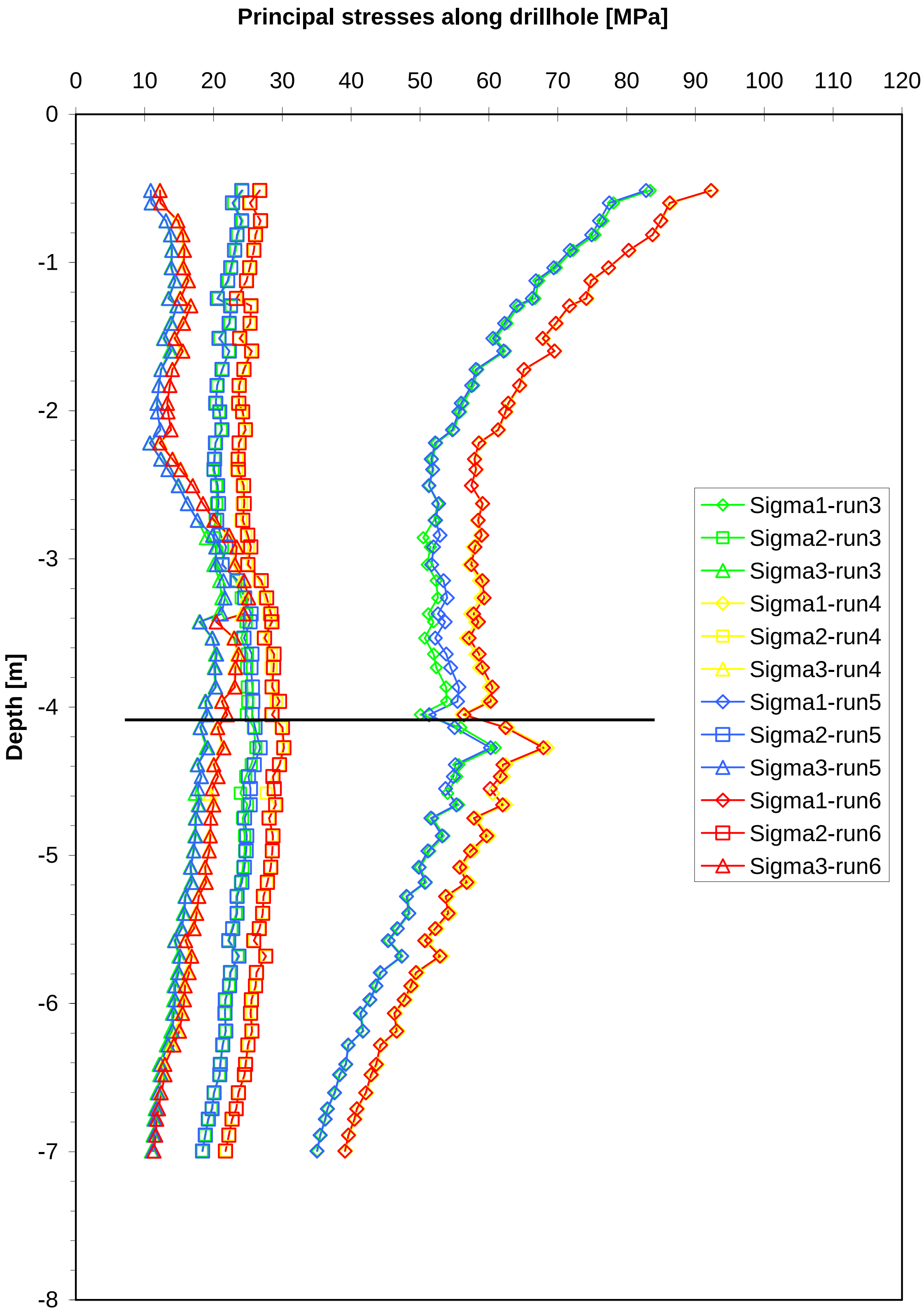

Figure 6-15. *Principal stress magnitudes corresponding to the location of borehole KQ0062G04 (B1) in the model for all the simulation cases. The black line represents the approximate intersection with the core discing fracture in Figure 3.2.*

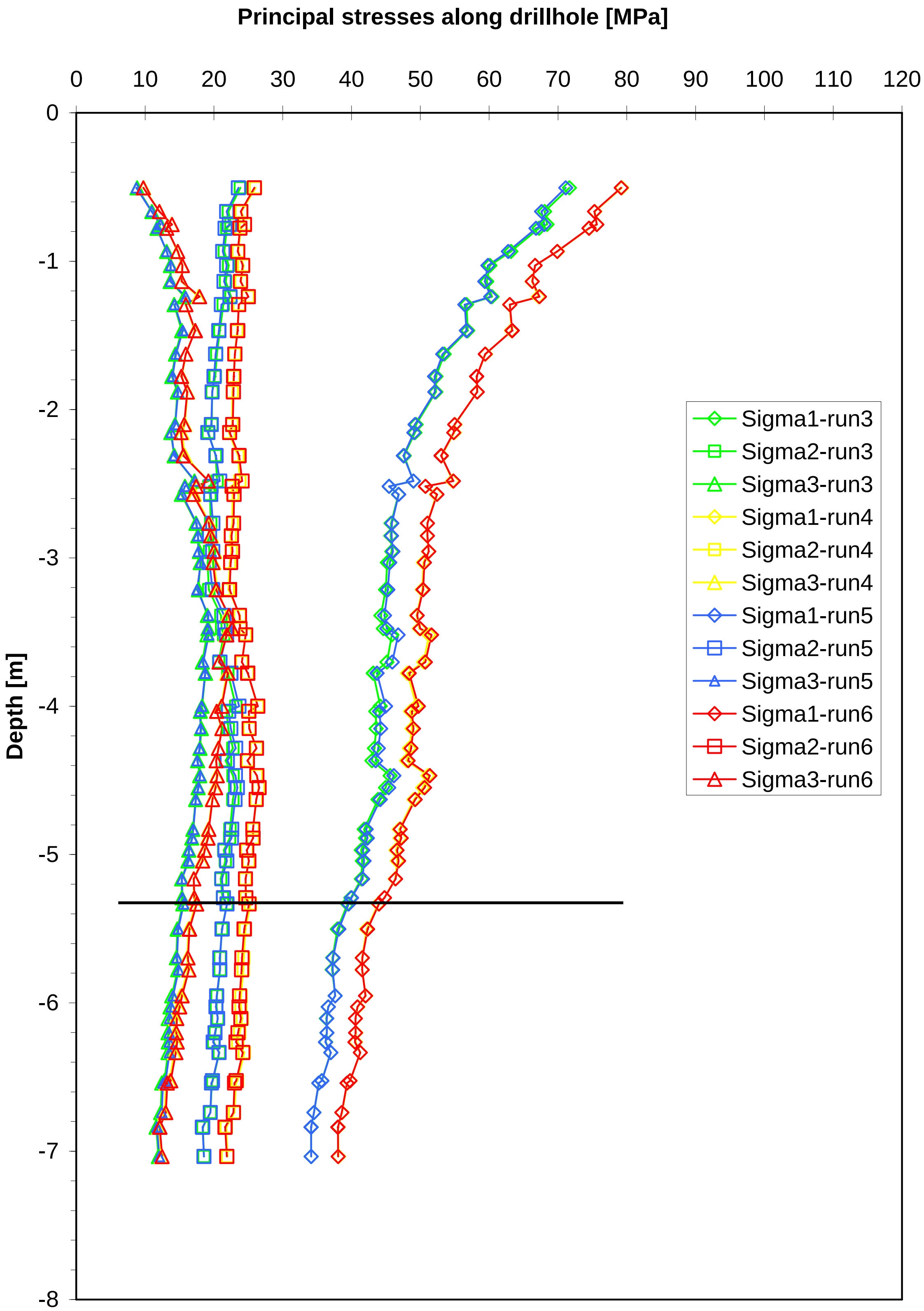

***Figure 6-16.** Principal stress magnitudes corresponding to the location of borehole KQ0061G10 (B2) in the model for all the simulation cases. The black line represents the approximate intersection with the core discing fracture in Figure 3.2.*

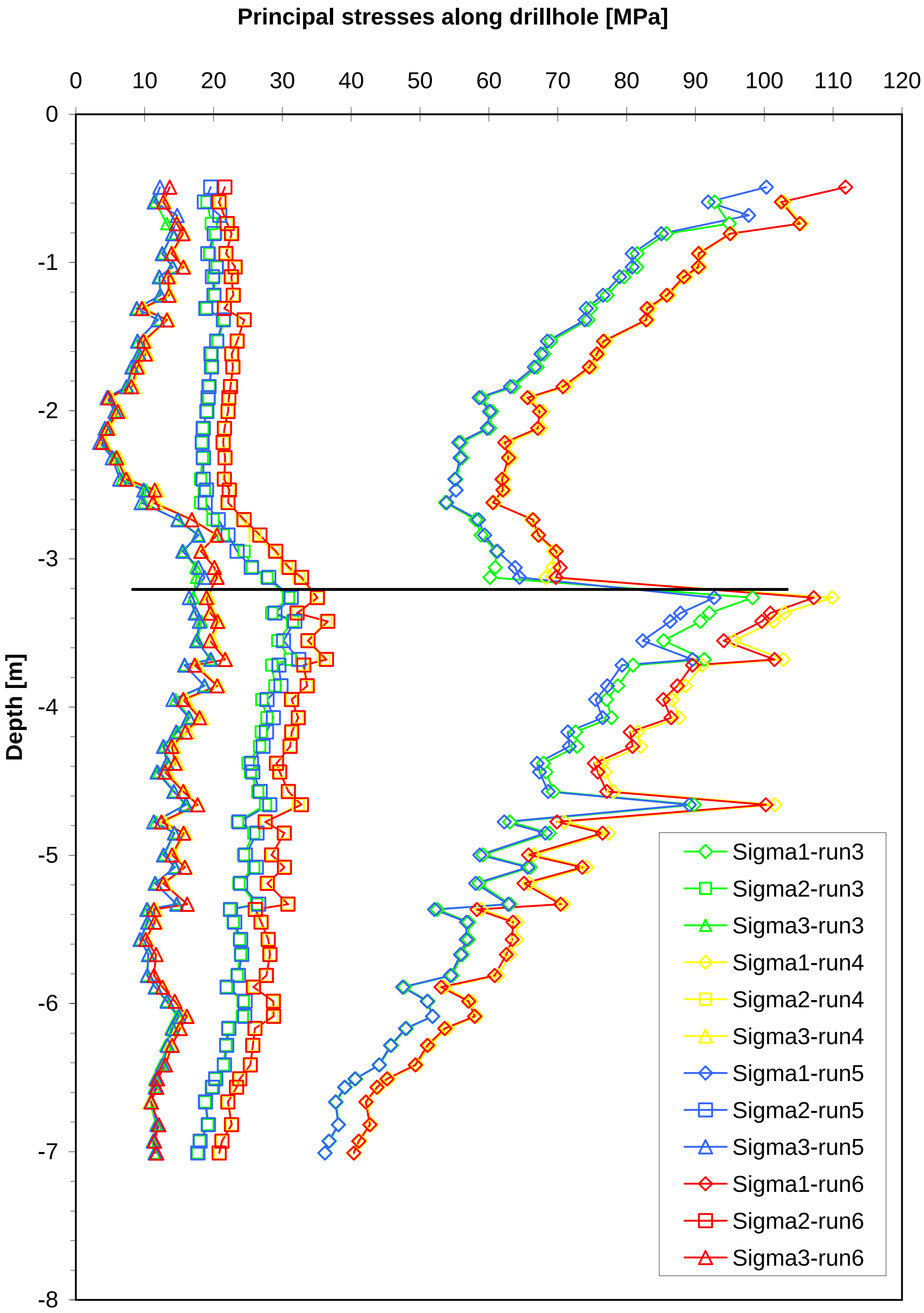

Figure 6-17. *Principal stress magnitudes corresponding to the location of borehole KQ0062G06 (C4) in the model for all the simulation cases. The black line represents the approximate intersection with the core discing fracture in Figure 3.2.*

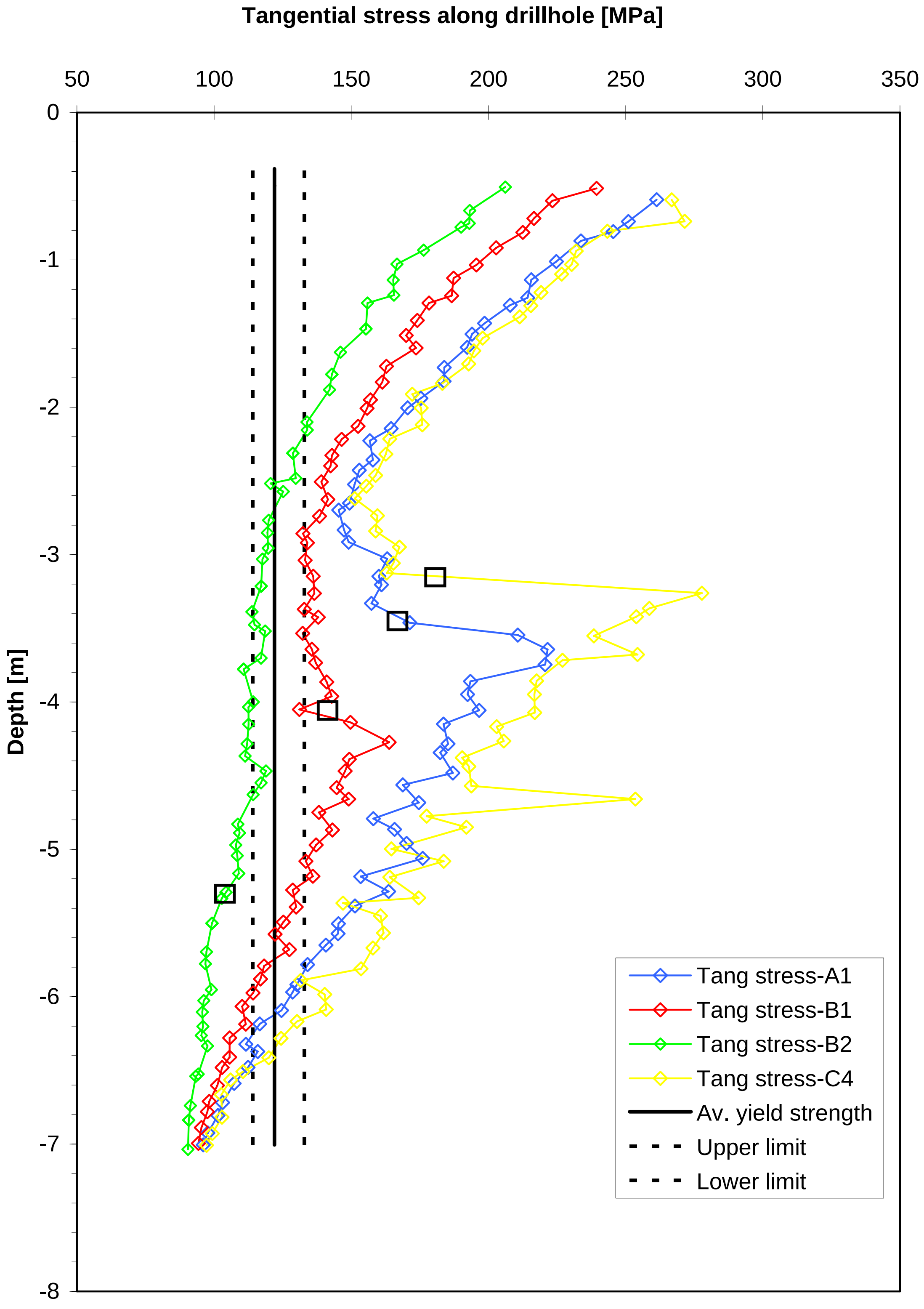

Figure 6-18. *Tangential stresses in the location of boreholes KQ0062G05 (A1), KQ0062G04 (B1), KQ0061G10 (B2), and KQ0062G06 (C4), for simulation Run3, shown together with the mean yield strength from /Andersson 2007/. The black quadrangles represent the approximate intersection with the core discing fracture in Figure 3.2.*

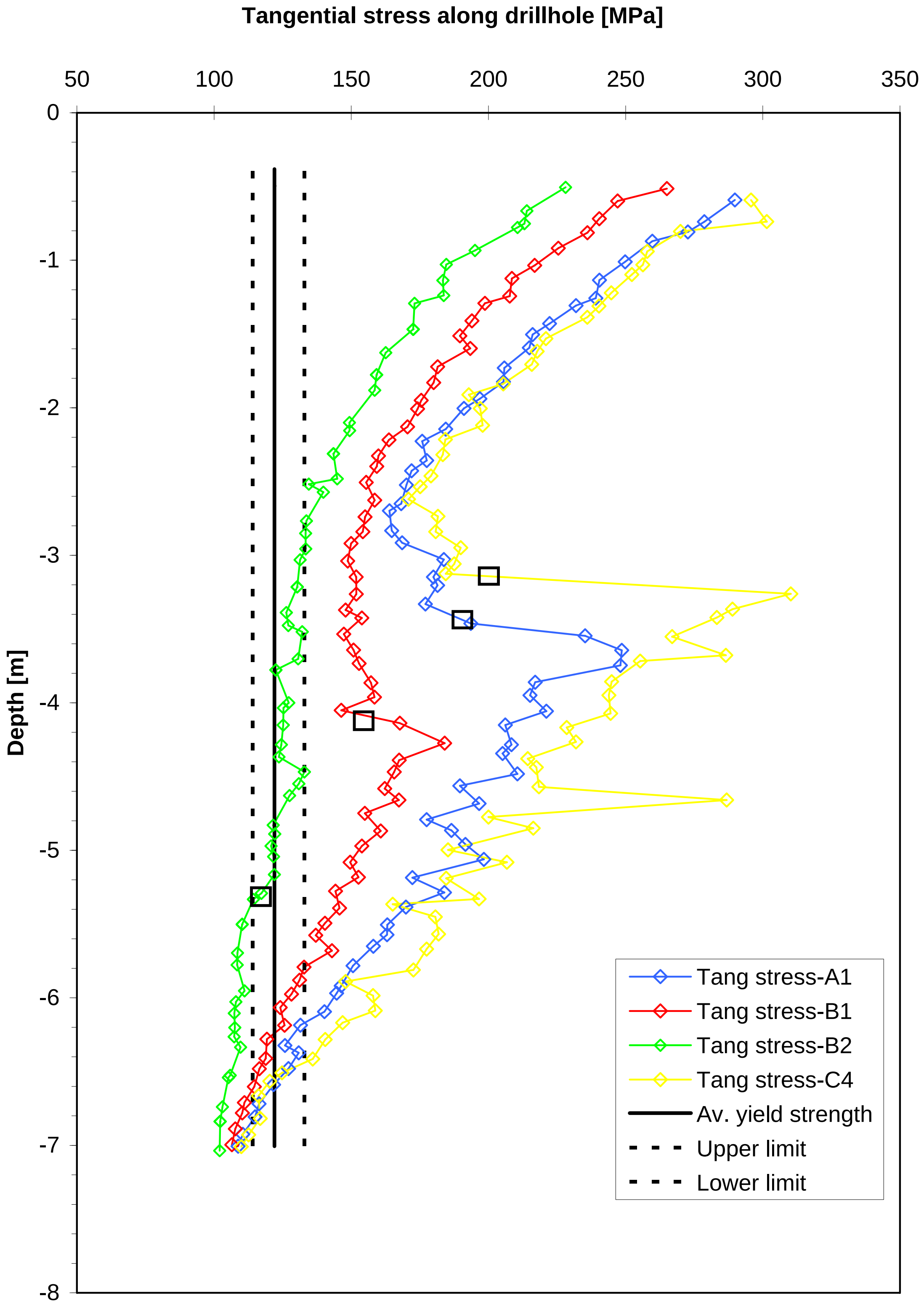

***Figure 6-19.** Tangential stresses in the location of boreholes KQ0062G05 (A1), KQ0062G04 (B1), KQ0061G10 (B2), and KQ0062G06 (C4), for simulation Run4 shown together with the mean yield strength from /Andersson 2007/. The black quadrangles represent the approximate intersection with the core discing fracture in Figure 3.2.*

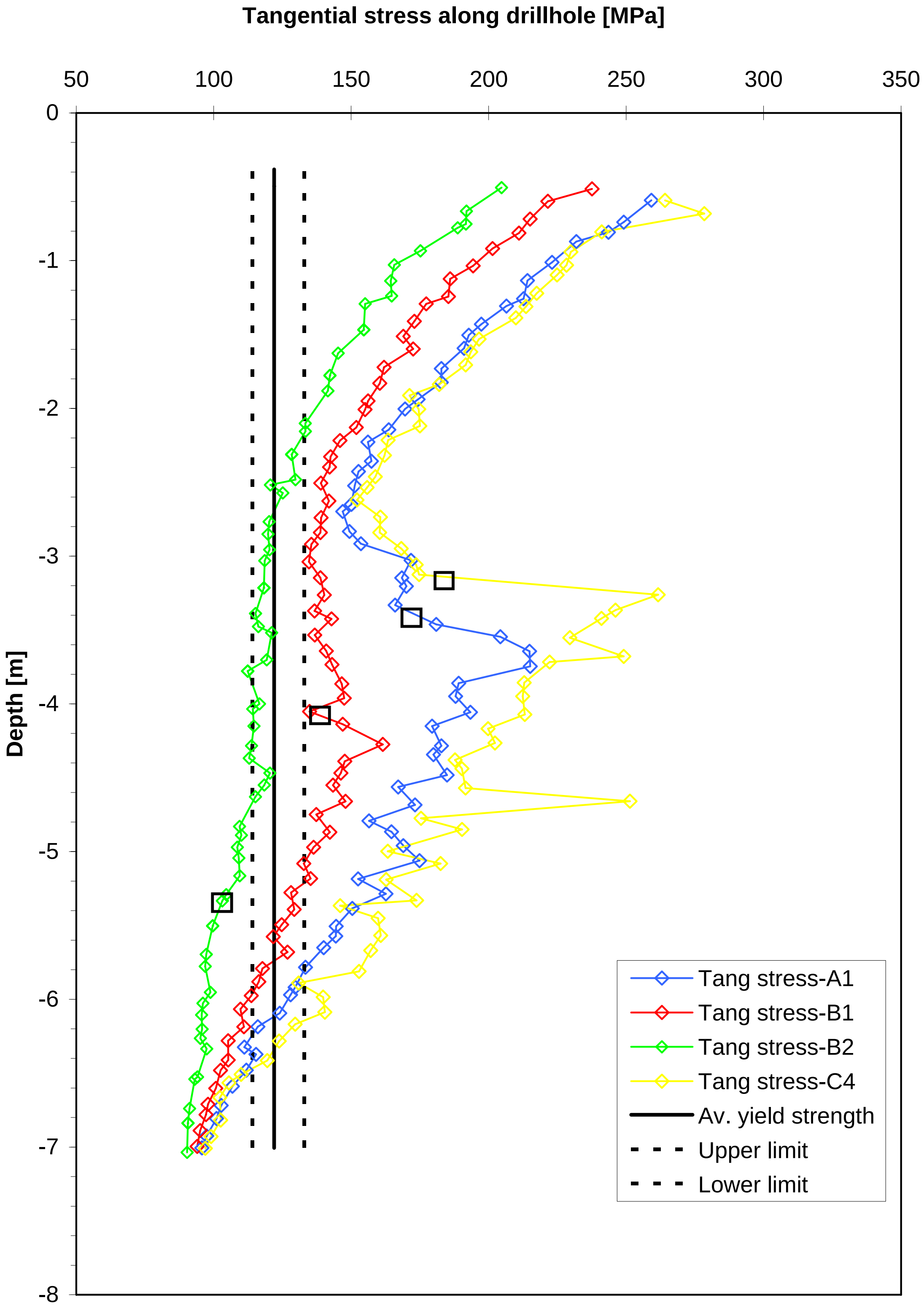

Figure 6-20. *Tangential stresses in the location of boreholes KQ0062G05 (A1), KQ0062G04 (B1), KQ0061G10 (B2), and KQ0062G06 (C4), for simulation Run5 shown together with the mean yield strength from /Andersson 2007/. The black quadrangles represent the approximate intersection with the core discing fracture in Figure 3.2.*

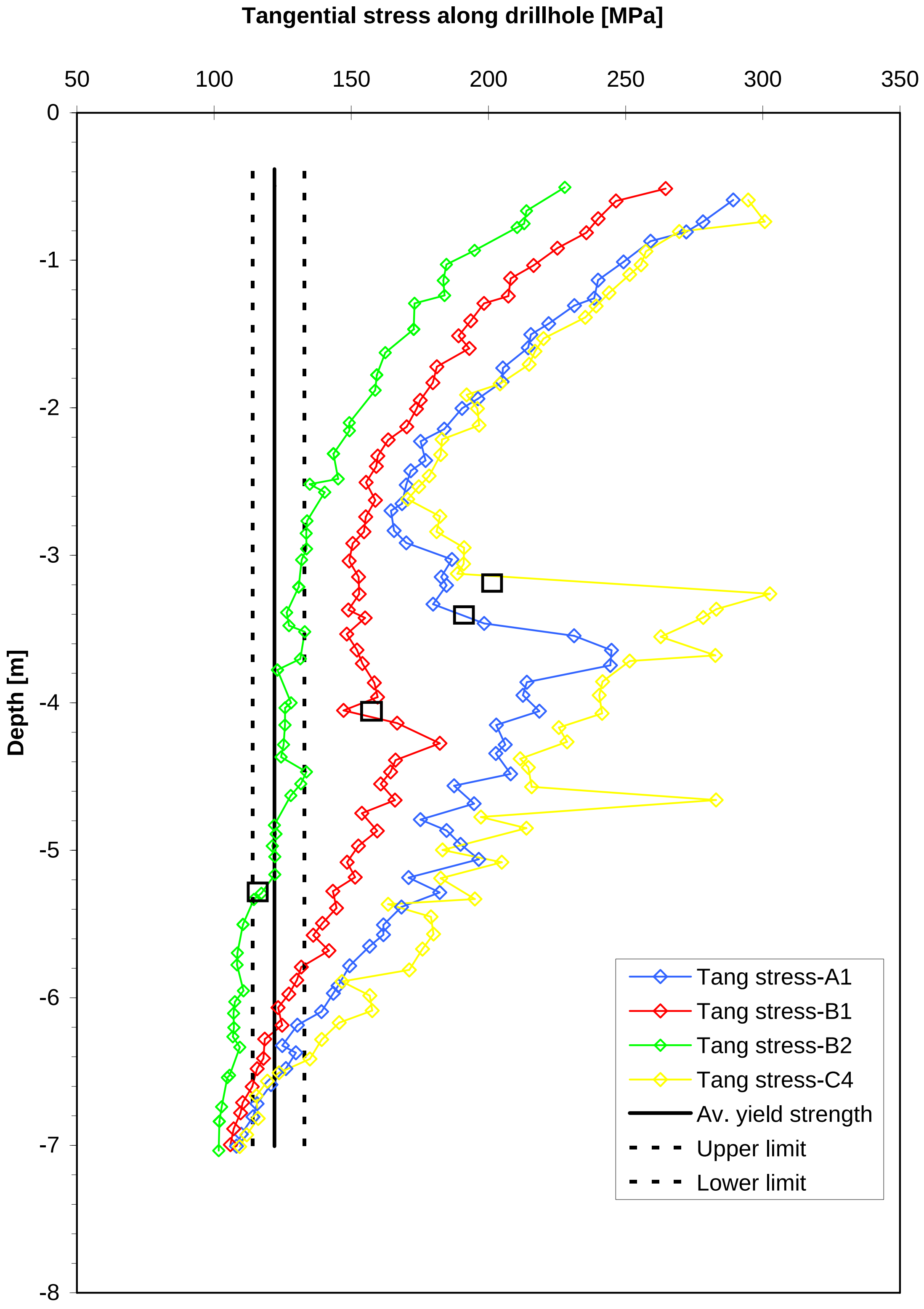

***Figure 6-21.** Tangential stresses in the location of boreholes KQ0062G05 (A1), KQ0062G04 (B1), KQ0061G10 (B2), and KQ0062G06 (C4), for simulation Run6 shown together with the mean yield strength from /Andersson 2007/. The black quadrangles represent the approximate intersection with the core discing fracture in Figure 3.2.*

6.3.2 Simulated fracture displacement

During the drilling of the de-stressing slot (see Figure 3-1) normal and shear displacements were monitored at different locations along fractures 08 and 14 /Mas Ivars, 2005/. Figure 6-22 and Figure 6-23 show the measured field displacements.

The simulated normal and shear displacements during the de-stressing of the pillar at the APSE site were monitored at 0.3 and 2.5m depth in fractures 08 and 14 (Figure 3-1). The modeling results are shown in Figure 6-24 through Figure 6-27.

Although the normal and shear displacement of fracture 08 at 2.5m depth failed to be recorded in Run6, the general trend and the final values of the simulated normal displacement in every modeling case (Figure 6-24 and Figure 6-25) compares relatively well with the normal displacement monitored in the field (Figure 6-22). The largest normal fracture opening is registered in fracture 08 at 2.5m depth in the modeling cases and at 2.6m depth in the field. The normal displacement in fracture 08 seems to decrease when we get closer to the surface of the tunnel. In fracture 14, the modeled normal displacements show small closure, similar to what was recorded in the field.

As in the case of the fracture normal displacement, the general trends and the final values of the simulated fracture shear displacement (Figure 6-26 and Figure 6-27) and the one monitored in the field (Figure 6-23) agree relatively well. However, there seems to be a better agreement for the simulation cases Run3 and Run5 in which the lower *in situ* stress option was used (see Table 6-5). The cases Run 4 and Run6 seem to overestimate the final value of the fracture shear displacement.

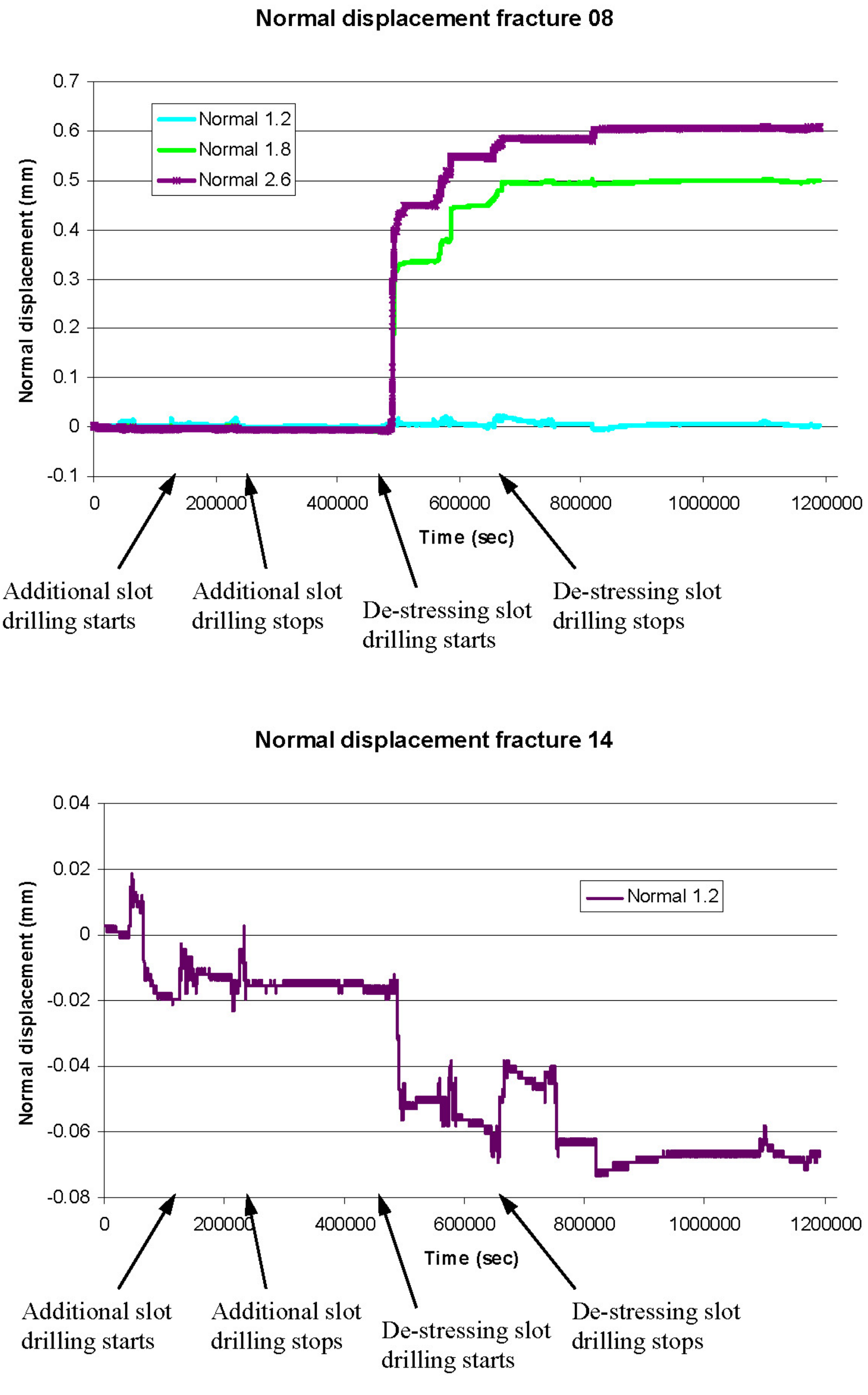

Figure 6-22. *Monitored normal displacement at different depths in fractures 08 and 14 during the de-stressing of the APSE pillar /Mas Ivars, 2005/.*

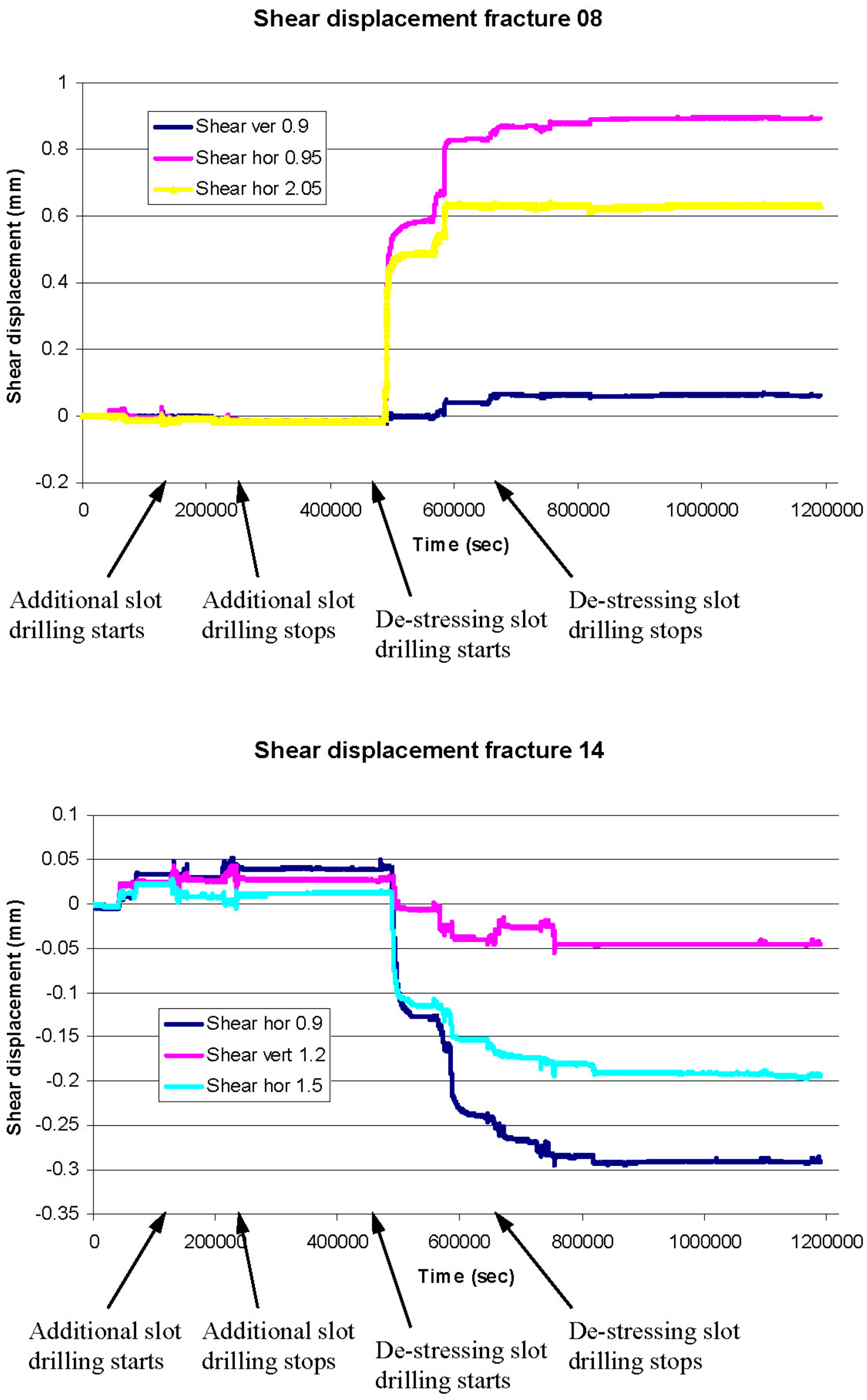
Shear displacement fracture 08

Additional slot drilling starts

Additional slot drilling stops

De-stressing slot drilling starts

De-stressing slot drilling stops

Shear displacement fracture 14

Additional slot drilling starts

Additional slot drilling stops

De-stressing slot drilling starts

De-stressing slot drilling stops

Figure 6-23. *Monitored shear displacement at different depths in fractures 08 and 14 during the de-stressing of the APSE pillar /Mas Ivars, 2005/.*

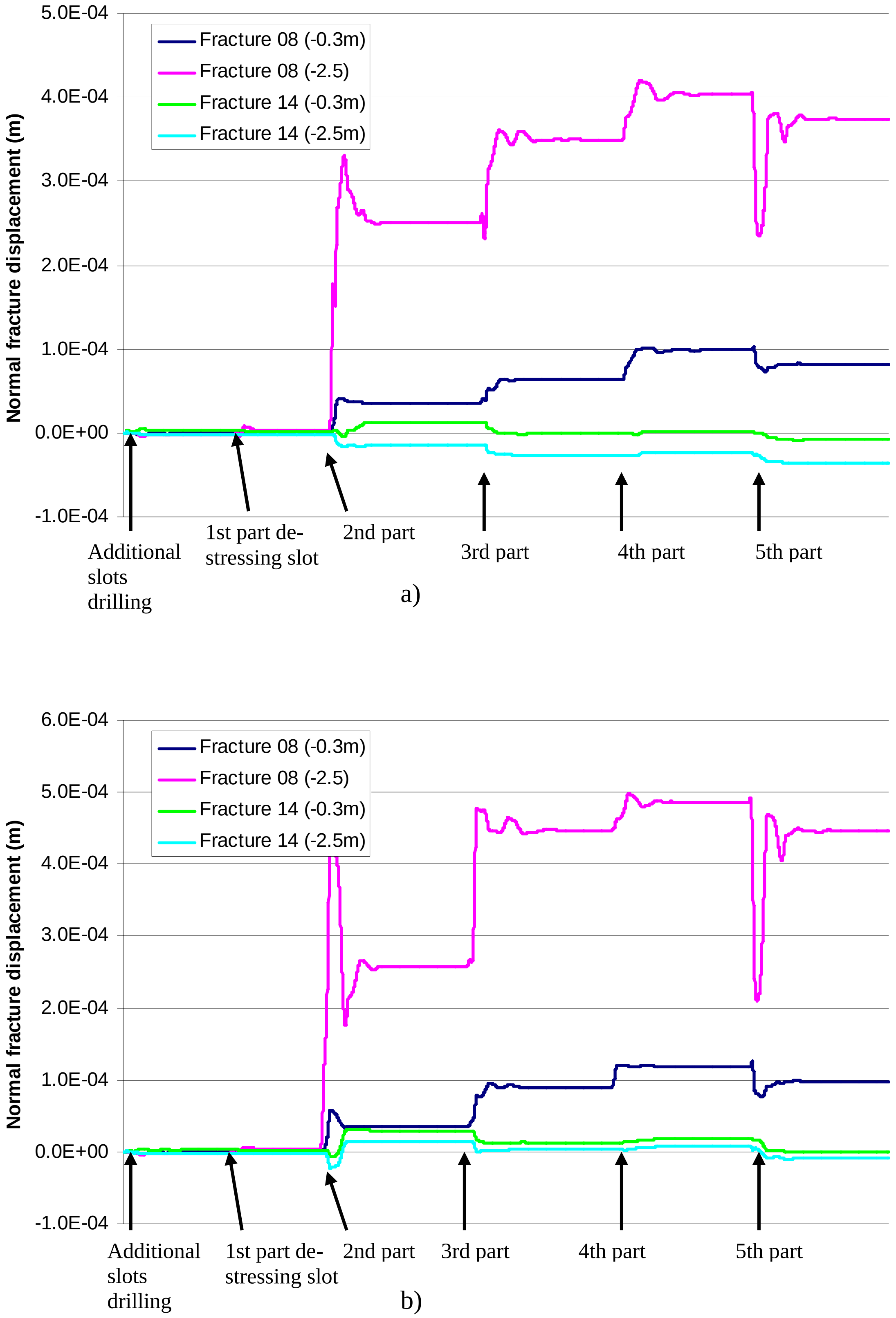

Figure 6-24. *Modeled normal displacement at different depths in fractures 08 and 14 during the de-stressing of the pillar for a) Run3 and b) Run4.*

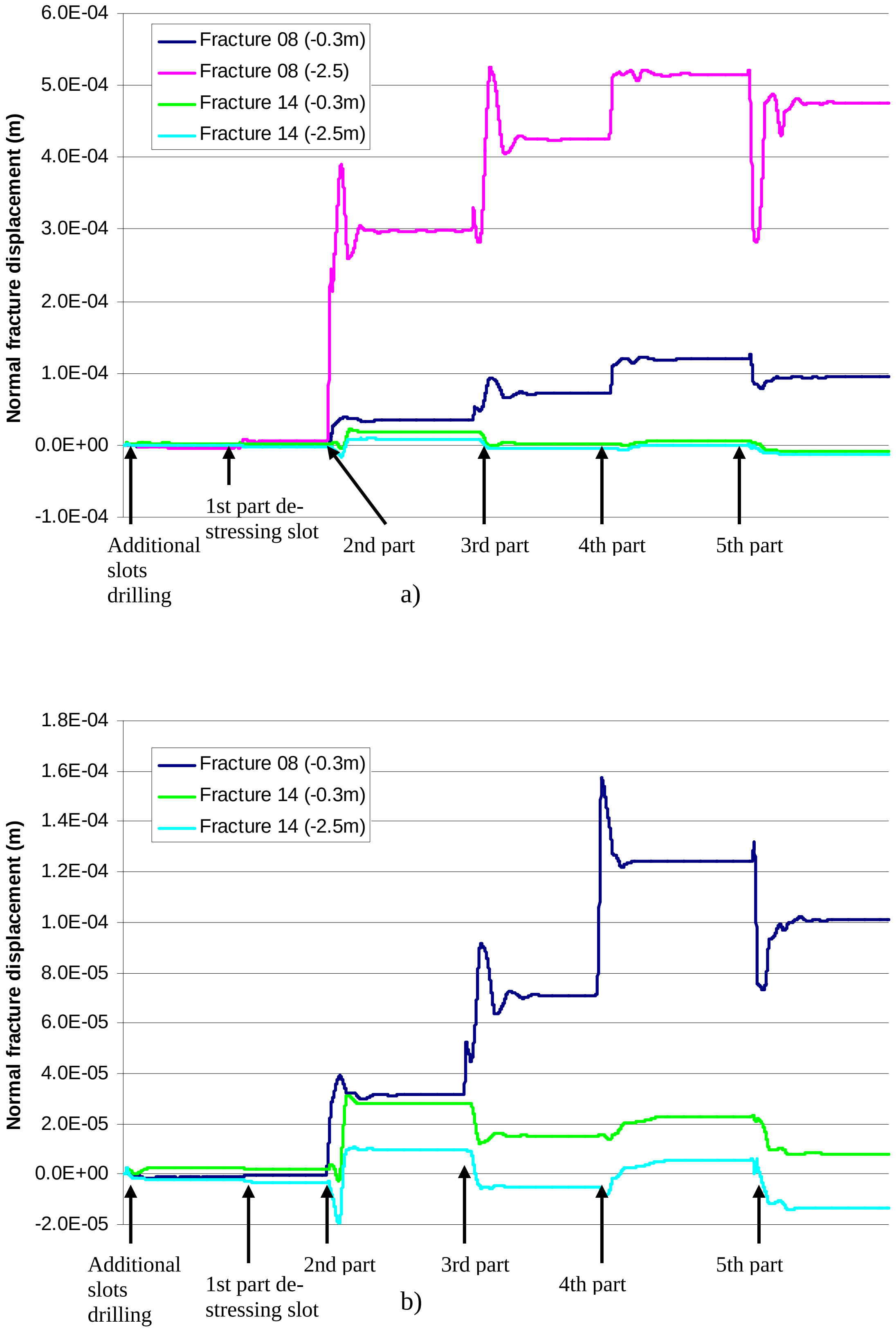

Figure 6-25. *Modeled normal displacement at different depths in fractures 08 and 14 during the de-stressing of the pillar for a) Run5 and b) Run6 (fracture 08 at 2.5m depth missing).*

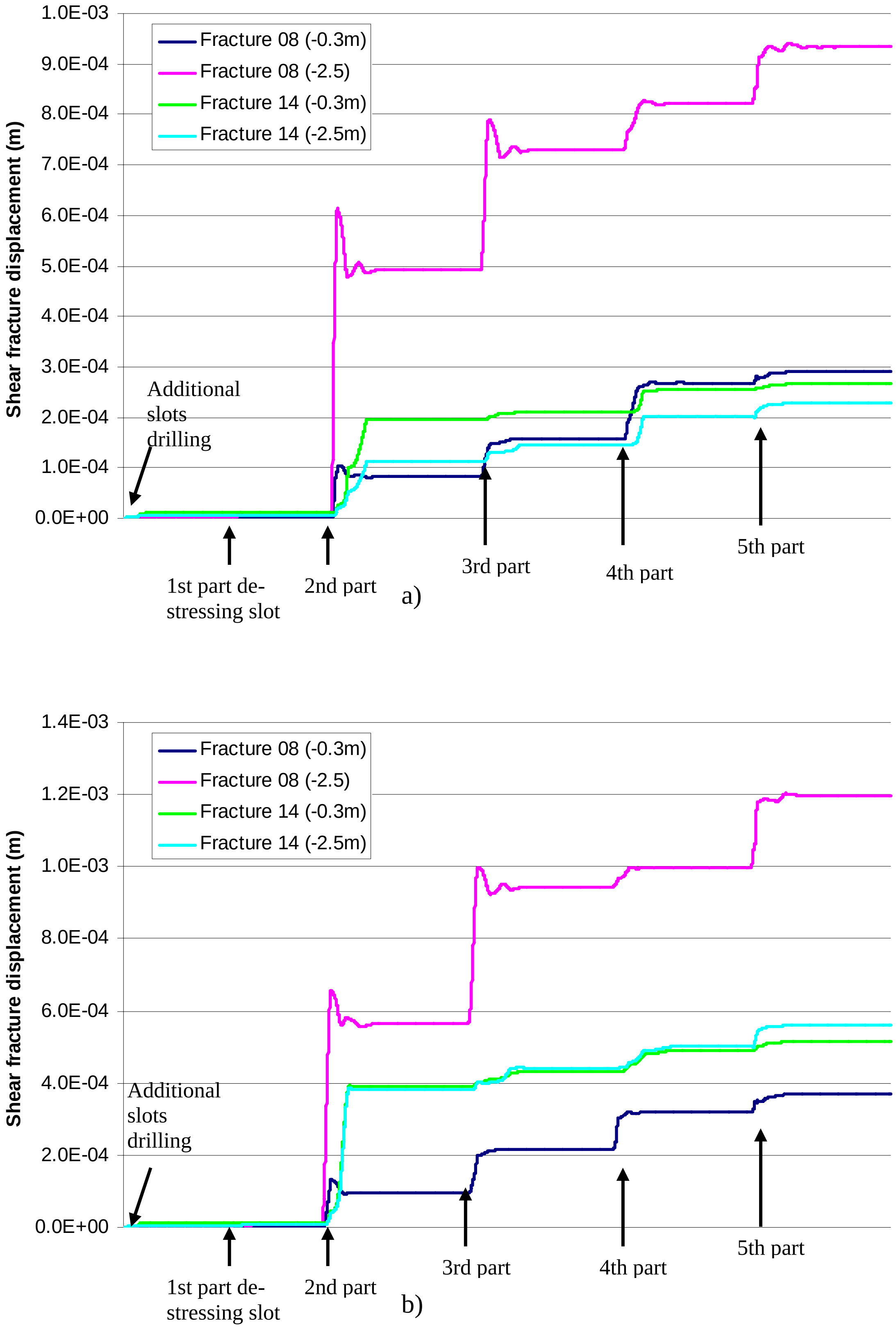

Figure 6-26. *Modeled shear displacement at different depths in fractures 08 and 14 during the de-stressing of the pillar for a) Run3 and b) Run4.*

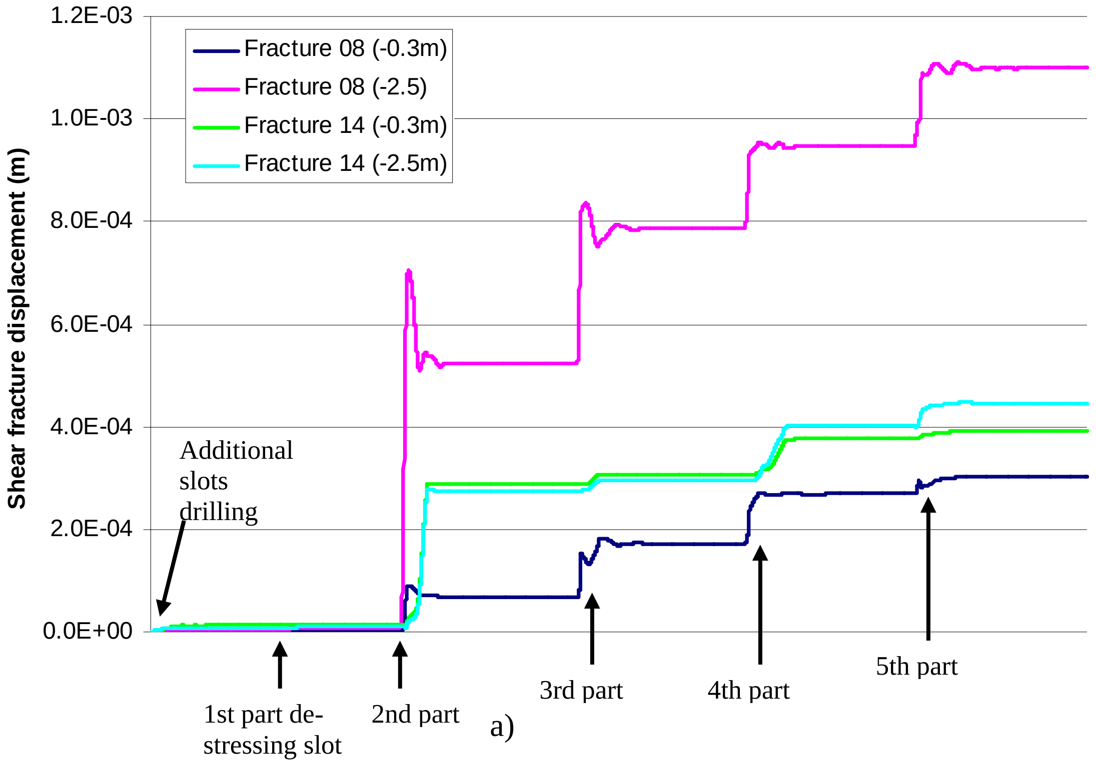

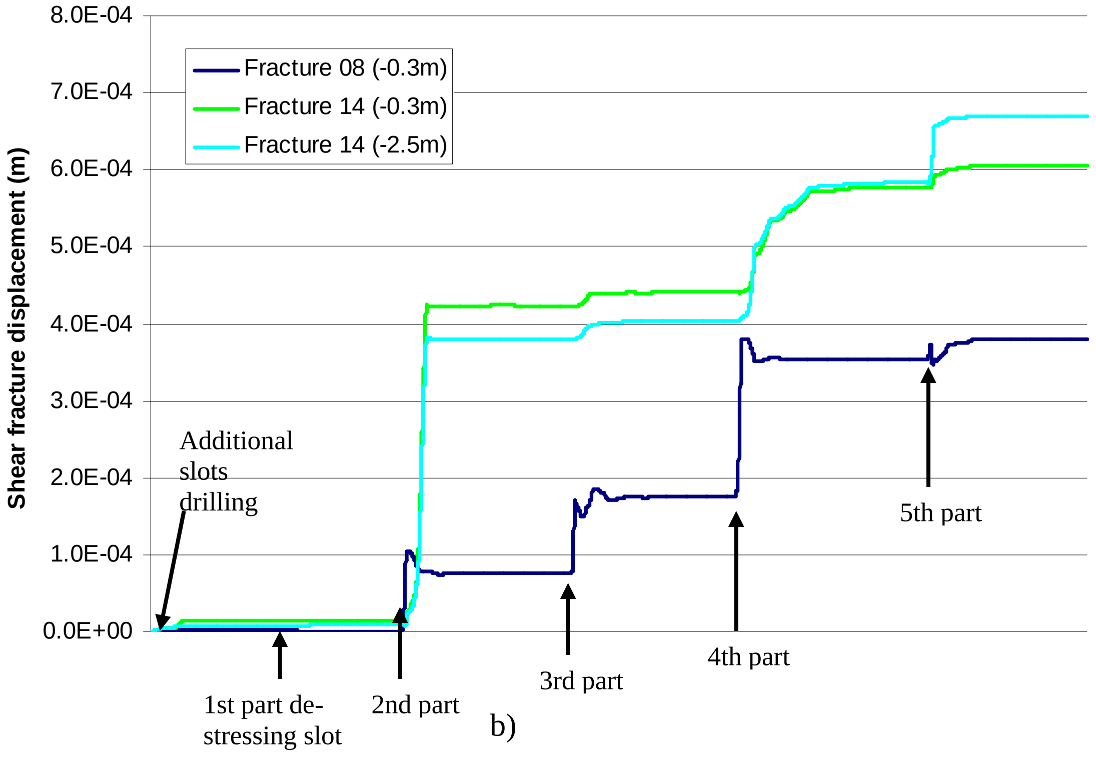

Figure 6-27. *Modeled shear displacement at different depths in fractures 08 and 14 during the de-stressing of the pillar for a) Run5 and b) Run6 (fracture 08 at 2.5m depth missing).*

7 Summary analysis and discussion

7.1 Core disking

The scarcity of core disking observations is an indication that stresses are lower than what was anticipated based on the numerical modeling performed prior to this study. The observed disking (Table 4-1) comprised disk thicknesses ranging from 5 to 30 mm. Taking an estimated average disk thickness of 15 mm, and using the nomograms of /Hakala, 1999a/, this would indicate a maximum horizontal stress of around 75–80 MPa. However, this would only apply locally, as disking was only observed over a distance of 0.1–0.2 m in each borehole, with the exception of the first test hole, where disking was found over 0.5 m distance.

The lack of core disking implies the stresses are lower than a certain value. Again, using the nomograms of /Hakala, 1999a/, this limit may be estimated as

$$\sigma_H = 4\sigma_t \ .$$

With σ_t = 15 MPa (Table 4-3), and upper limit of σ_H = 60 MPa applies in areas with no core disking.

Taken together, the observations indicate that stresses are highest closest to the deposition hole, as the longest stretch of core disking was observed in borehole KQ0062G01 closest to the deposition hole. Also, no disking was found in boreholes KQ0062G04 and KQ0061G10, located farther away from the deposition hole. However, stresses are not high enough to cause systematic core disking, which implies that maximum horizontal stress is, generally, less than approximately 60 MPa (prior to drilling the holes), at the location of these boreholes.

What was evident from this study is the strong link between observed core disking and the occurrence of subvertical fractures intersecting the boreholes. A fracture crosses the core disking areas in all three boreholes, as shown in Figure 7-1 . However, in borehole KQ0062G06, core disking occurred at several locations, not only associated with subvertical fractures. It may be speculated that stresses along this borehole are slightly higher, due its closer proximity to the deposition hole, thus resulting in several core disking occurrences. However, this hypothesis cannot be verified from the presently available data.

At the site investigation at Forsmark, it has often been found that core disking correlates (to some extent) with the length of the core barrels. The data from the present study does not indicate such a correlation. It should be noted, however, that the drilling rigs used at Forsmark and in the present study, are very different. There were large practical problems to achieve sufficient feed force for overcoring; however, this may not have influenced the occurrence of core disking, although this cannot be verified using the available data. No registration of drilling parameters was conducted.

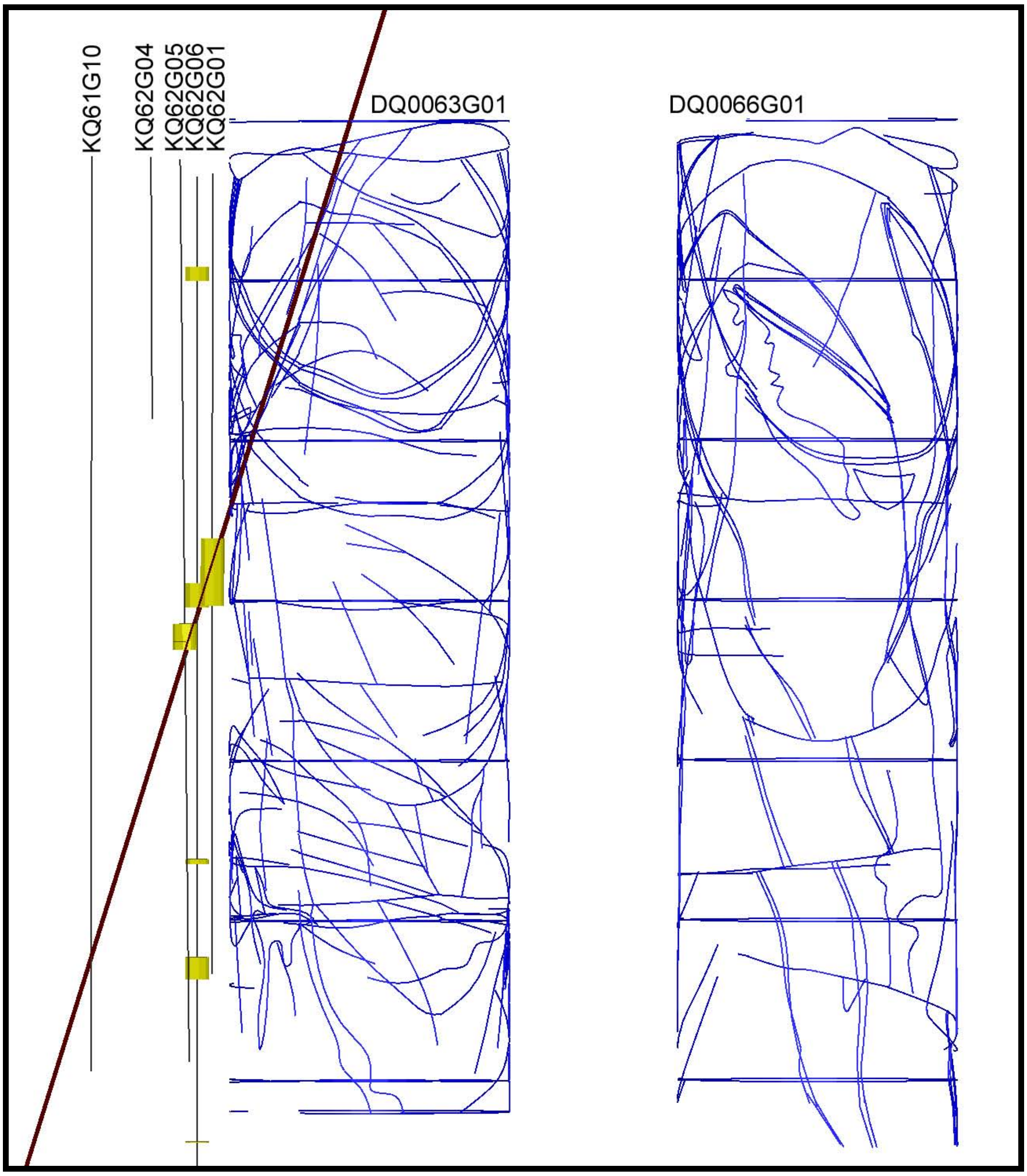

Figure 7-1. *Core disking (yellow cylinders) in boreholes KQ0062G01, KQ0062G05, and KQ0062G06, in the vicinity of deposition hole DQ0063G01, shown together with subvertical fracture (dark red).*

7.2 Borehole breakouts

The few observations of borehole breakouts are a further indication that stresses are not particularly high in the test volume. Under the assumption that the observed borehole wall damages are manifestations of spalling-type failure in mineral-grain scale had occurred at the borehole wall, the virgin stress state causing failure can be estimated. In /Andersson, 2007/ the average value of the rock spalling strength was determined as 118 MPa (virtually the same as the crack initiation stress). Using the Kirsch solution for the stresses at the boundary of a circular opening, one thus obtains the following criterion for borehole breakouts:

$$3\sigma_H - \sigma_h = 118.$$

The value of the minimum horizontal stress must be assumed. Using the results from numerical modeling, an upper limit appears to be 30 MPa (cf. Chapter 6). Using $\sigma_h = 0$ as a lower limit, one finds that:

$$39 < \sigma_H < 49 \text{ (MPa)}$$

Since borehole breakouts only occurred at a few, isolated, locations (see Section 4.3), it is likely that stresses (prior to drilling the holes) are lower than these values for the majority of the rock mass volume at the test site. This finding may also be illustrated as calculated tangential stresses at the borehole walls, as shown in Figure 6-18 through Figure 6-21, which show that the yield (spalling) strength is reached at the borehole wall along the majority of the borehole lengths. Since this is not observed in reality, it can be concluded that ether (i) the boundary stress conditions are not correct (Table 6-2), or (ii) the model does not capture the full stress-path of the test site correctly (more on this in Section 7.4 below).

7.3 Overcoring measurements

The confidence in the conducted overcoring stress measurements is judged to be low to moderate, primarily due to difficult measurement conditions. Measurements were heavily affected by the presence of subvertical, sometimes open, fractures, in addition to practical difficulties in the measurements (most notably drilling problems). Only one measurement can be regarded as moderately reliable.

This result is compared to previously conducted stress measurements in the area in Table 7-1. Stress orientations are similar in all measurements, which is to be expected as the tunnel axis was oriented roughly perpendicular to the maximum stress (to obtain maximum stress influence). The major stress orientation remains the same after tunnel excavation, excavation of deposition holes and removal of pillar. Stress magnitudes are, however, significantly lower in the latest measurements, despite these being taken close to the deposition hole (previous measurements were in undisturbed conditions thus reflecting the virgin stress state). No core disking was observed in borehole KQ0061G10 where stress measurements were made.

Although the measurement conducted is regarded as only moderately reliable, the results are, nevertheless, in line with those derived from core disking and borehole breakout observations above, i.e., that stresses are significantly lower than expected, and also lower than indicated from the numerical modeling of Chapter 6.

Table 7-1. Comparison of current and previously conducted stress measurements in the test area, partly from /Jansson & Stigsson, 2002/ and /Sjöberg, 2002/.

Borehole no.	Method *)	σ_H (MPa)	σ_h (MPa)	σ_v (MPa)	Trend σ_H (°)
KF0093A01	OC	25.7	10.7	18.0	125
KA3376B01	OC	29.9	12.4	13.9	137
KA2599G01	HF	21.8	11.0	-	131
KF0093A01	HF	-	11.0	19.8	127
KQ0061G10	OC	14.3	1.8	8.8	123

*) OC = overcoring using the *Borre* probe
HF = hydraulic fracturing

7.4 Stress modeling

The numerical model showed high stresses near the tunnel floor. In reality it is likely that the tunnel floor is destressed to a depth of around 0.5 m /Andersson, 2007/ due to excavation-induced damage. This was not simulated in the present model. A test run with fictitious fractures at the location of the destressed zone gave destressing in this portion, but virtually similar stresses in the portion below the destressed zone. Hence, the present modeling is physically more correct, by just disregarding the high-stress zone to about 1 m depth.

The stress modeling clearly showed stress discontinuities over the steeply dipping fracture in the core holes. This can be qualitatively correlated with observed disking. Slightly elevated stresses above and below the fracture coupled with (potentially) weaker rock near the fracture may be a reason for observed core disking. However, a quantitative correlation with respect to exact location of core disking, or in terms of stress level, could not be obtained.

It appears that stresses, in general, are much higher in the numerical model than field observations and measurements indicate. One reason for this may be that the model does not replicate the excavation-loading history, and its effect on the rock, correctly. This involves excavation of the tunnel, followed by excavation of the deposition holes, thermal loading and unloading, drilling of destressing slot, and finally, removal of the pillar between the deposition holes. In the numerical modeling, all stages except the thermal loading was included (which was assumed to be transient). More importantly, only linear-elastic modeling was conducted; hence, no permanent effects of reaching the rock strength could be captured by the model.

It may be argued that the rock in the area does not behave in a true plastic sense; rather, it displays brittle behavior. However, the results of rock failure is that the rock in question cannot take any additional load, thus redistributing stresses to other portions of the rock mass. This effect can only be simulated using a plastic type of constitutive model in numerical analysis (strain-softening may also be considered). The possible effects of the destressing and removal of the pillar must also be simulated in a plasticity model, in which all sequences of excavation and loading are included. This requires considerable efforts, as great care must be taken to simulate all relevant events (result will be path-dependent), and was outside the scope of the present work. It should also be realized that a basic continuum model with some discontinuities included is probably the only realistic choice for such a task. However, it may also become difficult to explain all observations (from both the APSE study and the core disking boreholes) in a single model.

7.5 Discussion

The conducted work proved that determination of stress levels at which core and ring disking occurs is no small feat. Despite careful planning and what, at the beginning, appeared to be a good test site, it was not possible to fulfill this primary objective of the project work.

It appears that the sparse occurrence of core disking can be attributed to two major factors: (i) lower stresses than expected in the test volume, and (ii) heterogeneous geology. The first may be due to destressing occurring as a result of the complex excavation and loading history of the APSE test area. As discussed above, not all aspects of this sequence was simulated in the numerical model. The second factor (heterogeneous geology) affects the stress distribution in the area, making it more discontinuous (as evidenced by the conducted stress analysis). Together, these two factors may cause lower, and more varying, stresses in the test area, than originally anticipated. Locally, high stress may develop (such as near subvertical fractures) and this, coupled with possibly weaker rock near fractures, may be the cause of locally occurring core disking.

It should be noted, however, that the mechanisms at work have not been fully resolved. Only a qualitative explanation is offered here. The lack of more observations and hard data preclude verification.

One of the aims of the work was also to evaluate methods for estimating stresses from core disking observations. Given the few and sporadic observations of disking, this could not be achieved in full. Since stress conditions are not known, it cannot be stated whether the nomograms of /Hakala, 1999a/ provide realistic results or not. However, if stresses in the area still are similar to those back-calculated in the APSE-project /Andersson, 2007/, extensive and systematic core disking would have resulted. The influence from structures, nor the highly heterogeneous geology, obviously cannot be explicitly accounted for in the nomograms of /Hakala, 1999a/.

Perhaps a larger problem is that the mechanisms for core disking still remain partly unresolved, in particular in cases with complex geology and structural conditions. The available methods, such as that of /Hakala, 1999a/ or /Lim et al, 2006/ are, in many ways, too simplistic. However, a refinement of these requires better knowledge about the governing mechanisms for core disking and ring disking.

The idea pursued in this work for determining stress levels for core disking occurrence, is still considered relevant. However, to improve on the results, it is desirable that as many as possible of the factors contributing to core disking are kept constant. It would be necessary to find a test site with more homogeneous geological conditions, preferably in virtually fracture-free rock. The findings of this study have clearly shown that fractures strongly affect the development of core disking. For the application to overcoring stress measurements, this is of less concern as measurements are taken in fracture-free rock. Hence, future tests should also be made in the best rock conditions available. Furthermore, the practical arrangements, and in particular the drilling equipment, must be improved upon. This is necessary to achieve reliable results and also to be able to drill more test holes and conduct more measurements (to study potential scatter). Detailed planning is imperative and additional numerical modeling, using both linear-elastic and plastic constitutive models should be carried out prior to the field work, and as an input into planning of hole locations.

8 Conclusions and recommendations

From the conducted work, the following conclusions and recommendations are presented:

- The objective of the work (to determine stress levels at which core disking occurs) was not fulfilled. The primary reasons for this were: (i) the lack of systematic core disking in the boreholes (only a few, separate, instance of disking observed), and
  (ii) the practical difficulties in drilling and overcoring, thus achieving only four core holes, and only one successful stress measurement.

- Overcoring measurements were conducted under difficult conditions. Subvertical open fractures intersected boreholes making measurements impossible and/or less reliable. Only one moderately reliable measurement results was obtained, indicating a maximum horizontal stress of around 14 MPa. This value is significantly lower than what was originally expected, and indicate either (i) a considerable destressing at the test site, or (ii) erroneous measurement results (influenced by difficulties in drilling, etc). The data does not permit discarding either of these hypotheses.

- The isolated observations of core disking and borehole breakouts indicated stresses lower than approximately 40 MPa judging from borehole breakouts, or lower than about 55 MPa (estimated based on lack of core disking). These values are an approximate upper bound of the maximum horizontal stress prior to drilling the holes, and for the majority of the rock mass volume at the test site.

- Locally, higher stresses probably exist, as evidenced by the observed core disking and the numerical stress modeling. The latter clearly showed that stress discontinuities developed over the steeply dipping fractures in the test volume.

- There is a strong link between observed core disking and the occurrence of subvertical fractures intersecting the boreholes. Slightly elevated stresses above and below a fracture coupled with (potentially) weaker rock near the fracture may be a contributing factor to the observed core disking.

- The numerical modeling showed much higher stresses than what can be inferred from field observations and measurements. A reason for this may be that the model does not replicate the full stress-path history of the test site, and its effect on the rock. It is believed that to do so, a model which captures permanent effects of reaching the rock strength must be used, i.e., a plasticity model, and that all stages in the excavation-loading be modeled. Even so, it may not be possible to describe all rock observations using a single numerical model.

- In summary, the lack of systematic core disking can be ascribed to two major factors: (i) lower stresses than expected in the test volume, and (ii) heterogeneous geology. The destressing of the test volume may be a result of the complex excavation and loading history of the APSE test area. The heterogeneous geology, and in particular the presence of subvertical fractures, influence the stress distribution making it more discontinuous. Together, these two factors may cause lower, and more varying, stresses in the test area, than originally anticipated. However, the governing mechanisms cannot be fully explained given the currently available data.

- The work did not result in any definite conclusions regarding the applicability of methods for estimating stresses from core disking observations. Since stress conditions are not known, it cannot be stated whether, e.g., the nomograms of /Hakala, 1999a/ provide realistic results or not. A particular problem is that the mechanisms for core disking still remain partly unresolved, in particular in cases with complex geology and structural conditions.

- The general idea of studying core disking in a field test still has potential. However, it is crucial that as many as possible of the factors controlling core disking are maintained constant. This means homogeneous geology with as few fractures as possible, well-defined stress conditions and simple stress-path history, better drilling control, and the ability to drill more tests holes and conduct more measurements (to achieve redundancy in the results). Detailed planning is essential and detailed numerical modeling, using both linear-elastic and plastic constitutive models should be carried out prior to the field work, and as an input into planning of hole locations.

9 References

Amadei B, Stephansson O, 1997. Rock stress and its measurement. London: Chapman & Hall, 490 pp.

Andersson J C, 2004. Äspö Pillar Stability Experiment. Summary of preparatory work and predictive modelling. *SKB, R-03-02. Svensk Kärnbränslehantering AB.*

Andersson, C. 2007. Äspö Pillar Stability Experiment, Final report. Rock mass response to coupled mechanical thermal loading. *SKB*, T*R-07-01. Svensk Kärnbränslehantering AB.*

Christiansson R, Jansson T, 2003. A test of different stress measurement methods in two orthogonal bore holes in the Äspö Hard Rock Laboratory (HRL), Sweden. *Int. J. Rock Mech. Min. Sci., 40*, No. 7-8, pp. 1161-1172.

Fardin N, 2003. The Effect of Scale on the Morphology, Mechanics and Transmissivity of Single Rock Fractures. Ph.D. Thesis, Kungliga Tekniska Högskolan, Stockholm, Sweden, 2003.

Fredriksson A, Staub I and Outers N, 2004. Äspö Pillar Stability Experiment. Final 2D coupled thermo-mechanical modelling. *SKB*, *R-04-02. Svensk Kärnbränslehantering AB.*

Fälth B, Kristensson O and Hökmark H, 2005. Äspö Hard Rock Laboratory. Äspö Pillar Stability Experiment. Thermo-mechanical 3D back analyze of the heating phase. *SKB, IPR-05-19. Svensk Kärnbränslehantering AB.*

Hakala M. 1999a. Numerical study on core damage and interpretation of in situ state of stress. Posiva report 99-25.

Hakala M. 1999b. Numerical study of the core disk fracturing and interpretation of the in situ state of stress. Proc. Ninth International Congress on Rock Mechanics (Paris, 1999), Vol. 2, pp. 1149-1153. Rotterdam: A. A. Balkema.

Hakala M. 2006. Quality control for overcoring stress measurement data. Posiva Report 2006-03.

Hakala M, Hudson J A, Christiansson R, 2003. Quality control of overcoring stress measurement data. *Int. J. Rock Mech. Min. Sci., 40*, No. 7-8, pp. 1141-1159.

Itasca Consulting Group, Inc., 2003. *3DEC – 3 Dimensional Distinct Element Code, User's Manual*. Minneapolis: Itasca.

Jacobsson L and Flansbjer M, 2005. Äspö Hard Rock Laboratory. Äspö Pillar Stability Experiment. Samples from TASQ tunnel at Äspö HRL. Normal loading and shear tests on joints. *SKB, IPR-05-23. Svensk Kärnbränslehantering AB.*

Jansson T, Stigsson M, 2002. Test with different stress measurement methods in two orthogonal bore holes in Äspö HRL. SKB R-report R-02-26. *Sv*ensk Kärnbränslehantering AB.

Kisiel, T, 2004. Personal communication.

KTH, 1990. Formelsamling i hållfasthetslära. Publikation nr 104, Institutionen för hållfasthetslära, Kungliga Tekniska Högskolan, Stockholm (in Swedish).

Leeman E R, 1968. The determination of the complete state of stress in rock using a single borehole—laboratory and underground measurements. *Int. J. Rock Mech. & Min. Sci., 5,* 31-56.

Leeman E R, Hayes D I, 1966. A technique for determining the complete state of stress in rock using a single borehole. In *Proceedings of the 1st International Congress on Rock Mechanics (Lisboa, 1966), Vol. 2,* pp. 17-24.

Lim S S, Martin C D, Christiansson R. 2006. Estimating in-situ stress magnitudes from core disking. *Proceedings International Symposium on In-Situ Rock Stress (Trondheim, June 19–21, 2006),* pp. 399-407. London: Taylor & Francis

Lindfors U, Perman F, Sjöberg J. 2005. Evaluation of the overcoring results from borehole KFM01B. SKB P-report P-05-66. Svensk Kärnbränslehantering AB.

Mas Ivars D, 2005. Äspö Hard Rock Laboratory. Äspö Pillar Stability Experiment. Hydromechanical data acquisition experiment at the APSE site. *SKB, IPR-05-21, Svensk Kärnbränslehantering AB.*

Mas Ivars D, 2006. Äspö Hard Rock Laboratory. Äspö Pillar Stability Experiment. Three-dimensional mechanical discontinuum modeling of de-stressing slot drilling at the APSE site. *SKB, IPR-report , Svensk Kärnbränslehantering AB* (in press).

Olofsson I, Simeonov A, Stephens M, Follin S, Nilsson A-C, Röshoff K, Lindberg U, Lanaro F, Fredriksson A, and Persson L, 2007. Site description modelling Forsmark, stage 2.2. A fracture domain concept as a basis for the statistical modelling of fractures and minor deformation zones, and interdisciplinary coordination. *SKB, R-07-15. Svensk Kärnbränslehantering AB.*

Rinne M, Shen B and Lee H-S, 2004. Äspö Pillar Stability Experiment. Modelling of fracture development of APSE by FRACOD. *SKB, R-04-04. Svensk Kärnbränslehantering AB*

Sjöberg J. 2002. 3D overcoring rock stress measurements in borehole KA3376B01 at Äspö HRL. SKB International Progress Report IPR-03-16. Stockholm: Swedish Nuclear Fuel and Waste Management Co, 12 p..

Sjöberg J, Klasson H, 2003. Stress measurements in deep boreholes using the *Borre* (*SSPB*) probe. *Int. J. Rock Mech. Min. Sci., 40,* No. 7-8, pp. 1205-1233.

SKB, 2006. Preliminary site description Laxemar stage 2.1. Feedback for the completion of the site investigation including input from safety assessment and repository engineering. *SKB, R-06-110. Svensk Kärnbränslehantering AB.*

Staub I, Andersson J C and Magnor B, 2004. Äspö Pillar Stability Experiment. Geology and mechanical properties of the rock in TASQ. *SKB, R-04-01. Svensk Kärnbränslehantering AB.*

Staub I, Janson T and Fredriksson A, 2003. Äspö Hard Rock Laboratory. Äspö Pillar Stability Experiment. Geology and properties of the rock mass around the experiment volume. *SKB, IPR-03-02. Svensk Kärnbränslehantering AB.*

Wanne T, Johansson E and Potyondy D, 2004. Äspö Pillar Stability Experiment. Final coupled 3d thermo-mechanical modelling. Preliminary particle-mechanical modelling. *SKB, R-04-03. Svensk Kärnbränslehantering AB.*

Appendix A

Core logging data

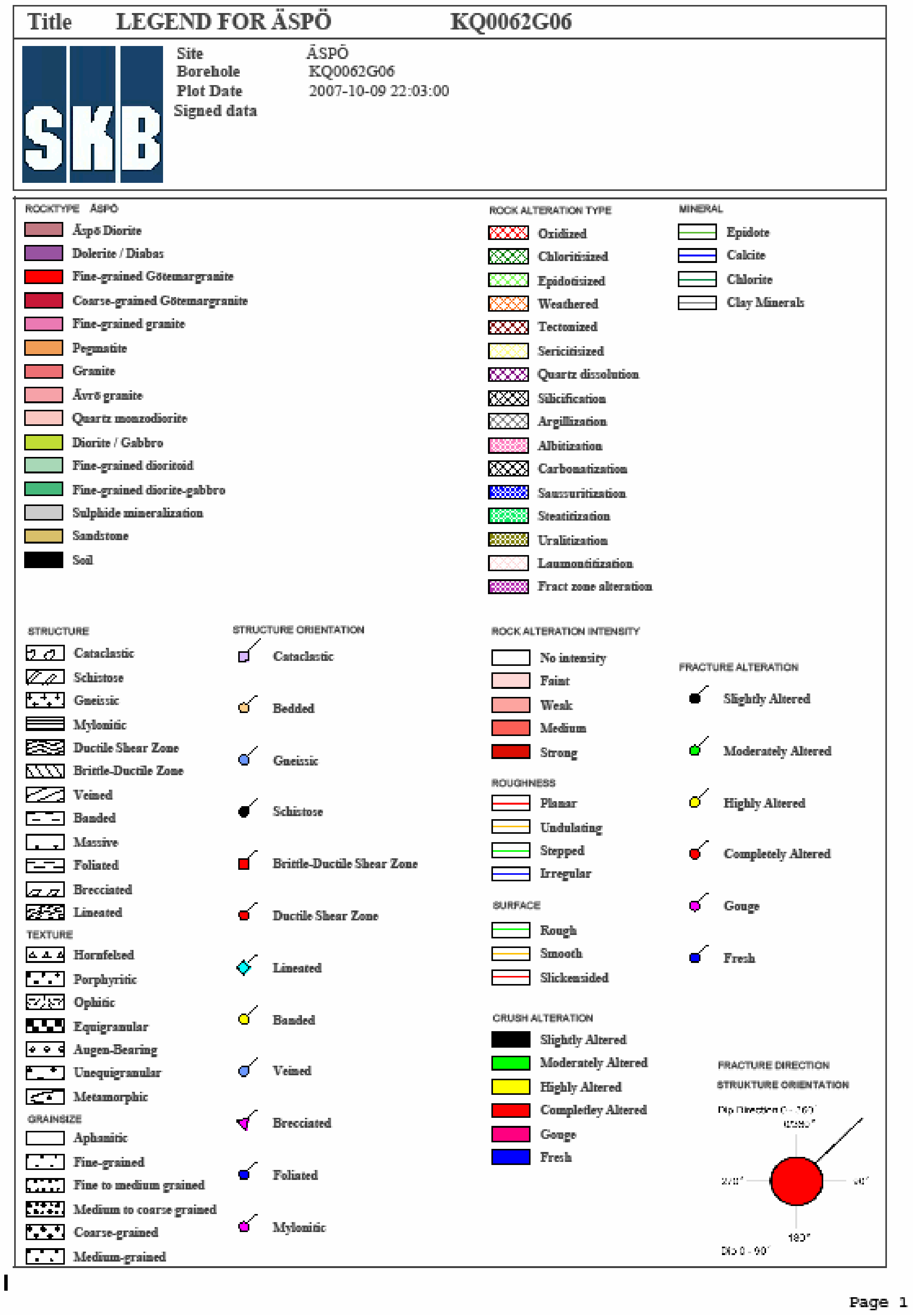

Title LEGEND FOR ÄSPÖ KQ0062G06

Site ÄSPÖ
Borehole KQ0062G06
Plot Date 2007-10-09 22:03:00
Signed data

ROCKTYPE ÄSPÖ
- Äspö Diorite
- Dolerite / Diabas
- Fine-grained Götemargranite
- Coarse-grained Götemargranite
- Fine-grained granite
- Pegmatite
- Granite
- Ävrö granite
- Quartz monzodiorite
- Diorite / Gabbro
- Fine-grained dioritoid
- Fine-grained diorite-gabbro
- Sulphide mineralization
- Sandstone
- Soil

ROCK ALTERATION TYPE
- Oxidized
- Chloritisized
- Epidotisized
- Weathered
- Tectonized
- Sericitisized
- Quartz dissolution
- Silicification
- Argillization
- Albitization
- Carbonatization
- Saussuritization
- Steatitization
- Uralitization
- Laumontitization
- Fract zone alteration

MINERAL
- Epidote
- Calcite
- Chlorite
- Clay Minerals

STRUCTURE
- Cataclastic
- Schistose
- Gneissic
- Mylonitic
- Ductile Shear Zone
- Brittle-Ductile Zone
- Veined
- Banded
- Massive
- Foliated
- Brecciated
- Lineated

TEXTURE
- Hornfelsed
- Porphyritic
- Ophitic
- Equigranular
- Augen-Bearing
- Unequigranular
- Metamorphic

GRAINSIZE
- Aphanitic
- Fine-grained
- Fine to medium grained
- Medium to coarse grained
- Coarse-grained
- Medium-grained

STRUCTURE ORIENTATION
- Cataclastic
- Bedded
- Gneissic
- Schistose
- Brittle-Ductile Shear Zone
- Ductile Shear Zone
- Lineated
- Banded
- Veined
- Brecciated
- Foliated
- Mylonitic

ROCK ALTERATION INTENSITY
- No intensity
- Faint
- Weak
- Medium
- Strong

ROUGHNESS
- Planar
- Undulating
- Stepped
- Irregular

SURFACE
- Rough
- Smooth
- Slickensided

CRUSH ALTERATION
- Slightly Altered
- Moderately Altered
- Highly Altered
- Completley Altered
- Gouge
- Fresh

FRACTURE ALTERATION
- Slightly Altered
- Moderately Altered
- Highly Altered
- Completely Altered
- Gouge
- Fresh

FRACTURE DIRECTION
STRUKTURE ORIENTATION

Page 1

Title GEOLOGY IN KQ0061G10 **Appendix:**

Site	ÄSPÖ	**Coordinate System**	RT90-RHB70
Borehole	KQ0061G10	**Northing [m]**	6367850.40
Diameter [mm]	76	**Easting [m]**	1551408.83
Length [m]	5.720	**Elevation [m.a.s.l.]**	-446.09
Bearing [°]	290.44	**Drilling Start Date**	2006-02-02 13:55:00
Inclination [°]	-89.73	**Drilling Stop Date**	2006-02-08 09:20:00
Date of coremapping	2006-04-19 14:22:00	**Plot Date**	2007-10-22 22:03:28
Rocktype data from	p_rock	**Signed data**	

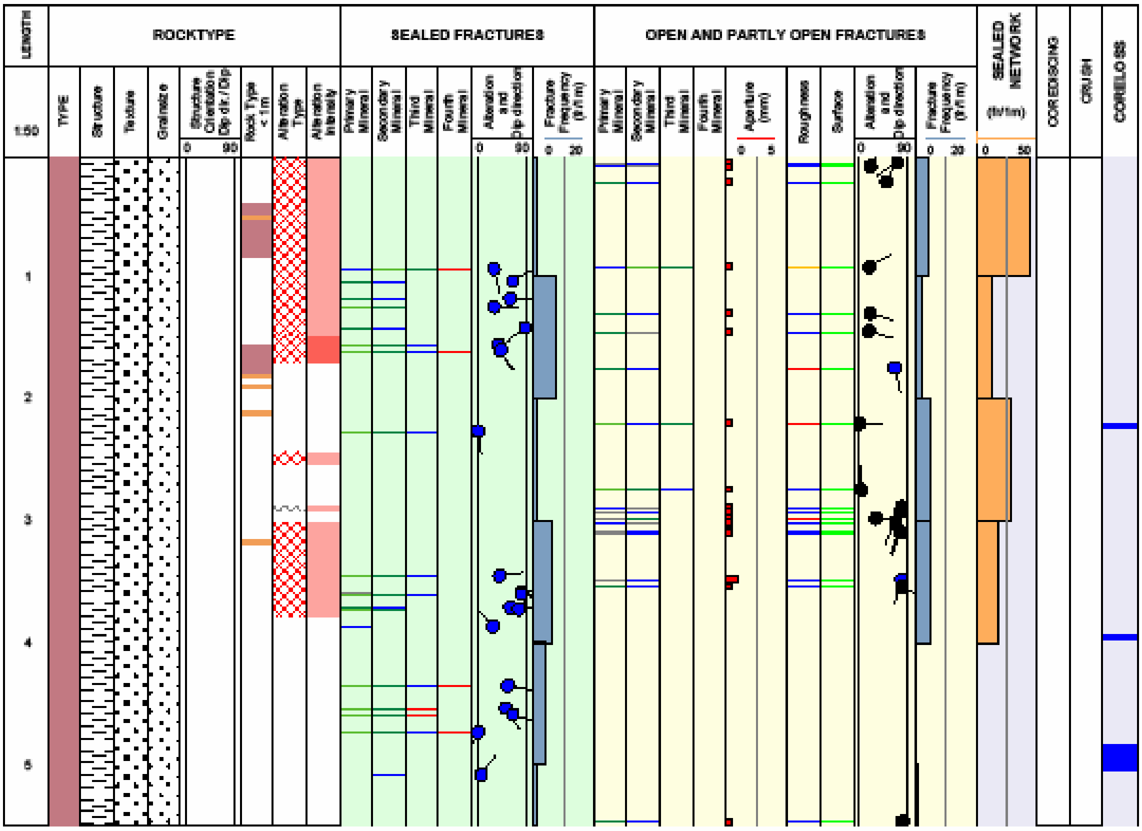

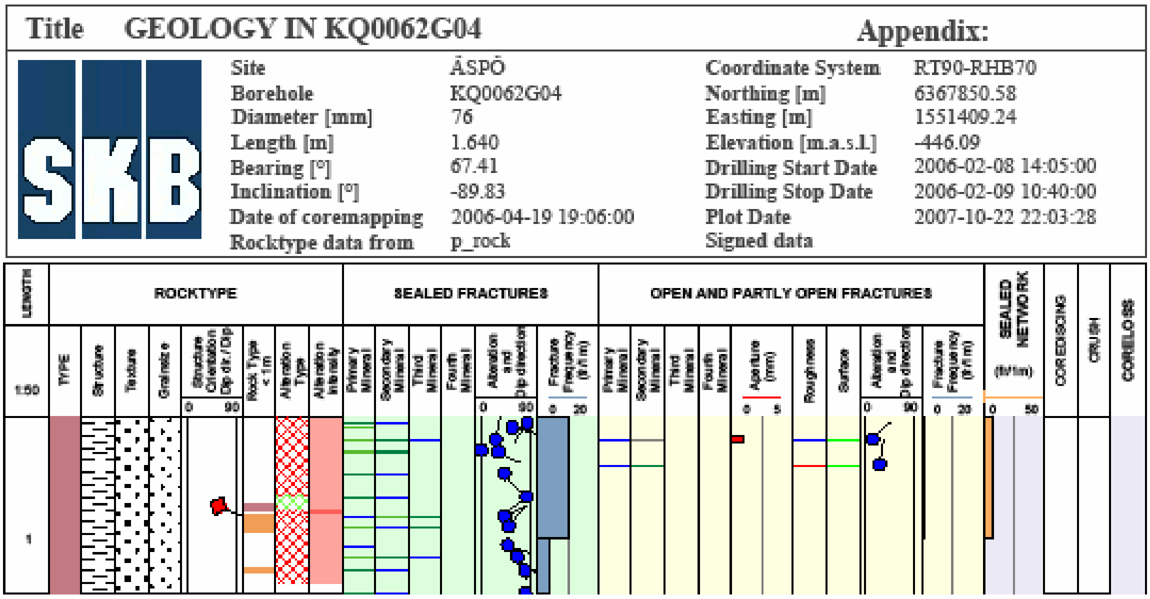

Title GEOLOGY IN KQ0062G04 **Appendix:**

Site	ÄSPÖ	**Coordinate System**	RT90-RHB70
Borehole	KQ0062G04	**Northing [m]**	6367850.58
Diameter [mm]	76	**Easting [m]**	1551409.24
Length [m]	1.640	**Elevation [m.a.s.l.]**	-446.09
Bearing [°]	67.41	**Drilling Start Date**	2006-02-08 14:05:00
Inclination [°]	-89.83	**Drilling Stop Date**	2006-02-09 10:40:00
Date of coremapping	2006-04-19 19:06:00	**Plot Date**	2007-10-22 22:03:28
Rocktype data from	p_rock	**Signed data**	

Title GEOLOGY IN KQ0062G05 **Appendix:**

Site	ÄSPÖ	**Coordinate System**	RT90-RHB70
Borehole	KQ0062G05	**Northing [m]**	6367850.85
Diameter [mm]	36	**Easting [m]**	1551409.14
Length [m]	5.640	**Elevation [m.a.s.l.]**	-446.12
Bearing [°]	9.45	**Drilling Start Date**	2006-01-17 14:00:00
Inclination [°]	-89.26	**Drilling Stop Date**	2006-01-24 14:10:00
Date of coremapping	2006-04-20 08:14:00	**Plot Date**	2007-10-22 22:03:28
Rocktype data from	p_rock	**Signed data**	

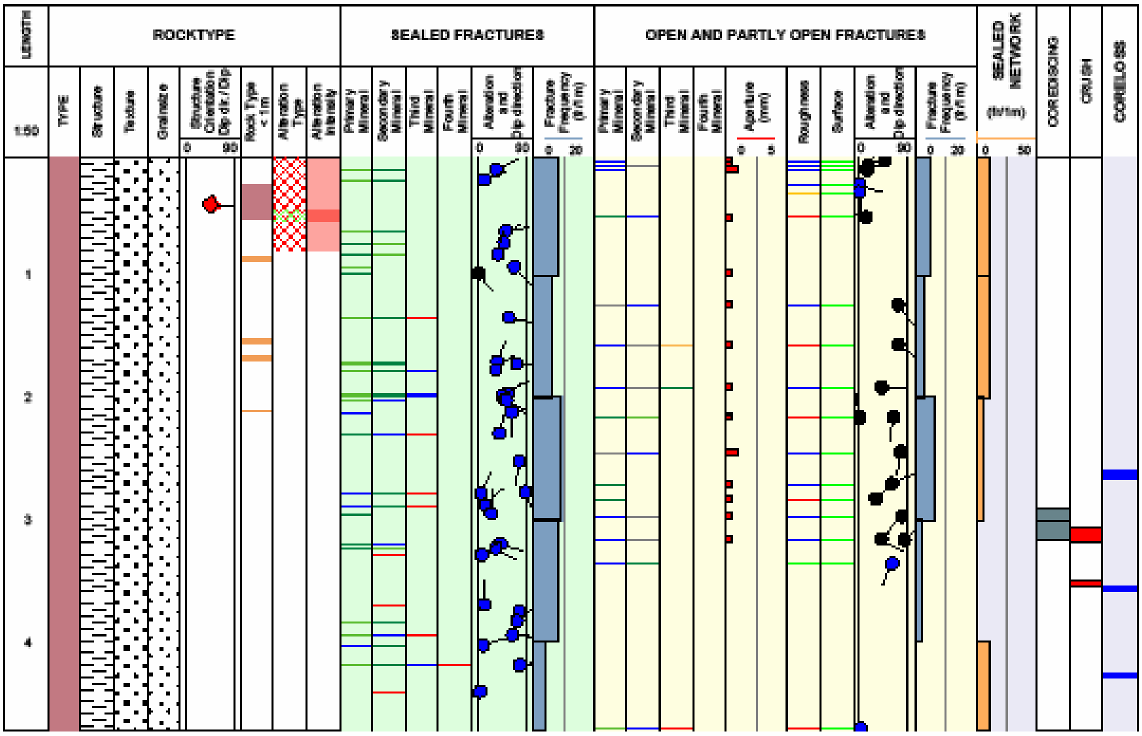

Title GEOLOGY IN KQ0062G06 **Appendix:**

Site	ÄSPÖ	**Coordinate System**	RT90-RHB70
Borehole	KQ0062G06	**Northing [m]**	6367851.08
Diameter [mm]	76	**Easting [m]**	1551408.99
Length [m]	7.500	**Elevation [m.a.s.l.]**	-446.22
Bearing [°]	308.94	**Drilling Start Date**	2006-01-25 12:00:00
Inclination [°]	-89.66	**Drilling Stop Date**	2006-02-02 12:03:00
Date of coremapping	2006-04-18 10:44:00	**Plot Date**	2007-10-22 22:03:28
Rocktype data from	p_rock	**Signed data**	

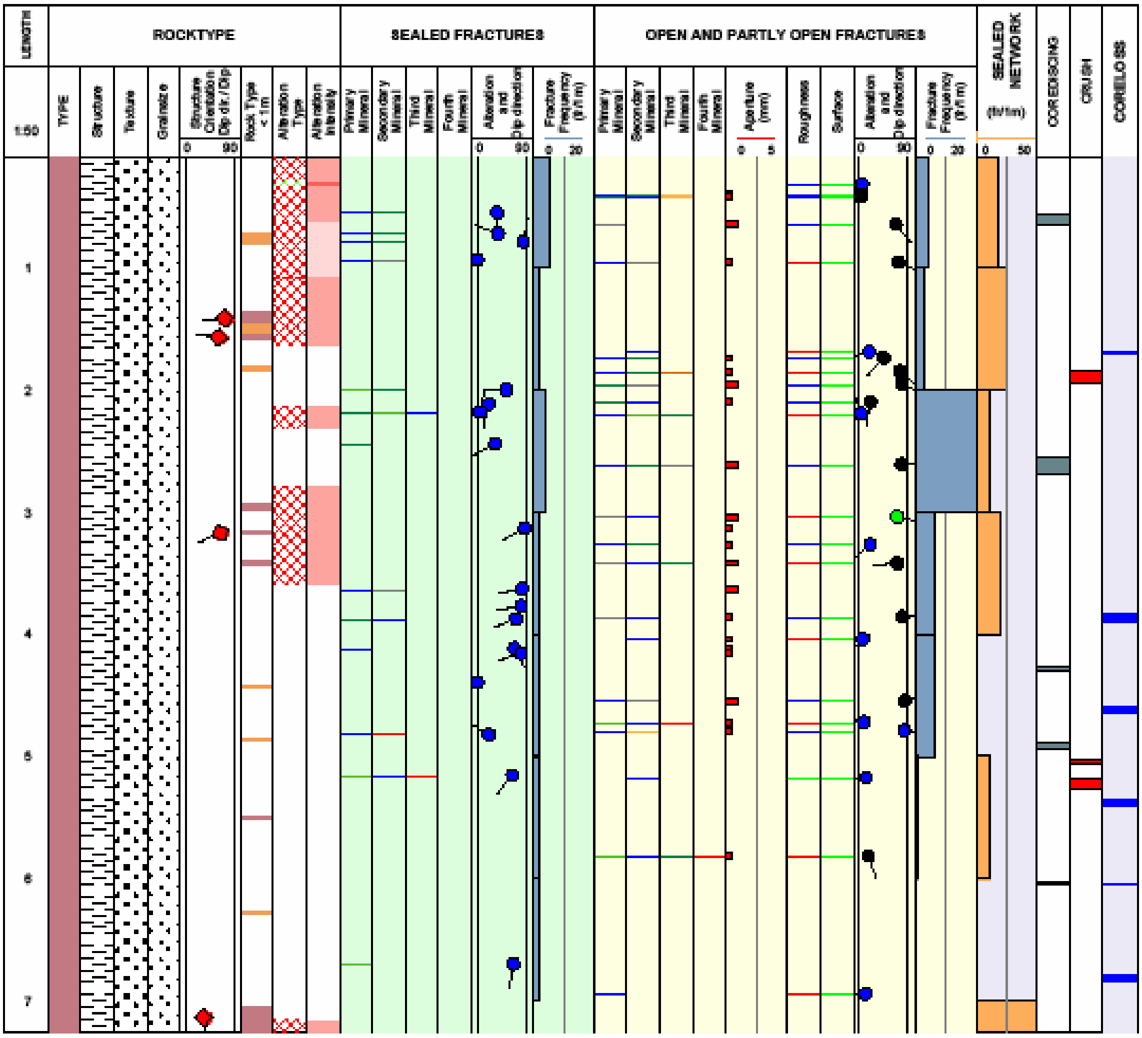

Appendix B

RVS model

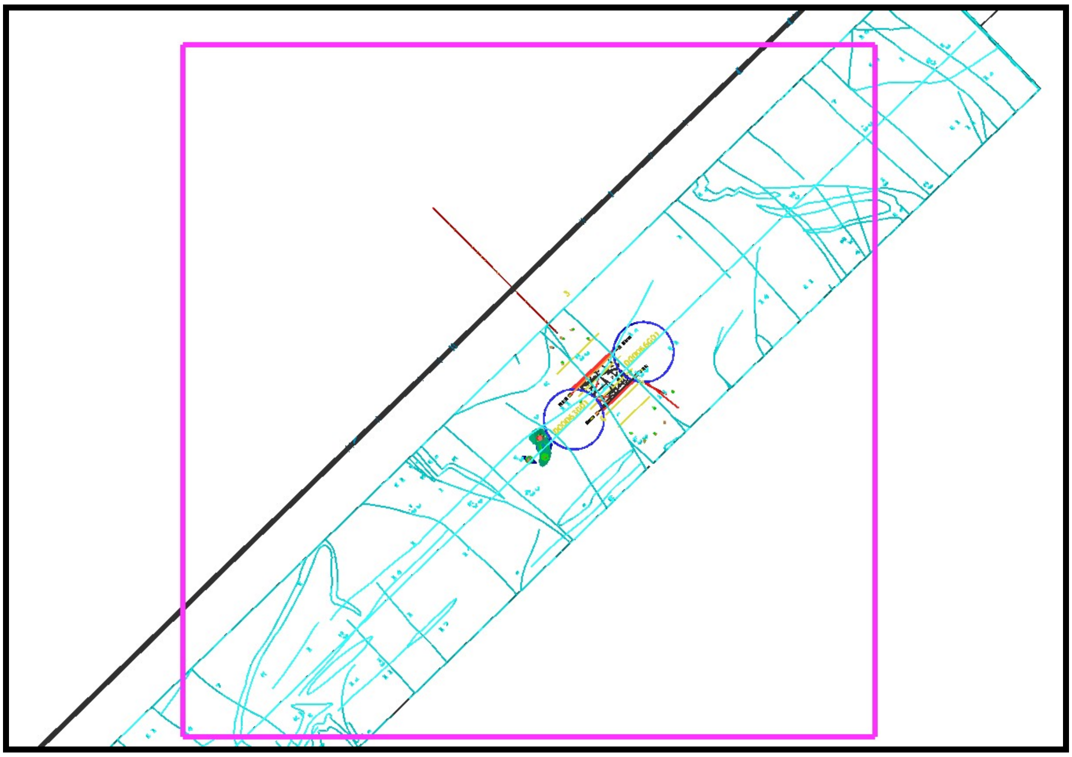

Figure B-1. *Top view over the model volume (purple square), where north (Äspö96) is up. The mapping of the TASQ-tunnel is seen as light blue lines, representing mapped structures in the tunnel roof and the two deposition holes are seen as darker blue circles. Also seen in various colors are boreholes in the area and visualized parameters in these. The core-disking test site is situated just to the southwest of the deposition holes.*

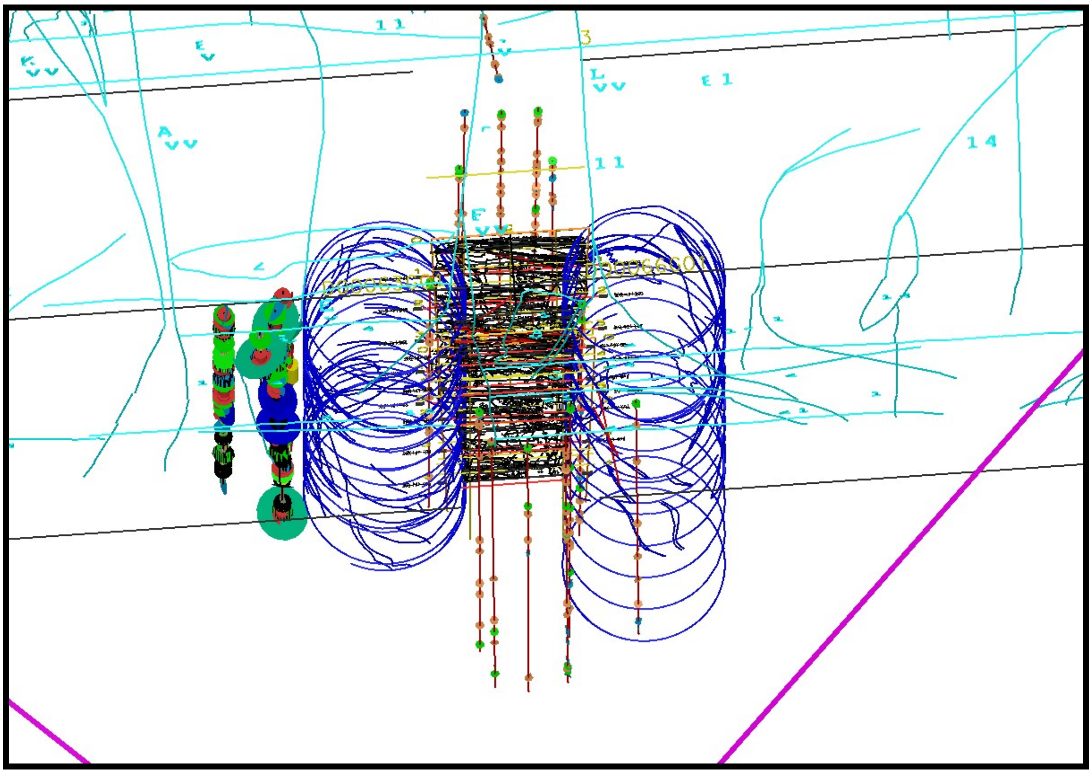

Figure B-2. *A close-up view over the deposition holes area and the core-disking test holes to the left. The view is down towards the northwest.*

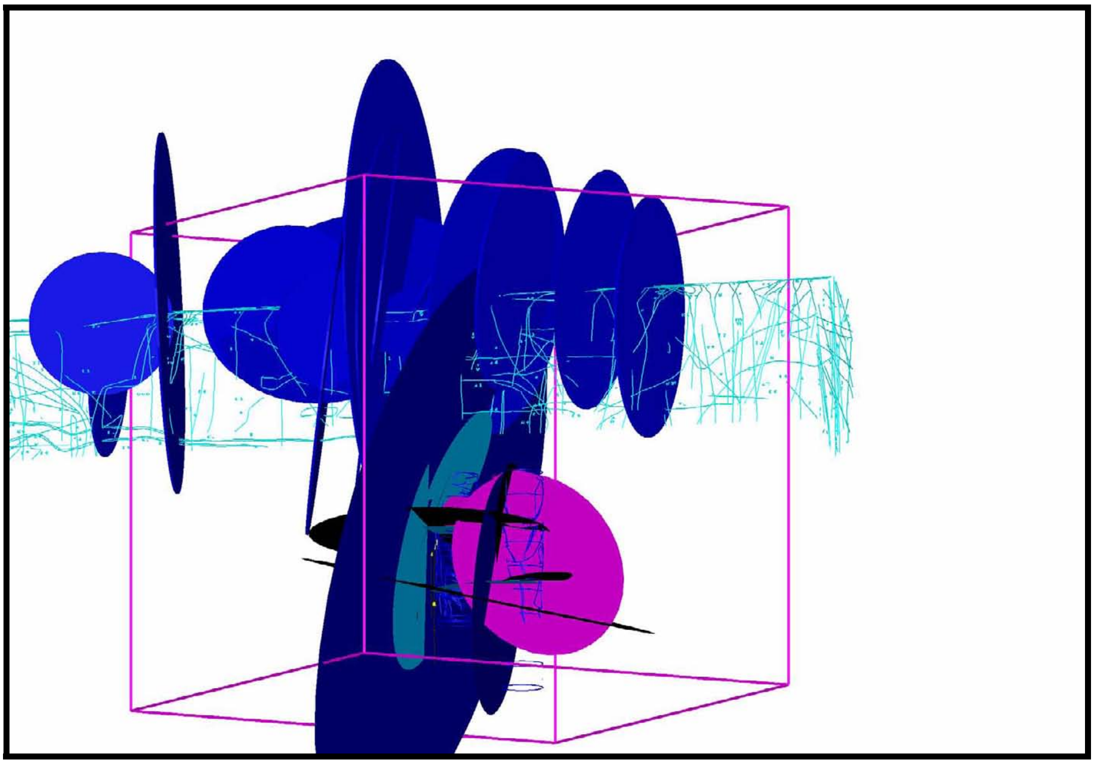

Figure B-3. *Visualized "fracture observations" in the model volume. See also table A1 for tabulated fracture observations.*

Table B-1. Fracure observations in RVS.

Visualization name	Object	Comment
TASQ-Z0	Fracture zone	Brittle-ductile deformation zone inherited from earlier model
TASQ-Z0-small	Fracture zone	Smaller version of the same zone as above
MTA_1_block	Mylonite	
MTA_2_block	Mylonite	
Z0_DQ63G01_centerline	Fracture zone	Brittle-ductile deformation zone in DQ0063. Purple in Figure B-3
Z0(U)_DQ66G01	Fracture zone	Brittle-ductile deformation zone in DQ0066, upper splay. Purple in Figure B-3
Z0(L)_DQ66G01	Fracture zone	Brittle-ductile deformation zone in DQ0066, lower splay. Purple in Figure B-3
MTA_3_block	Mylonite	
MTB_1_block	Mylonite	
MTA_4_block	Mylonite	
MTA_5_block	Mylonite	
Z0	Fracture zone	
Z0_low_cont	Fracture zone	
frac_n45roof_1	Water-bearing fracture	Dark blue in Figure B-3
NS_fracture_1_V	Water-bearing fracture	Dark blue in Figure B-3

NW_fracture1_VV	Water-bearing fracture	Dark blue in Figure B-3
NW_fracture2_VV	Water-bearing fracture	Dark blue in Figure B-3
NW_fracture3_VV	Water-bearing fracture	Dark blue in Figure B-3
NW_fracture4_VV	Water-bearing fracture	Dark blue in Figure B-3
NW_fracture5_VV	Water-bearing fracture	Dark blue in Figure B-3
NW_fracture6_VV	Water-bearing fracture	Dark blue in Figure B-3
NW_fracture7_VV	Water-bearing fracture	Dark blue in Figure B-3
NW_fracture7_V	Water-bearing fracture	Dark blue in Figure B-3
NW_fracture8_VV	Water-bearing fracture	Dark blue in Figure B-3
NW_fracture9_VV	Water-bearing fracture	Dark blue in Figure B-3
NW_fracture10_V	Water-bearing fracture	Dark blue in Figure B-3
NO_fracture1_V	Water-bearing fracture	Dark blue in Figure B-3
NO_fracture2_V	Water-bearing fracture	Dark blue in Figure B-3
NO_fracture3_V	Water-bearing fracture	Dark blue in Figure B-3
NO_fracture4_V	Water-bearing fracture	Dark blue in Figure B-3
subh_fracture1	Large sub-horizontal fracture	Light blue in Figure B-3
subh_fracture2	Large sub-horizontal fracture	Light blue in Figure B-3
subh_fracture3	Large sub-horizontal fracture	Light blue in Figure B-3
NW_fracture1_corediscing hole	Water-bearing fracture	Close to core-disking boreholes. Light blue in Figure B-3
NW_fracture5_deposition hole	Water-bearing fracture	Close to core-disking boreholes. Light blue in Figure B-3
NW_fracture4_deposition holes	Water-bearing fracture	Close to core-disking boreholes. Light blue in Figure B-3
NW_fracture2_corediscing hole	Water-bearing fracture	Close to core-disking boreholes. Light blue in Figure B-3
NW_fracture3_deposition holes	Water-bearing fracture	Close to core-disking boreholes. Light blue in Figure B-3
NW_fracture2_deposition holes	Water-bearing fracture	Close to core-disking boreholes. Light blue in Figure B-3
wbfr_dephole	Water-bearing fracture	
wbfr_dephole	Water-bearing fracture	

Table B-1 (continued). Fracure observations in RVS.

Visualization name	Object	Comment
wbfr_3	Water-bearing fracture	Black in Figure B-3
Fracture_124_block	Water-bearing fracture	
fracture_DQ66G01_ep	Sub-horizontal fracture	Black in Figure B-3
subh_fracture_epbreccia	Sub-horizontal fracture	Black in Figure B-3

Table B-2. Modeled objects.

Object name in RVS	Object	Comment
wbfr_DQ66G01	Water-bearing fracture	
APSE_NW_strukt_2	Earlier modelled fault fracture	Not used in model (not water-bearing)
wbfr_NS_TQ	Water-bearing fracture	
wbfr_TQ_NE	Water-bearing fracture	
wbfr_TQ_NW	Water-bearing fracture	
wbfr_TQ_NW	Water-bearing fracture	
wbfr_coredisc_DQ63_02	Water-bearing fracture	
Ep_frac_fault	Complex epidote fracture	
Ep_breccia	Complex epidote fracture	
APSE_SZ_S	Shear zone	Not used in model
APSE_SZ_W_N	Shear zone	Not used in model (poor fit)
APSE_SZ_W_S	Shear zone	
TASQ_Z0_upper zone	Shear zone	
Z0_DQ66G01_lower	Shear zone	
Z0_Q_NE_part_upper	Shear zone	Nott used in model (poor fit)
APSE_19sec45-60	Fault fracture	Inherited from earlier model

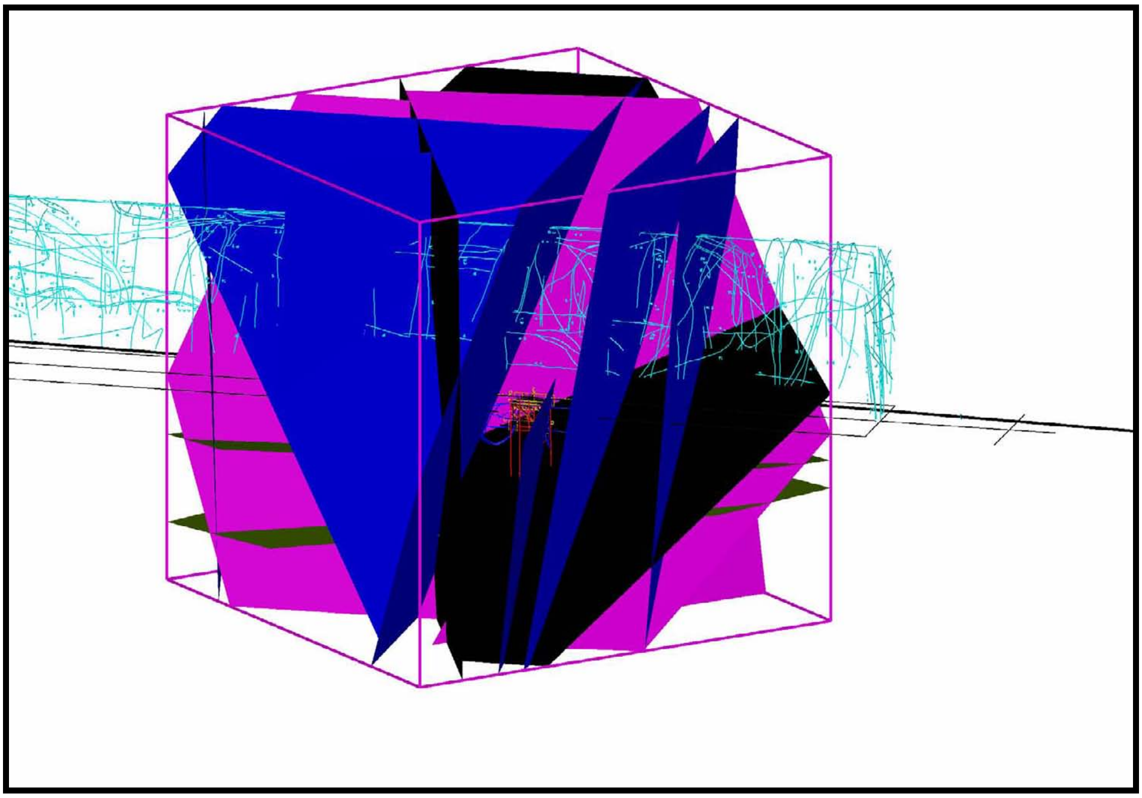

Figure B-4. *Modelled zones and fractures. See tables A-2 and A-3 for tabulation of modelled objects.*

Appendix C

Key stress measurement data

Table C1. Key measurement data for test no. KQ0061G10:1:2, 4.13 m borehole length (borehole B2).

Activity	Date [yy-mm-dd]	Time [hh:mm:ss]
Activation time	06-02-06	19:00:00
Mixing of glue	06-02-06	19:19:00
Application of glue to gauges	06-02-06	19:22:00
Probe installation in pilot hole	06-02-06	19:27:00
Start time for dense sampling (5 s interval)	06-02-07	07:00:00
Adapter retrieved	06-02-07	08:30:00
Adapter on surface	06-02-07	08:31:00
Drill string fed down the hole	06-02-07	08:45:00
Drill string in place	06-02-07	08:52:00
Flushing start	06-02-07	08:57:00
Rotation start	06-02-07	09:15:45
Overcoring start	06-02-07	09:16:00
Overcoring 4 cm	06-02-07	09:20:20
Overcoring 8 cm	06-02-07	09:25:30
Overcoring 12 cm	06-02-07	09:30:00
Overcoring 16 cm	06-02-07	09:33:30
Overcoring 20 cm	06-02-07	09:37:10
Overcoring 24 cm	06-02-07	09:40:30
Overcoring 28 cm	06-02-07	09:44:20
Overcoring 32 cm	06-02-07	09:48:10
Overcoring stop (70 cm)	06-02-07	10:09:30
Flushing off	06-02-07	10:55:55
Core break	06-02-07	11:12:30 11:36:30
Core retrieval start	06-02-07	11:37:00
Core & probe on surface	06-02-07	11:49:50
End of strain registration	06-02-07	12:27:15
Calculation of strain difference: OC Start	06-02-07	09:16:00
Calculation of strain difference: OC Stop	06-02-07	10:27:30

Overcoring advance	Overcoring rate [cm/min]
0 – 16 cm	0.9
16 – 32cm	1.1
32 cm – overcoring stop	1.8

Table C2. Key measurement data for test no. KQ0061G10:2:1, 5.18 m borehole length (borehole B2).

Activity	Date [yy-mm-dd]	Time [hh:mm:ss]
Activation time	06-02-07	19:45:00
Mixing of glue	06-02-07	20:04:00
Application of glue to gauges	06-02-07	20:07:00
Probe installation in pilot hole	06-02-07	20:16:00
Start time for dense sampling (5 s interval)	06-02-08	07:00:00
Adapter retrieved	06-02-08	08:06:30
Adapter on surface	06-02-08	08:07:00
Drill string fed down the hole	06-02-08	08:08:00
Drill string in place	06-02-08	08:12:00
Flushing start	06-02-08	08:16:00
Rotation start	06-02-08	08:39:40
Overcoring start	06-02-08	08:40:00
Overcoring 4 cm	06-02-08	08:43:50
Overcoring 8 cm	06-02-08	08:47:10
Overcoring 12 cm	06-02-08	08:50:50
Overcoring 16 cm	06-02-08	08:53:25
Overcoring 20 cm	06-02-08	08:56:15
Overcoring 24 cm	06-02-08	08:58:50
Overcoring 28 cm	06-02-08	09:01:45
Overcoring 32 cm	06-02-08	09:04:00
Overcoring stop (71 cm)	06-02-08	09:23:00
Flushing off	06-02-08	10:24:00
Core break	06-02-08	10:30:50
Core retrieval start	06-02-08	10:49:25
Core & probe on surface	06-02-08	11:00:00
End of strain registration	06-02-08	11:23:15
Calculation of strain difference: OC Start	06-02-08	08:40:30
Calculation of strain difference: OC Stop	06-02-08	10:07:00

Overcoring advance	Overcoring rate [cm/min]
0 – 16 cm	1.2
16 – 32 cm	1.5
32 cm – overcoring stop	2.3

Appendix D

Overcoring strain data and graphs

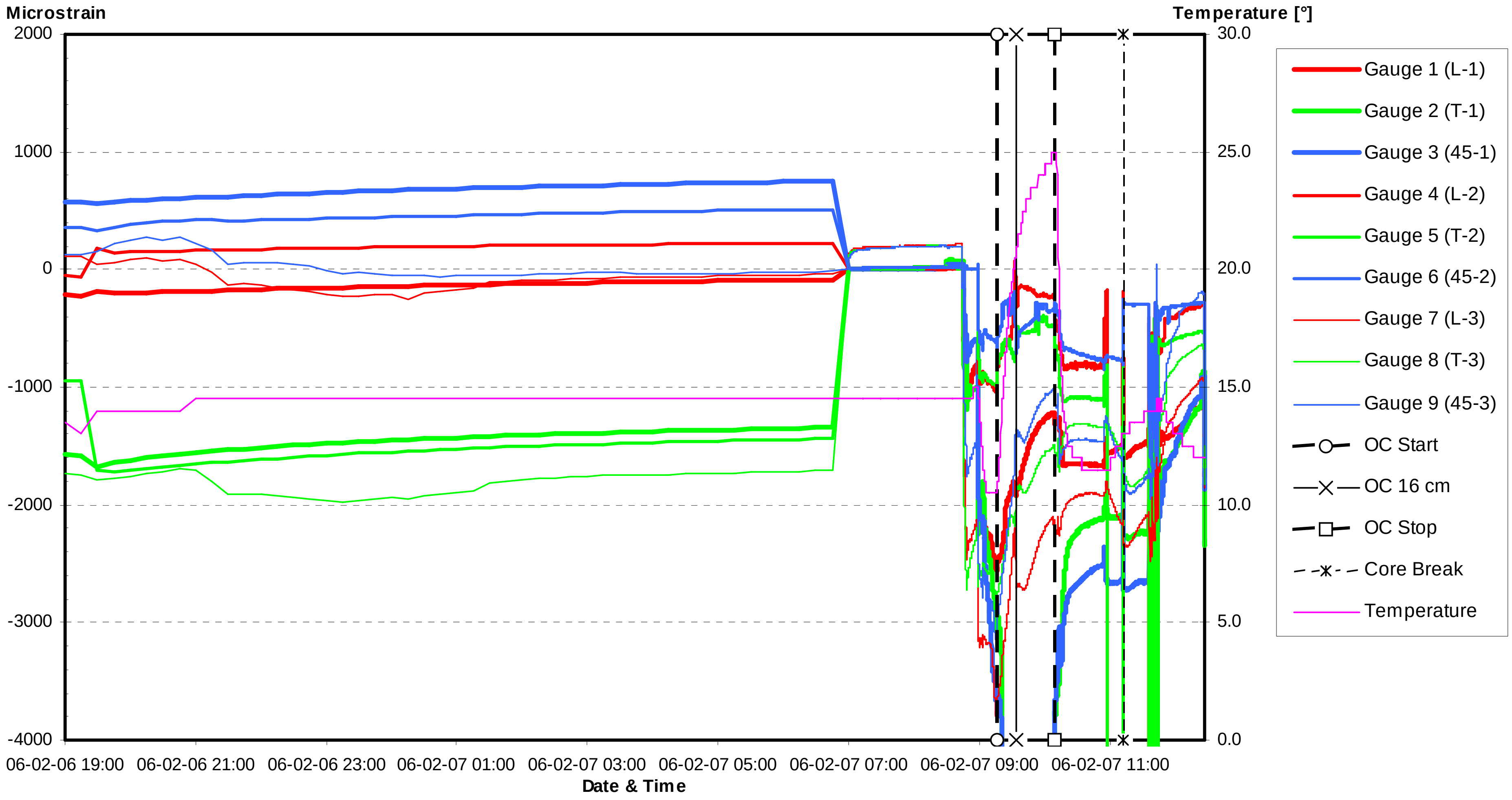

Figure D1. *All recorded strain data and temperature from activation of probe to recovery from borehole for test no. KQ0061G10:1:2, 4.13 m depth.*

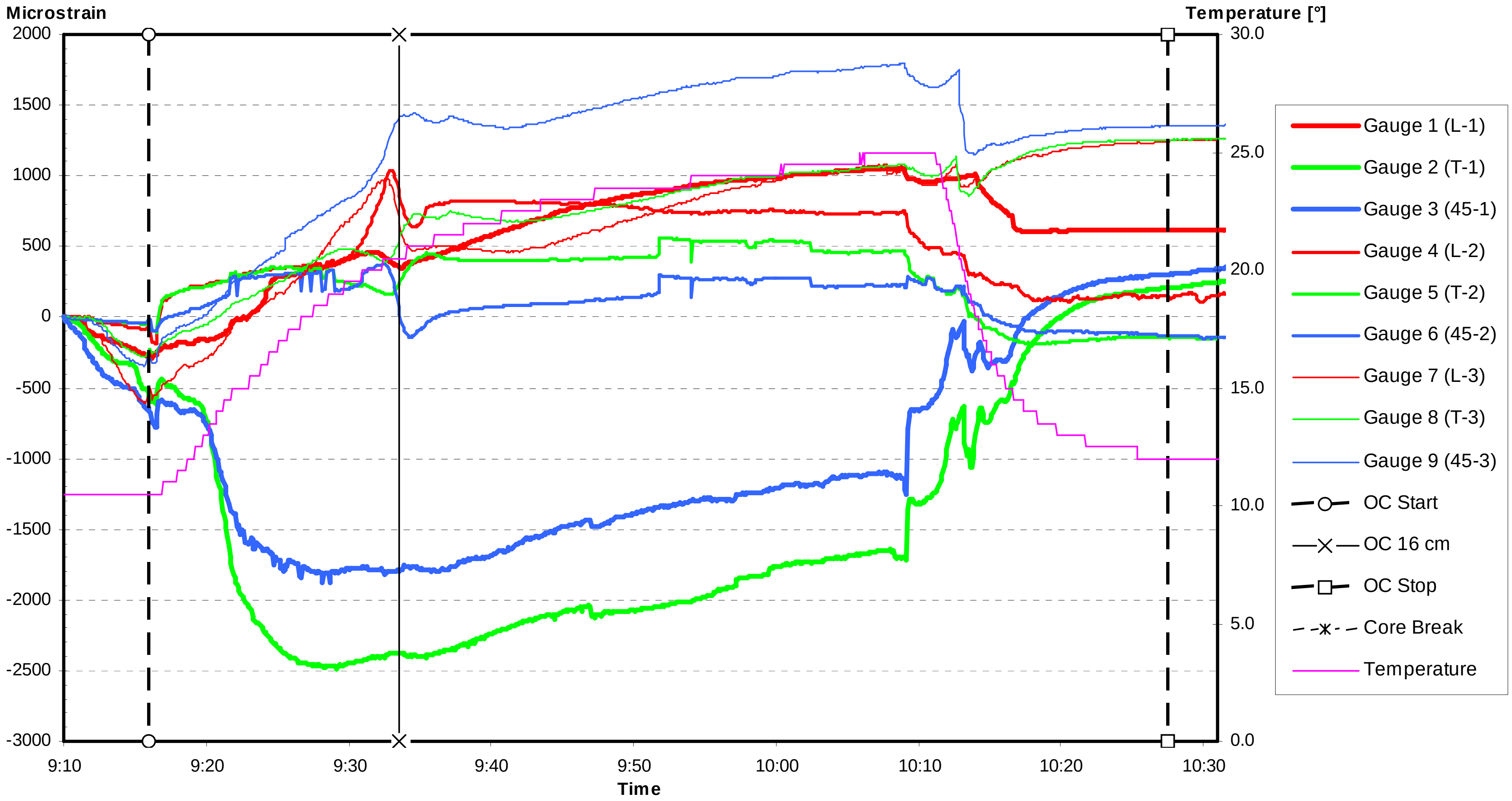

Figure D2. *Recorded strain data and temperature during overcoring (from start to stop) for test no. KQ0061G10:1:2, 4.13 m depth. Strain values reset to zero at 09:10.*

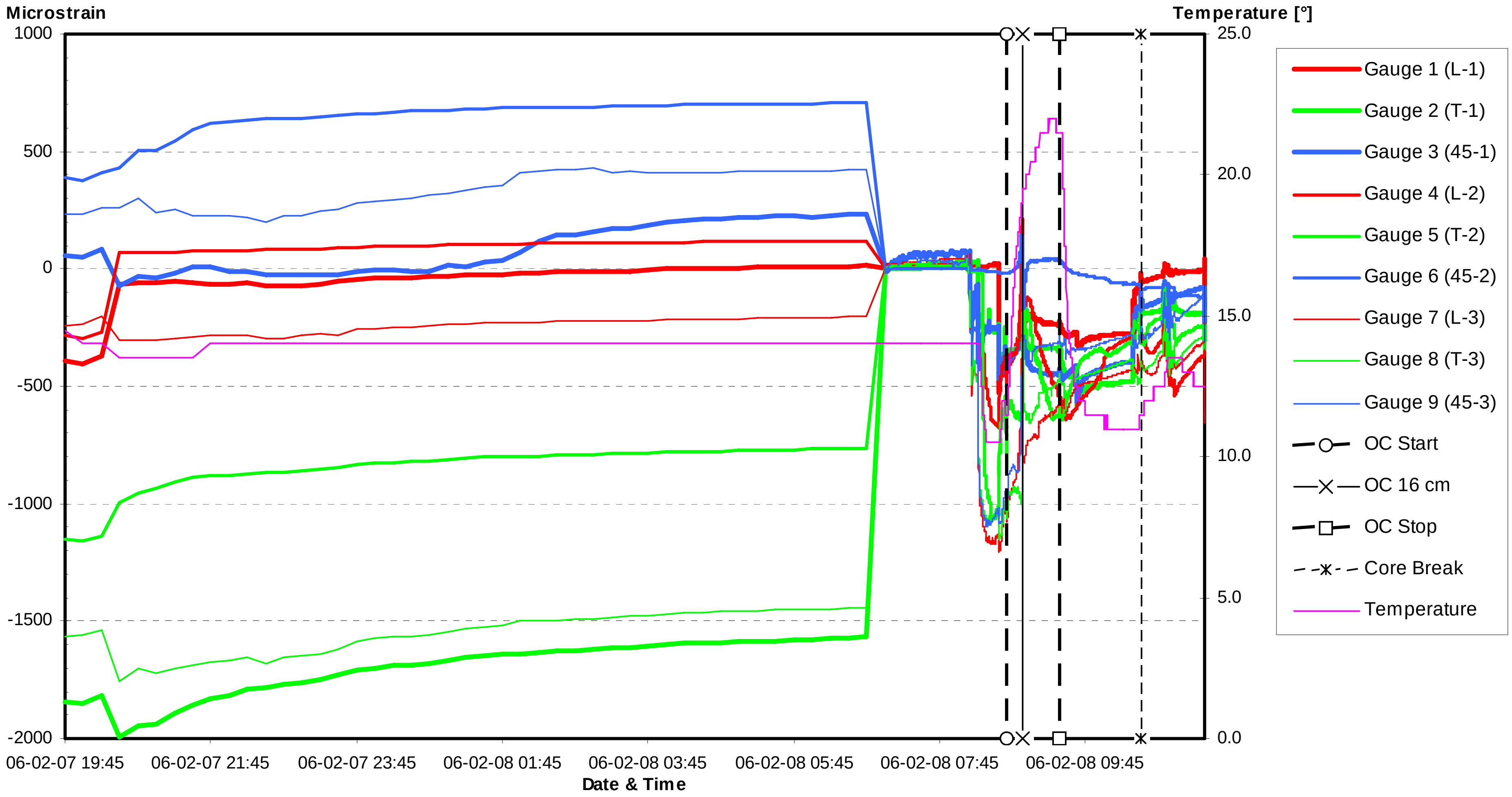

Figure D3. *All recorded strain data and temperature from activation of probe to recovery from borehole for test no. KQ0061G10:2:1, 5.18 m depth.*

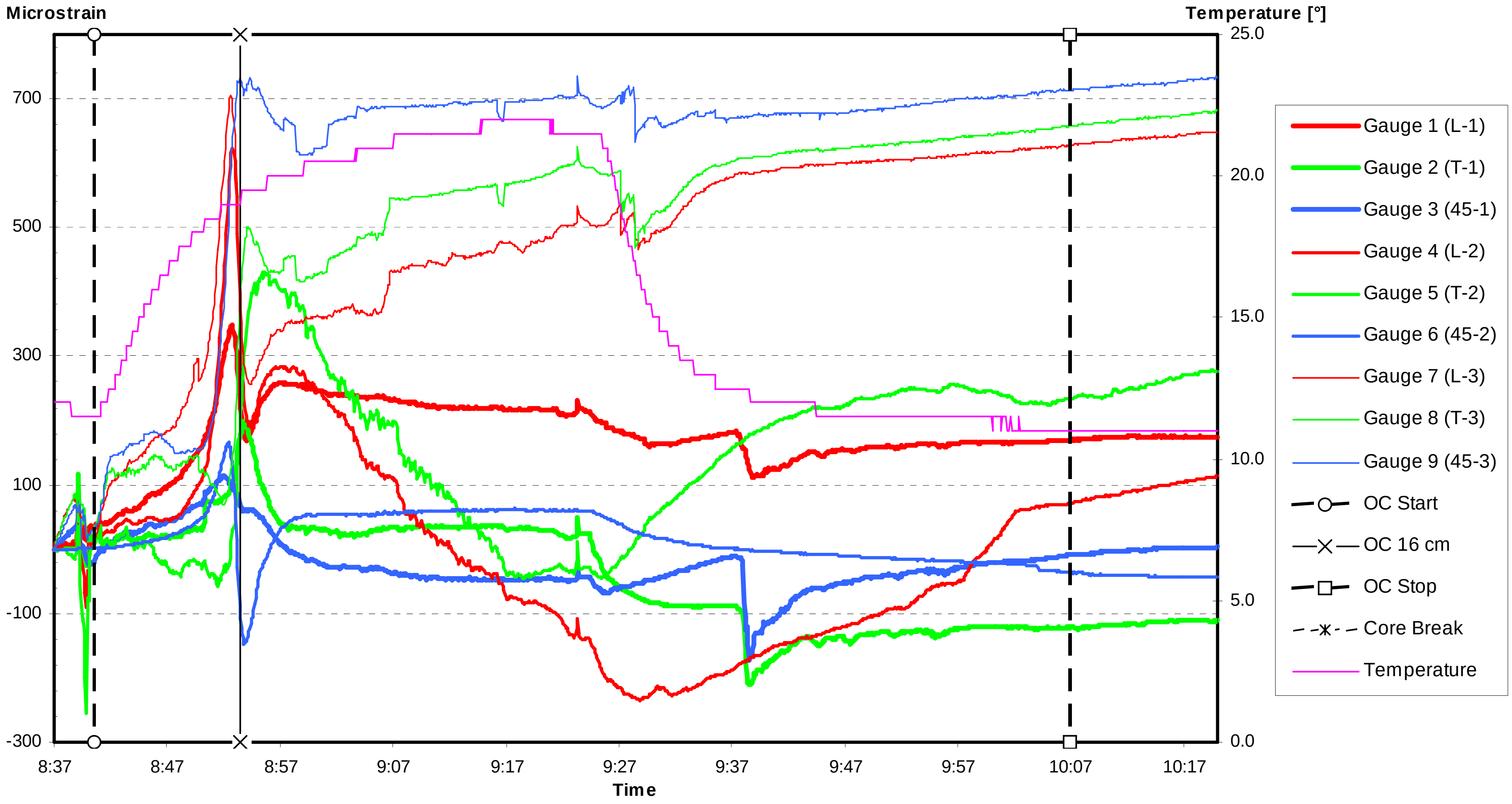

Figure D4. *Recorded strain data and temperature during overcoring (from start to stop) for test no. KQ0061G10:2:1, 5.18 m depth. Strain values reset to zero at 08:37.*

Appendix E

Biaxial test data

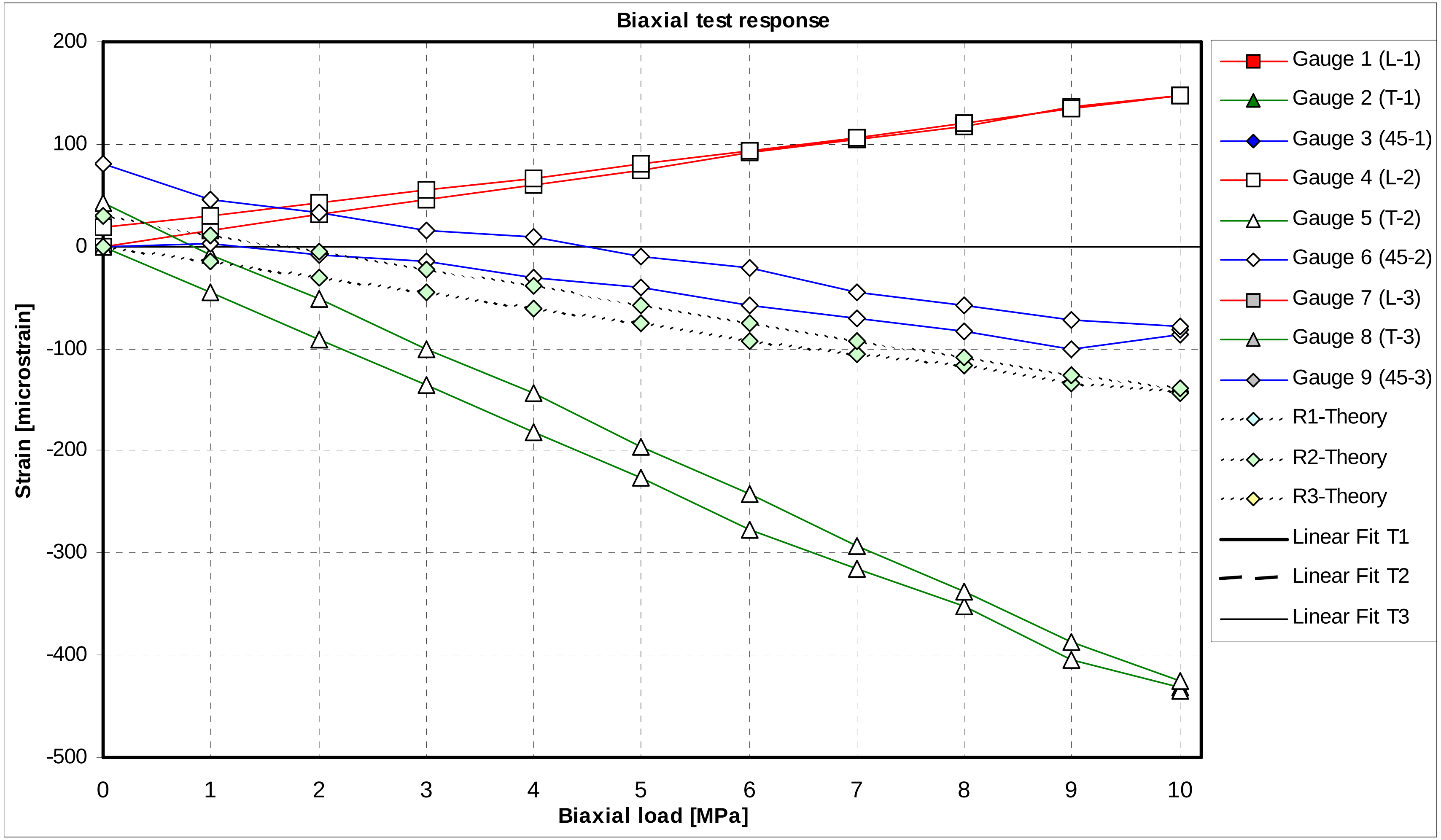

Figure E1. *Results from biaxial testing of test no. KQ0061G10:1:2, 4.13 m depth, excluding rosette nos. 1 and 3.*

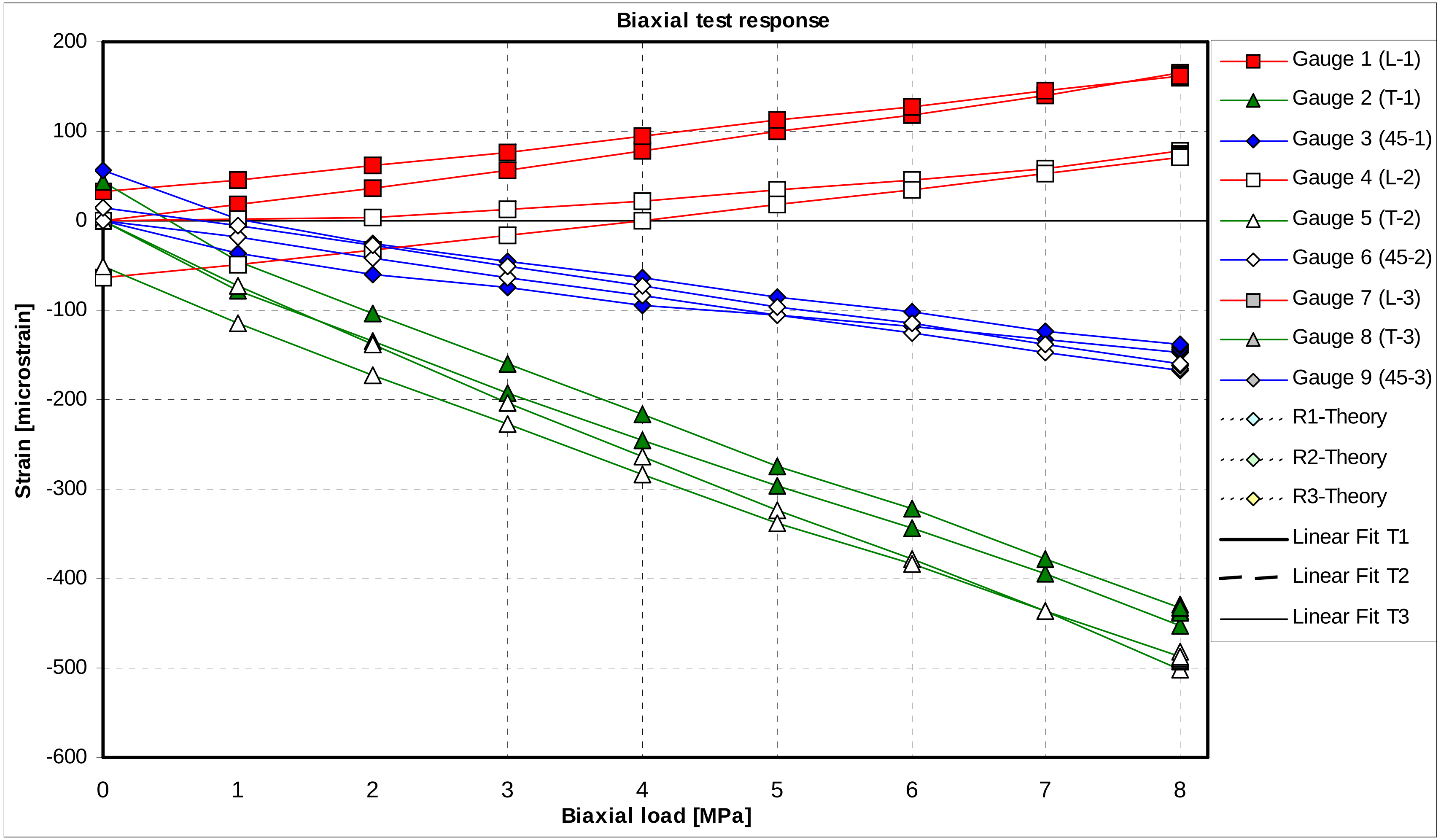

Figure E2. *Results from biaxial testing of test no. KQ0061G10:1:2, 5.18 m depth, excluding rosette no. 3.*

Appendix F

Stress calculation input data and results

Table F1. Measured in situ stresses for test no. KQ0061G10:1:2, 4.13 m depth.

VATTENFALL OVERCORING STRESS MEASUREMENTS

Project Description : Core disking APSE
Date : 2006-02-07
Borehole Dip : 90
Borehole Bearing : 0
Measurement Depth : 4.13 [m]

Input Data	Bearing (ball) - X [º]	Young's modulus [GPa]	Poisson's ratio	Needle bearing [º]	(values for gauge and resistance factor are always 2 and 1, respectively)	Overcoring Time [hh:mm:ss]	Overcoring Time [hh:mm:ss]
	7	64.4	0.26	-		Start=09:16:00	Stop=10:27:30

Strains	ε_{L1} (gauge no. 1) [μstrain]	ε_{T1} (gauge no. 2) [μstrain]	ε_{45_1} (gauge no. 3) [μstrain]	ε_{L2} (gauge no. 4) [μstrain]	ε_{T2} (gauge no. 5) [μstrain]	ε_{45_2} (gauge no. 6) [μstrain]	ε_{L3} (gauge no. 7) [μstrain]	ε_{T3} (gauge no. 8) [μstrain]	ε_{45_3} (gauge no. 9) [μstrain]
	875	769	966	222	-121	-121	1755	1481	1637

Principal Stresses

σ_1 [MPa]	σ_1 - Dip [º]	σ_1 - Bearing [º]	σ_2 [MPa]	σ_2 - Dip [º]	σ_2 - Bearing [º]	σ_3 [MPa]	σ_3 - Dip [º]	σ_3 - Bearing [º]
82.3	73.5	284.6	47.4	12.0	148.7	14.6	11.1	56.3

Horizontal and Vertical Stresses

Major stress σ_A [MPa]	σ_A - Bearing [º]	Minor stress σ_B [MPa]	σ_B - Bearing [º]	Vertical stress σ_z [MPa]	Error (sum of squares)	Strains re-calculated?
49.0	143.8	17.0	53.8	78.3	1183648.7	No

Table F2. Measured in situ stresses for test no. KQ0061G10:2:1, 5.18 m depth.

VATTENFALL OVERCORING STRESS MEASUREMENTS

Project Description : Core disking APSE
Date : 2006-02-08
Borehole Dip : 90
Borehole Bearing : 0
Measurement Depth : 5.18 [m]

Input Data	Bearing (ball) - X [º]	Young's modulus [GPa]	Poisson's ratio	Needle bearing [º]	(values for gauge and resistance factor are always 2 and 1, respectively)	Overcoring Time [hh:mm:ss]	[hh:mm:ss]
	17	51.7	0.27	-		Start=08:40:30	Stop=10:07:00

Strains	ε_{L1} (gauge no. 1) [µstrain]	ε_{T1} (gauge no. 2) [µstrain]	ε_{45_1} (gauge no. 3) [µstrain]	ε_{L2} (gauge no. 4) [µstrain]	ε_{T2} (gauge no. 5) [µstrain]	ε_{45_2} (gauge no. 6) [µstrain]	ε_{L3} (gauge no. 7) [µstrain]	ε_{T3} (gauge no. 8) [µstrain]	ε_{45_3} (gauge no. 9) [µstrain]
	64	-136	12	64	233	-38	64	635	683

Principal Stresses

σ_1 [MPa]	σ_1 - Dip [º]	σ_1 - Bearing [º]	σ_2 [MPa]	σ_2 - Dip [º]	σ_2 - Bearing [º]	σ_3 [MPa]	σ_3 - Dip [º]	σ_3 - Bearing [º]
18.1	32.9	299.7	5.3	52.4	152.6	1.5	16.1	40.5

Horizontal and Vertical Stresses

Major stress σ_A [MPa]	σ_A - Bearing [º]	Minor stress σ_B [MPa]	σ_B - Bearing [º]	Vertical stress σ_z [MPa]	Error (sum of squares)	Strains re-calculated?
14.3	122.7	1.8	32.7	8.8	8450.0	Yes

Appendix G

Photos of core samples

KQ0061G10:1:2, 4.13 m — pilot core (30 cm shown)

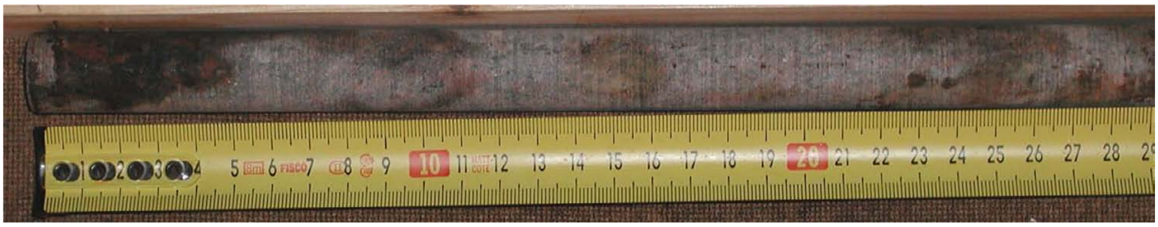

KQ0061G10:1:2, 4.13 m — overcore sample (30 cm shown)

KQ0061G10:2:1, 5.18 m — pilot core (30 cm shown)

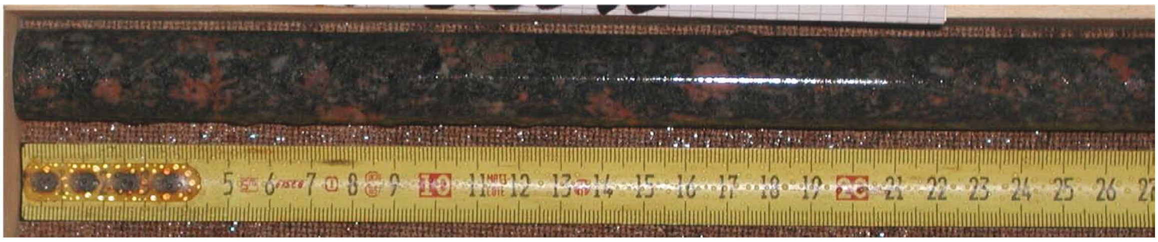

KQ0061G10:2:1, 5.18 m— overcore sample (30 cm shown)

Figure G1. *Photos of pilot core and overcore sample for borehole KQ0061G10.*

Appendix H

Numerical modeling results

The first set of figures (Figure H1 through Figure H3) shows the principal stress redistribution (colored by magnitude of: first σ_1, then σ_2 and finally σ_3) projected on a vertical cross section perpendicular to the axis of the tunnel in the center of the pillar when the TASQ tunnel is excavated. The results belong to Run3 and Run4 (see also Table 6-5).

The second set of figures (Figure H4 to Figure H6) shows the principal stress redistribution (colored by magnitude of: first σ_1, then σ_2 and finally σ_3) projected on a vertical cross-section along the axis of the TASQ tunnel, when the deposition holes are excavated. The results belong to Run3 and Run4 (see also Table 6-5).

The third set of figures (Figure H7 through Figure H15) shows the principal stress redistribution (colored by magnitude of: first σ_1, then σ_2 and finally σ_3) projected on a horizontal cross-section at different depths from the floor of the TASQ tunnel when the deposition holes are excavated. The results belong to Run3 and Run4 (see also Table 6-5).

Figure H16shows the fracture shear displacements on a horizontal cross-section at 1.5m depth from the floor of the TASQ tunnel when the deposition holes are excavated. The results belong to Run3 and Run4 (see also Table 6-5).

Figure H17shows the fracture shear displacements on a horizontal cross-section at 1.5m depth from the floor of the TASQ tunnel when the drilling of the de-stressing slot is complete. The results belong to Run3 and Run4 (see also Table 6-5).

The final set of figures (Figure H18 through Figure H26) shows the principal stress redistribution (colored by magnitude of: first σ_1, then σ_2 and finally σ_3) projected on a horizontal cross-section at different depths from the floor of the TASQ tunnel when the pillar has been removed. The results belong to Run3 and Run4 (see also Table 6-5).

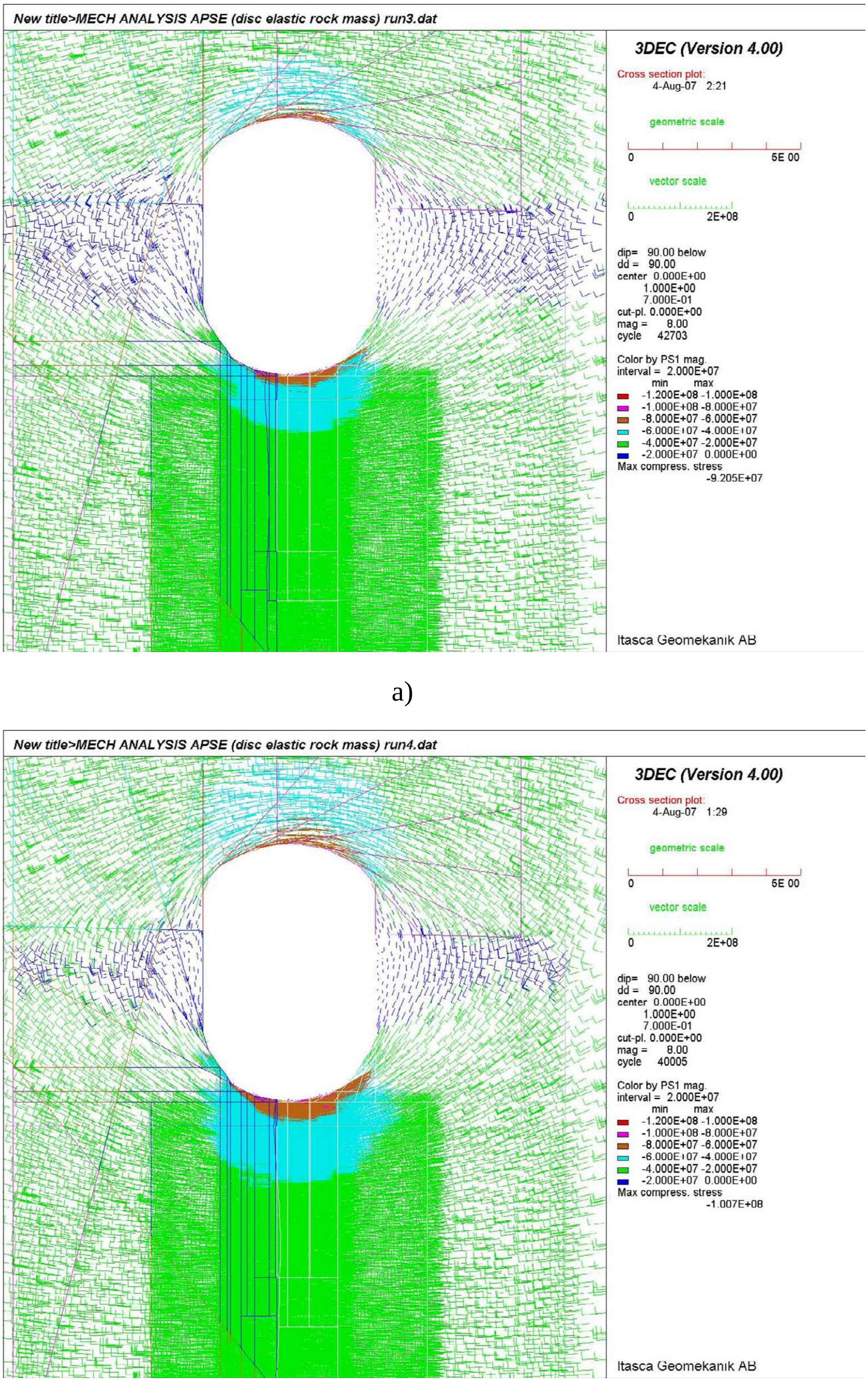

a)

b)

Figure H1. *Vertical cross section showing the projected principal stress on the center of the pillar before the deposition holes are excavated (Colors by magnitude of σ_1) for a) Run3 and b) Run4.*

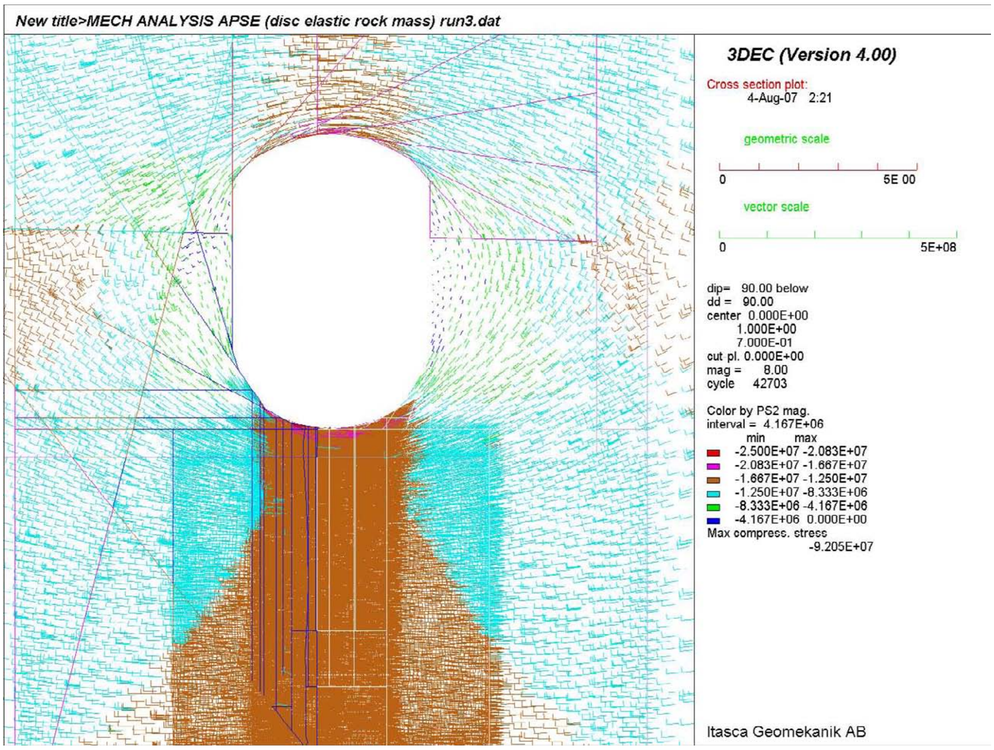

a)

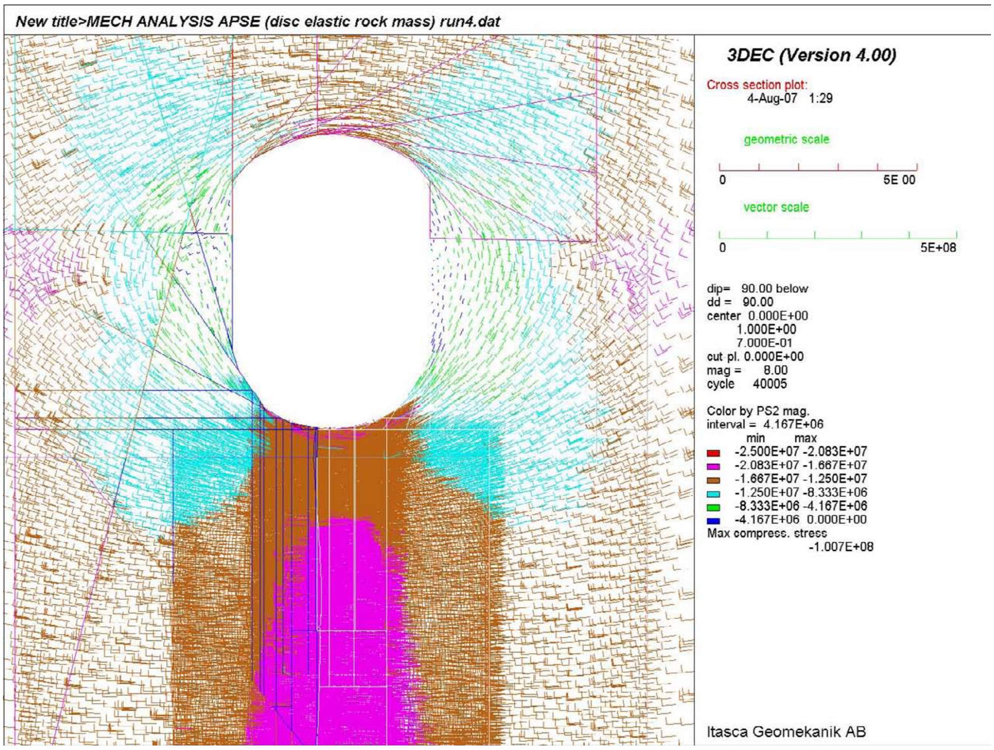

b)

Figure H2. *Vertical cross section showing the projected principal stress on the center of the pillar before the deposition holes are excavated (Colors by magnitude of σ_2) for a) Run3 and b) Run4.*

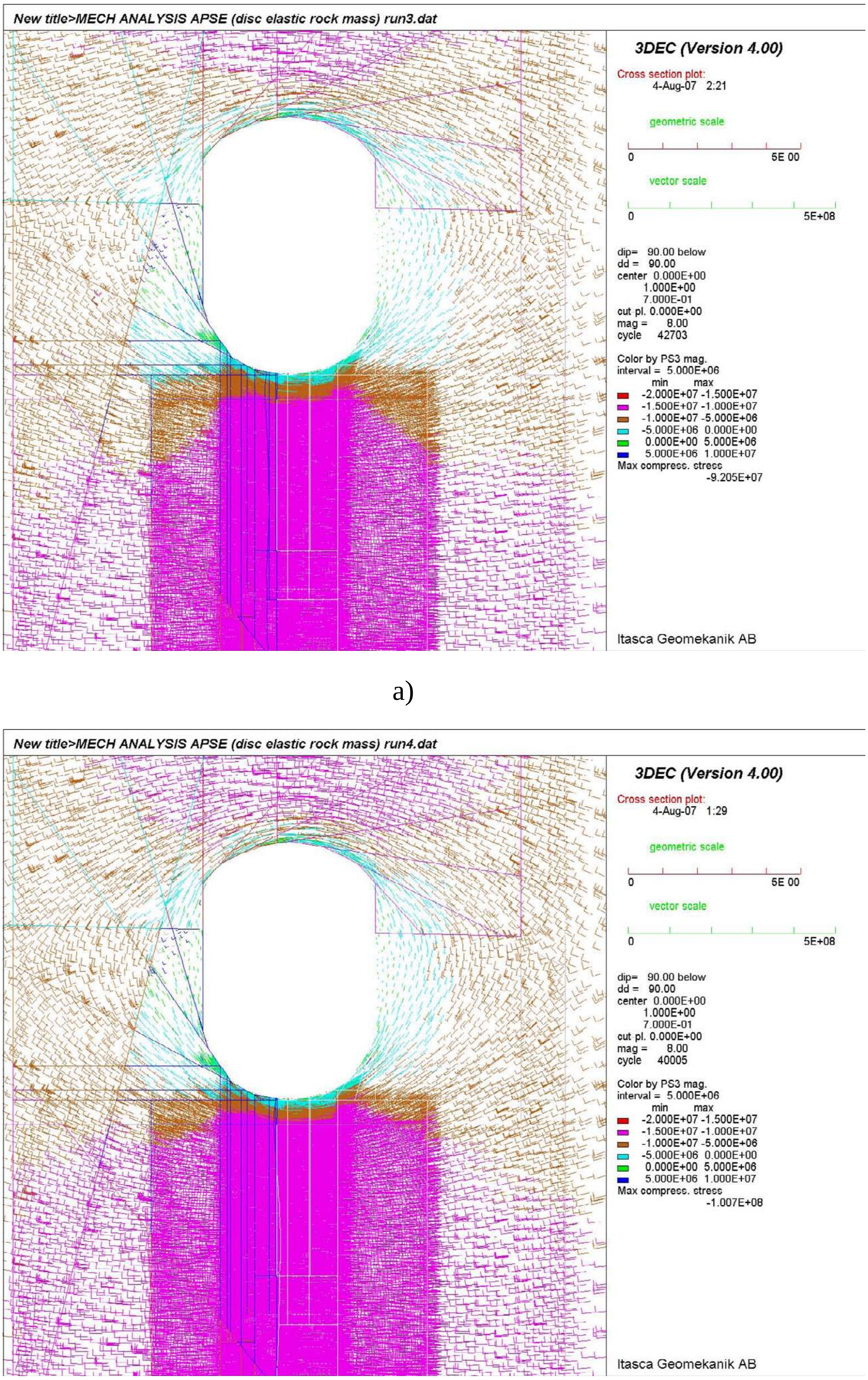

a)

b)

Figure H3. *Vertical cross section showing the projected principal stress on the center of the pillar before the deposition holes are excavated (Colors by magnitude of σ_3) for a) Run3 and b) Run4.*

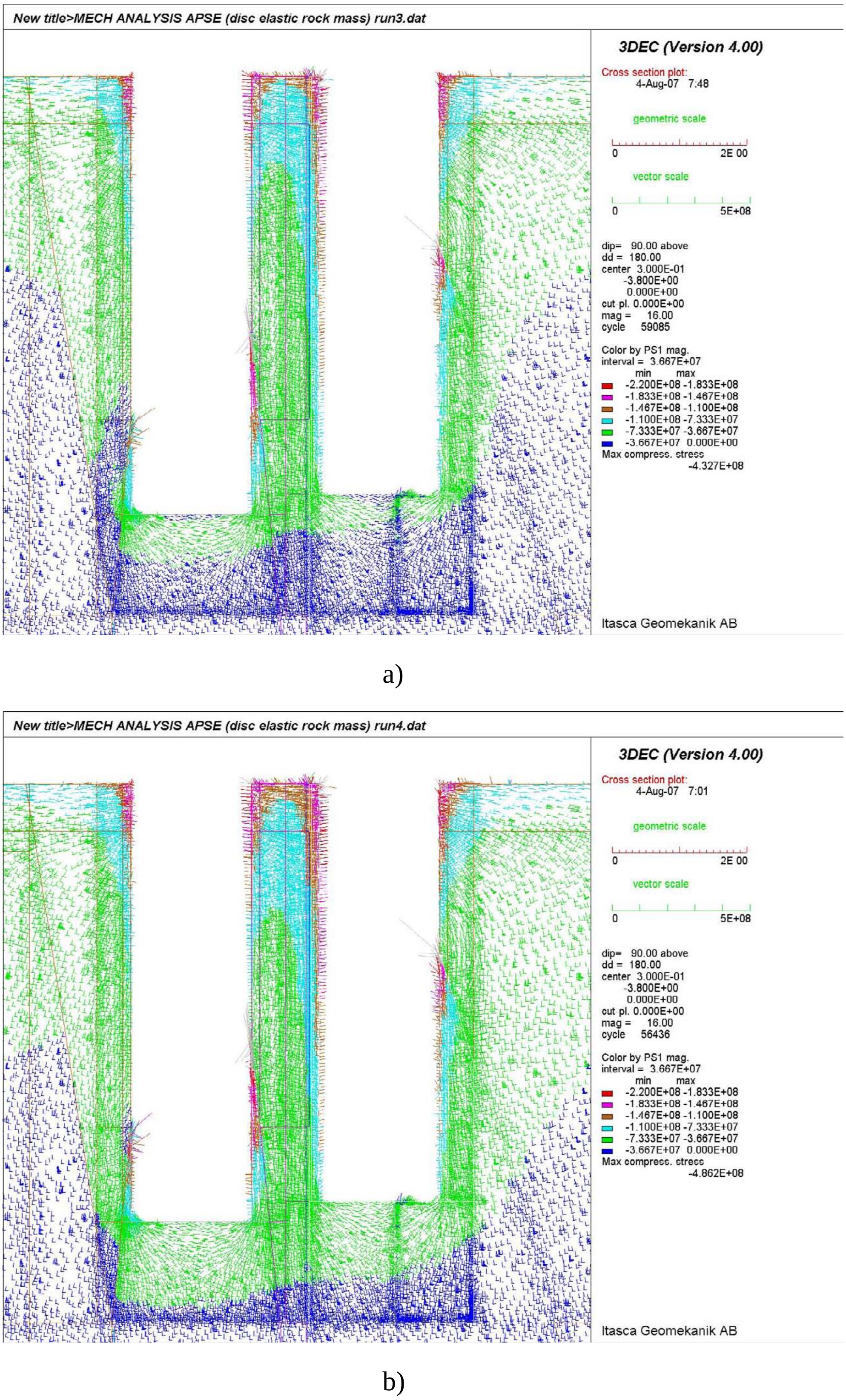

a)

b)

Figure H4. *Vertical cross-section showing the projected principal stress along the axis of the tunnel after the deposition holes have been excavated (Colors by magnitude of σ_1) for a) Run3 and b) Run4.*

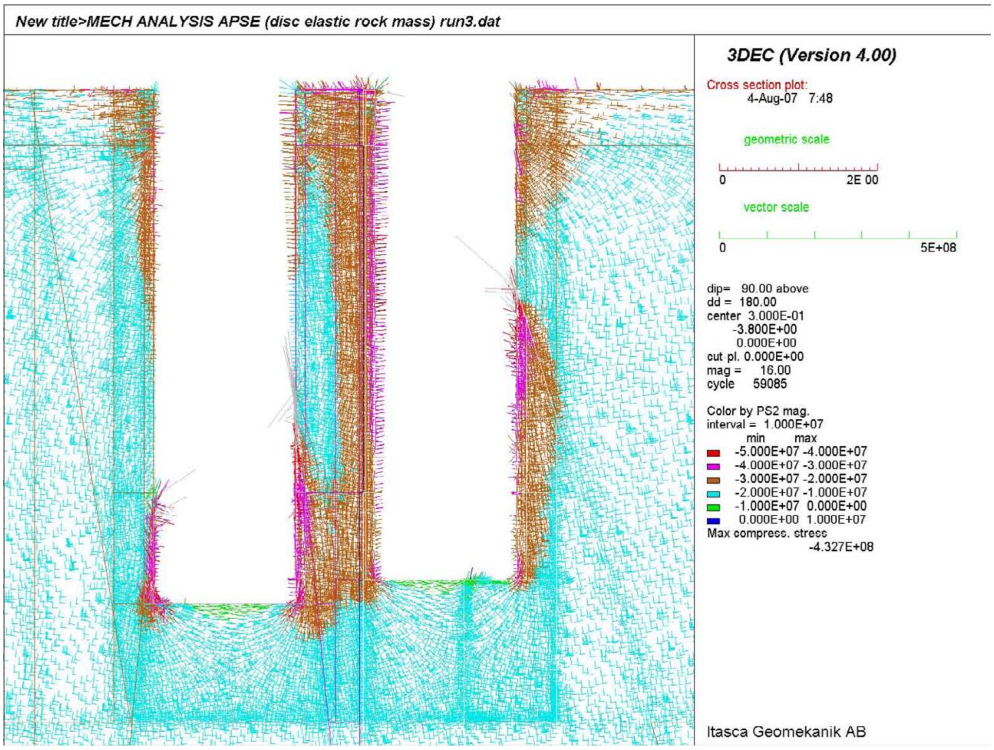

a)

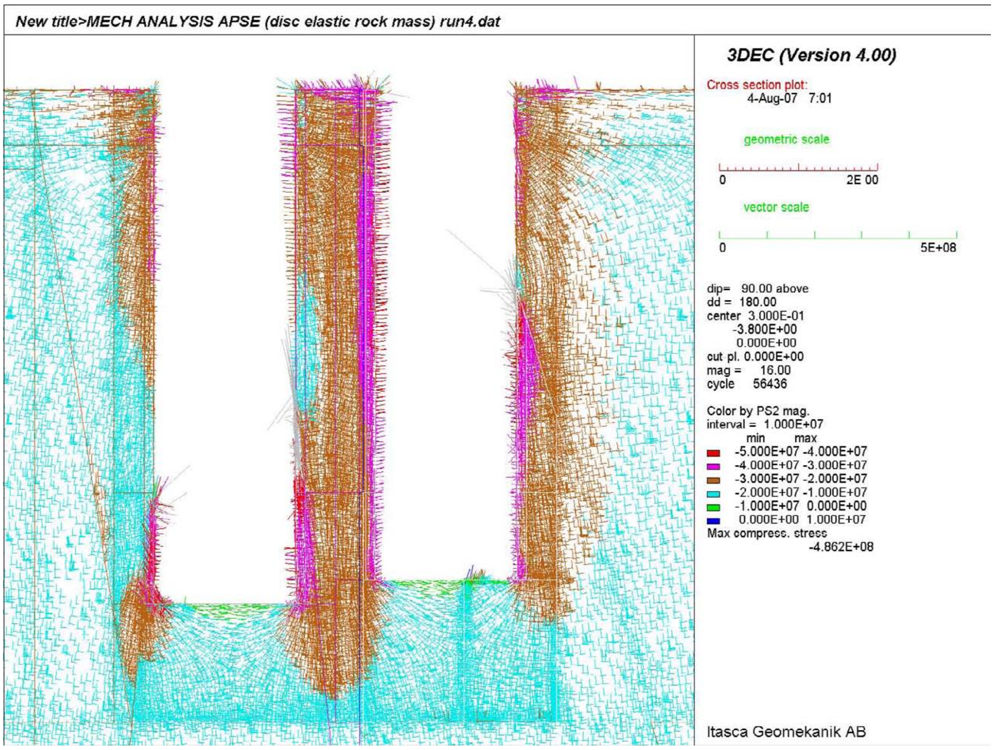

b)

Figure H5. *Vertical cross-section showing the projected principal stress along the axis of the tunnel after the deposition holes have been excavated (Colors by magnitude of σ_2) for a) Run3 and b) Run4.*

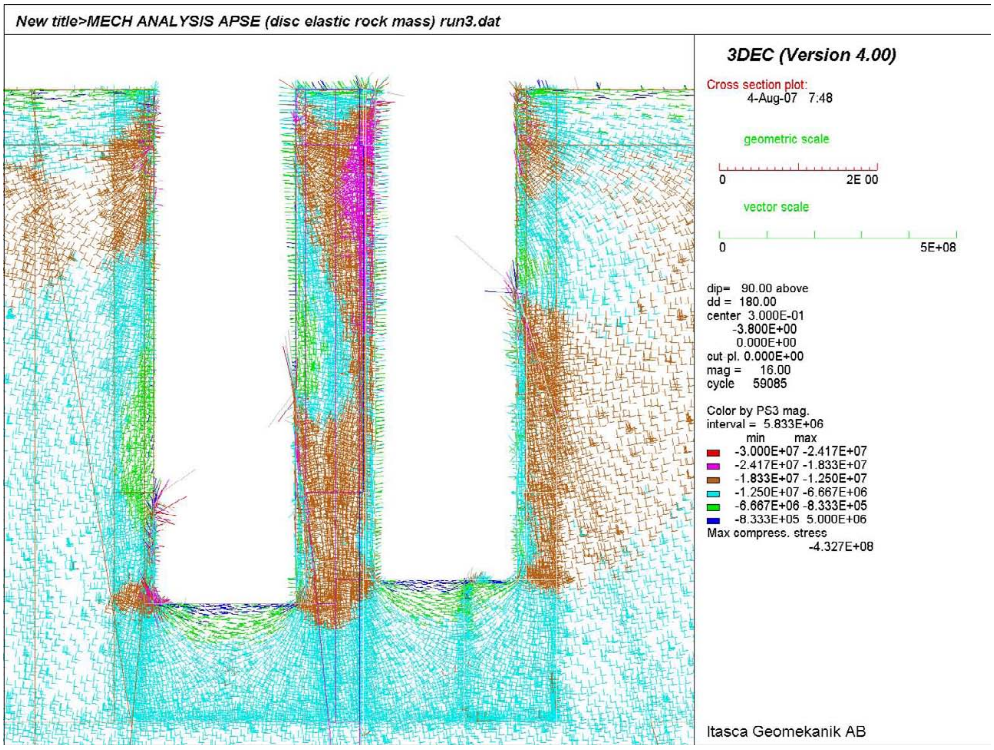

a)

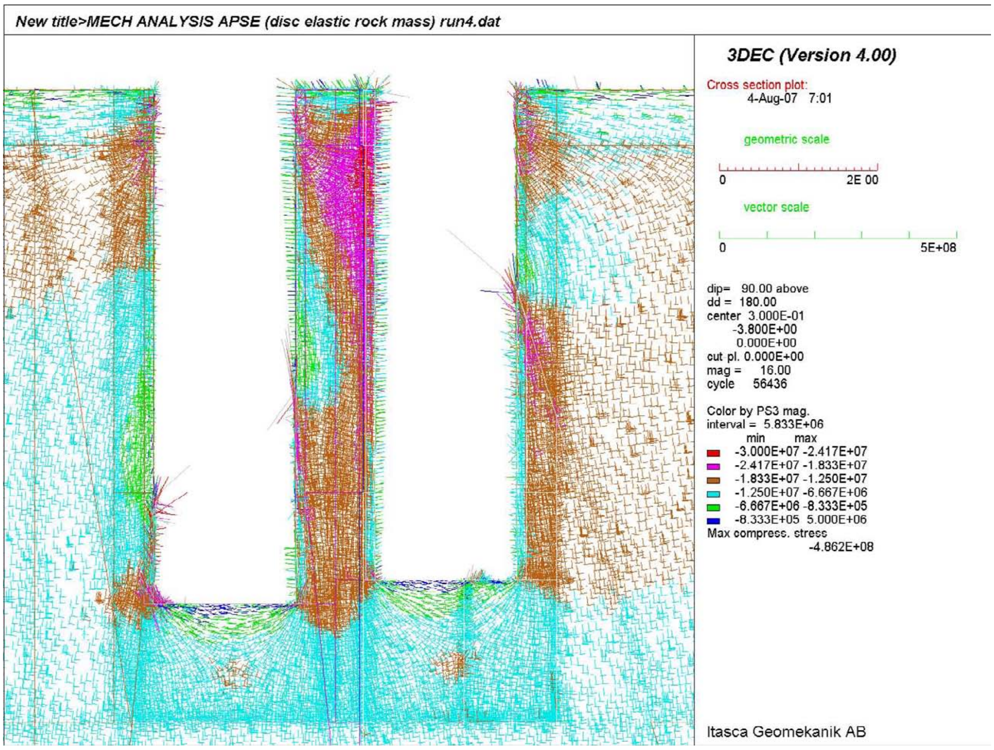

b)

Figure H6. *Vertical cross-section showing the projected principal stress along the axis of the tunnel after the deposition holes have been excavated (Colors by magnitude of* σ_3*) for a) Run3 and b) Run4.*

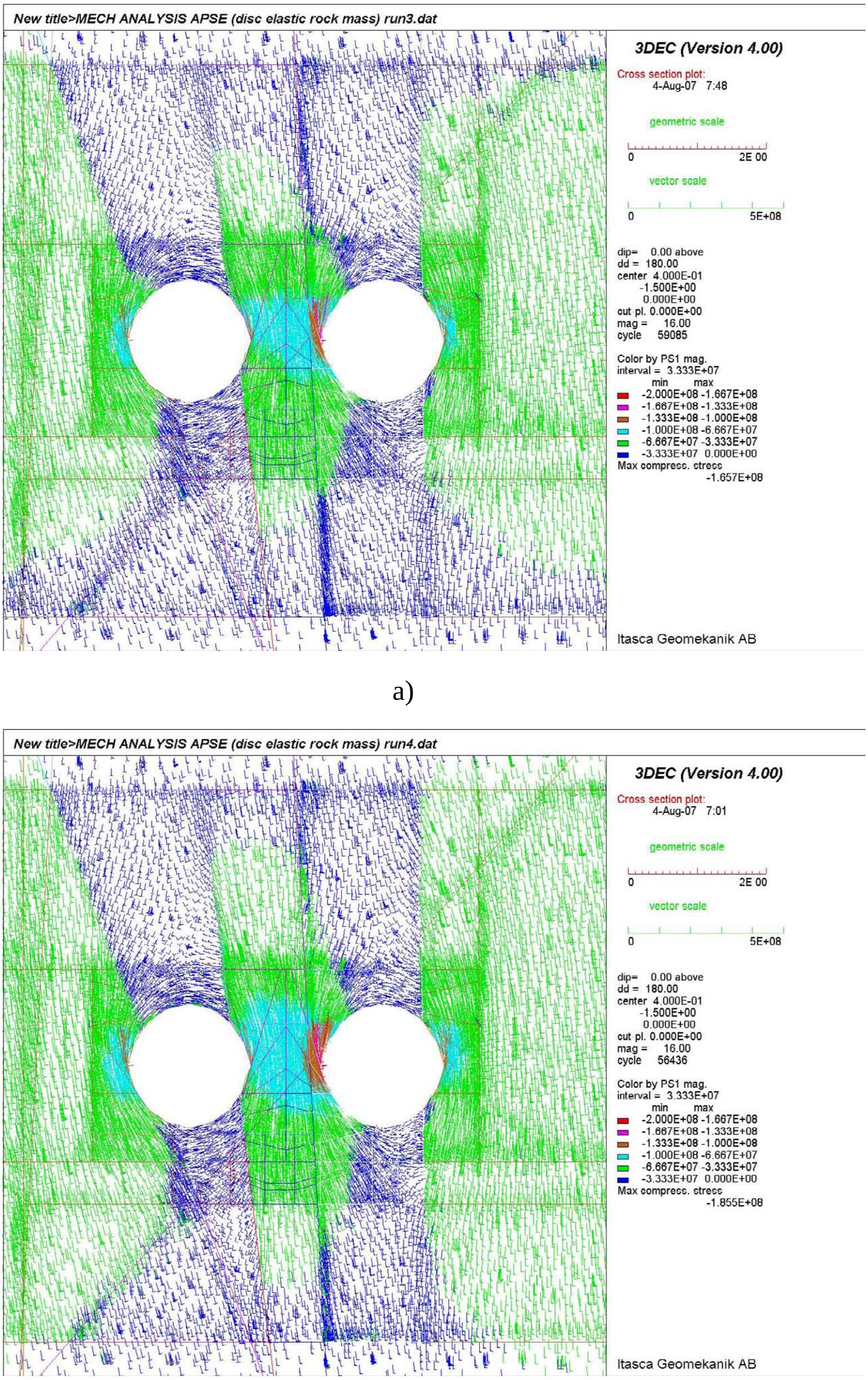

a)

b)

Figure H7. *Horizontal cross-section showing the projected principal stress at 1.5 m depth from the floor of the APSE tunnel after the deposition holes have been excavated (Colors by magnitude of* σ_1*) for a) Run3 b) Run4.*

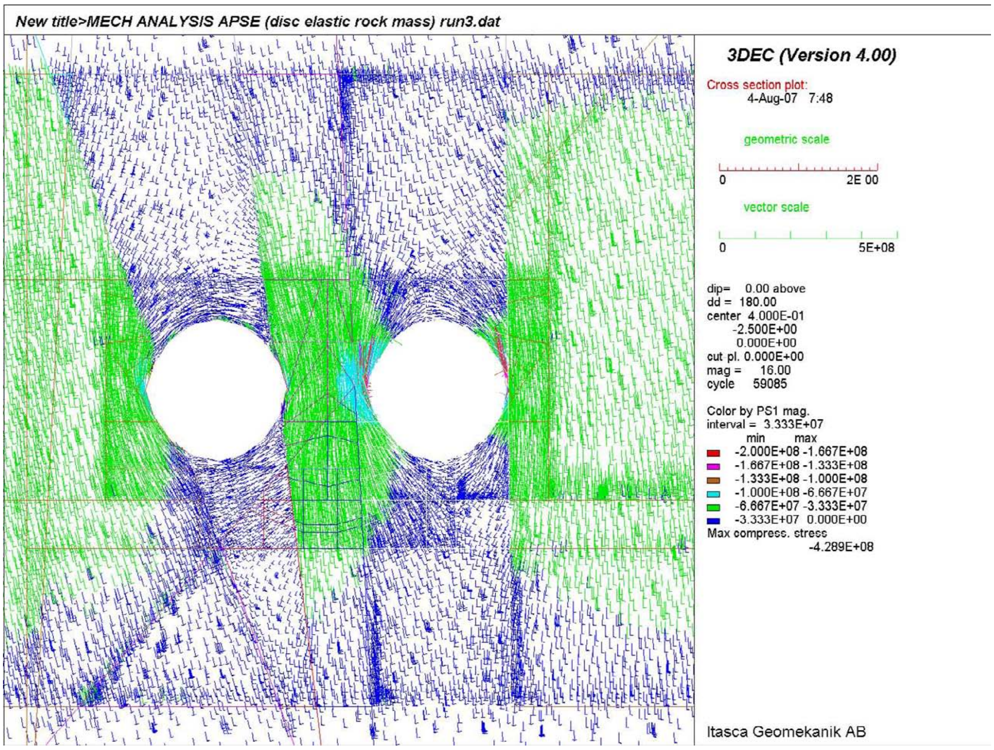

a)

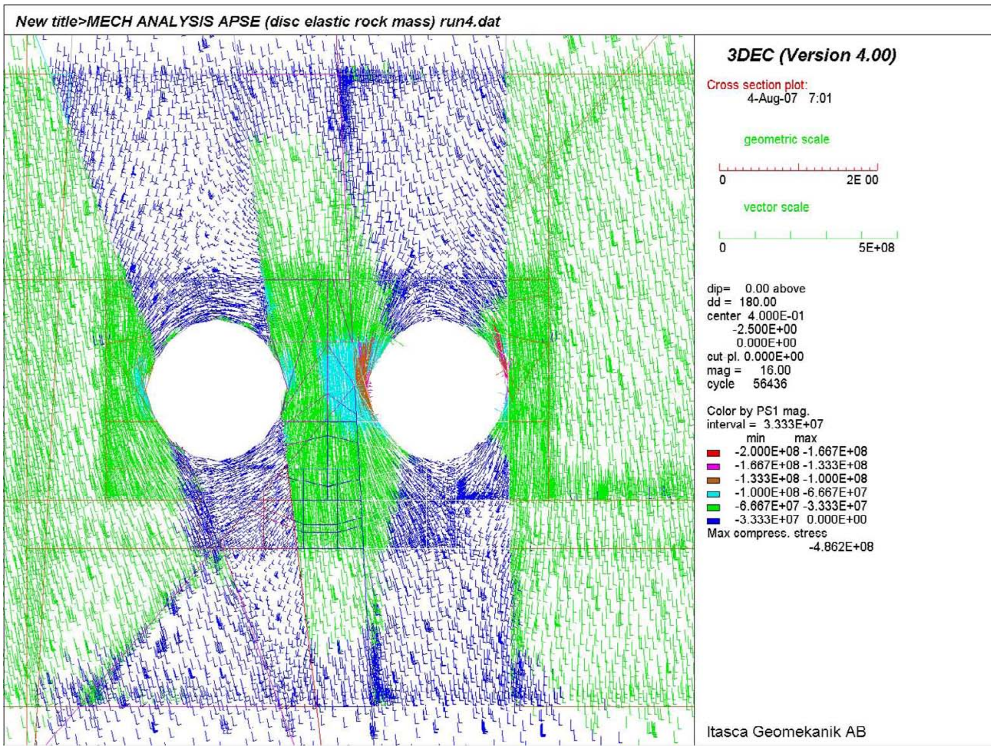

b)

Figure H8. *Horizontal cross-section showing the projected principal stress at 2.5 m depth from the floor of the APSE tunnel after the deposition holes have been excavated (Colors by magnitude of σ_1) for a) Run3 b) Run4.*

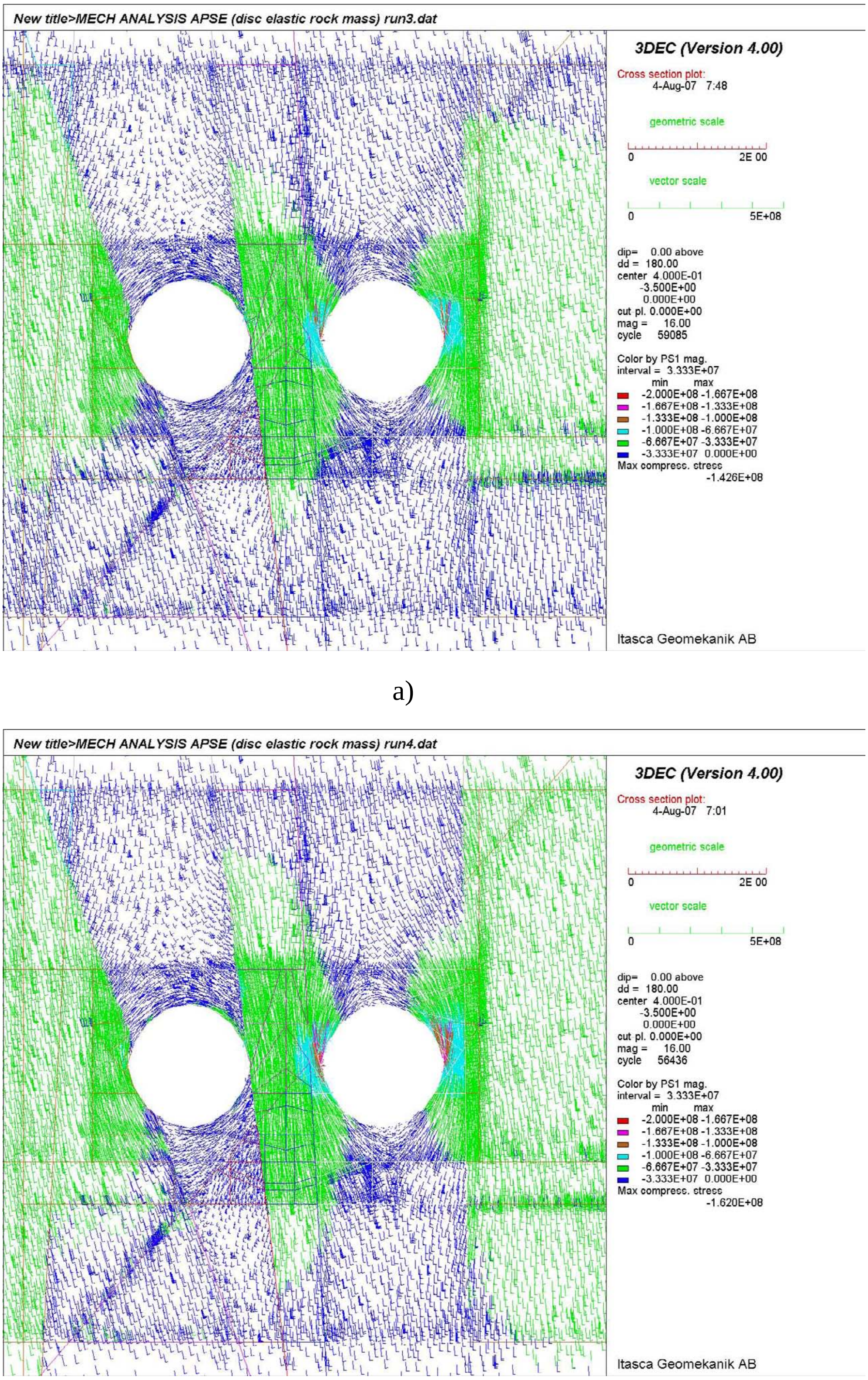

a)

b)

Figure H9. *Horizontal cross-section showing the projected principal stress at 3.5 m depth from the floor of the APSE tunnel after the deposition holes have been excavated (Colors by magnitude of σ_1) for a) Run3 b) Run4.*

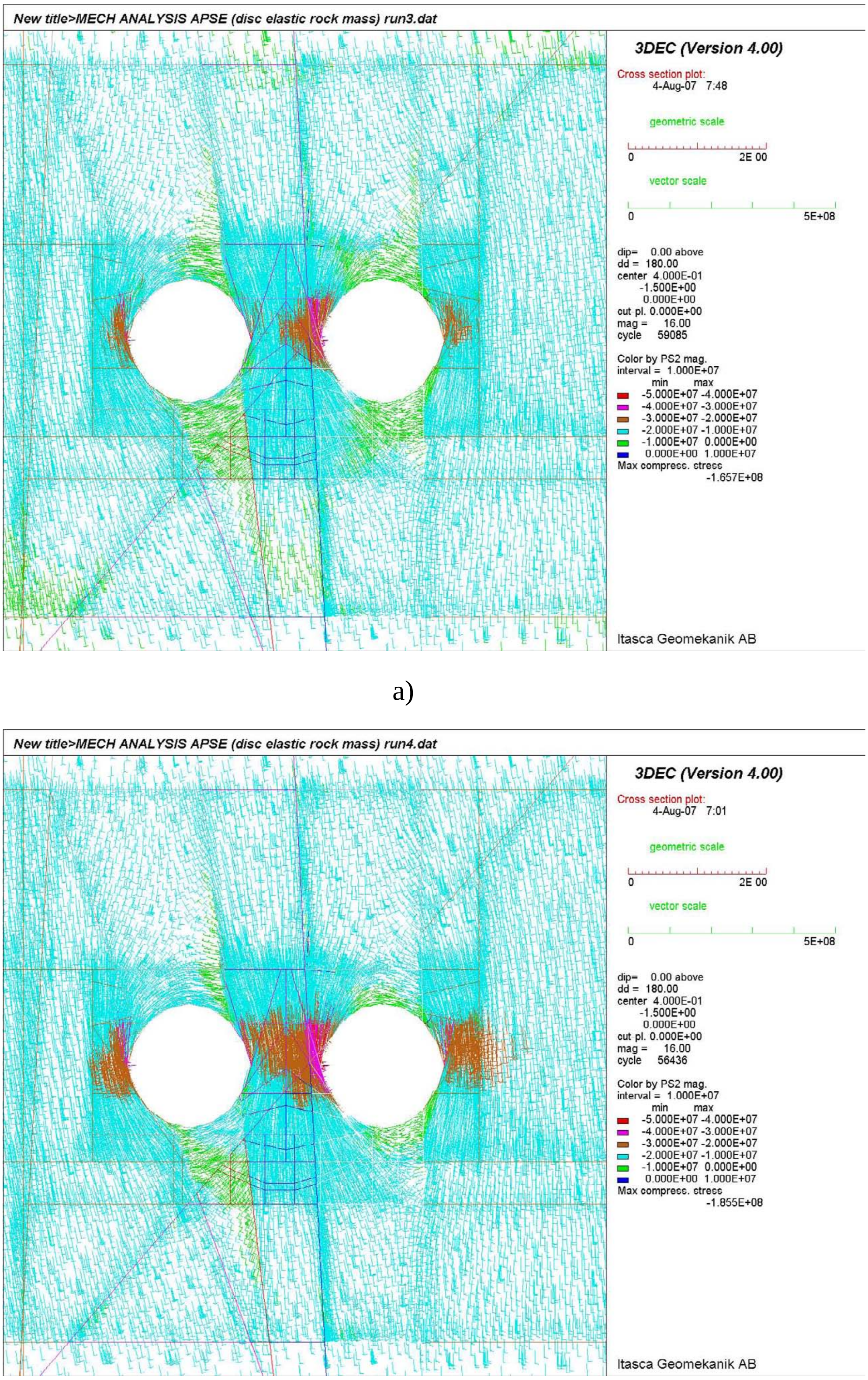

a)

b)

Figure H10. *Horizontal cross-section showing the projected principal stress at 1.5 m depth from the floor of the APSE tunnel after the deposition holes have been excavated (Colors by magnitude of* σ_2*) for a) Run3 b) Run4.*

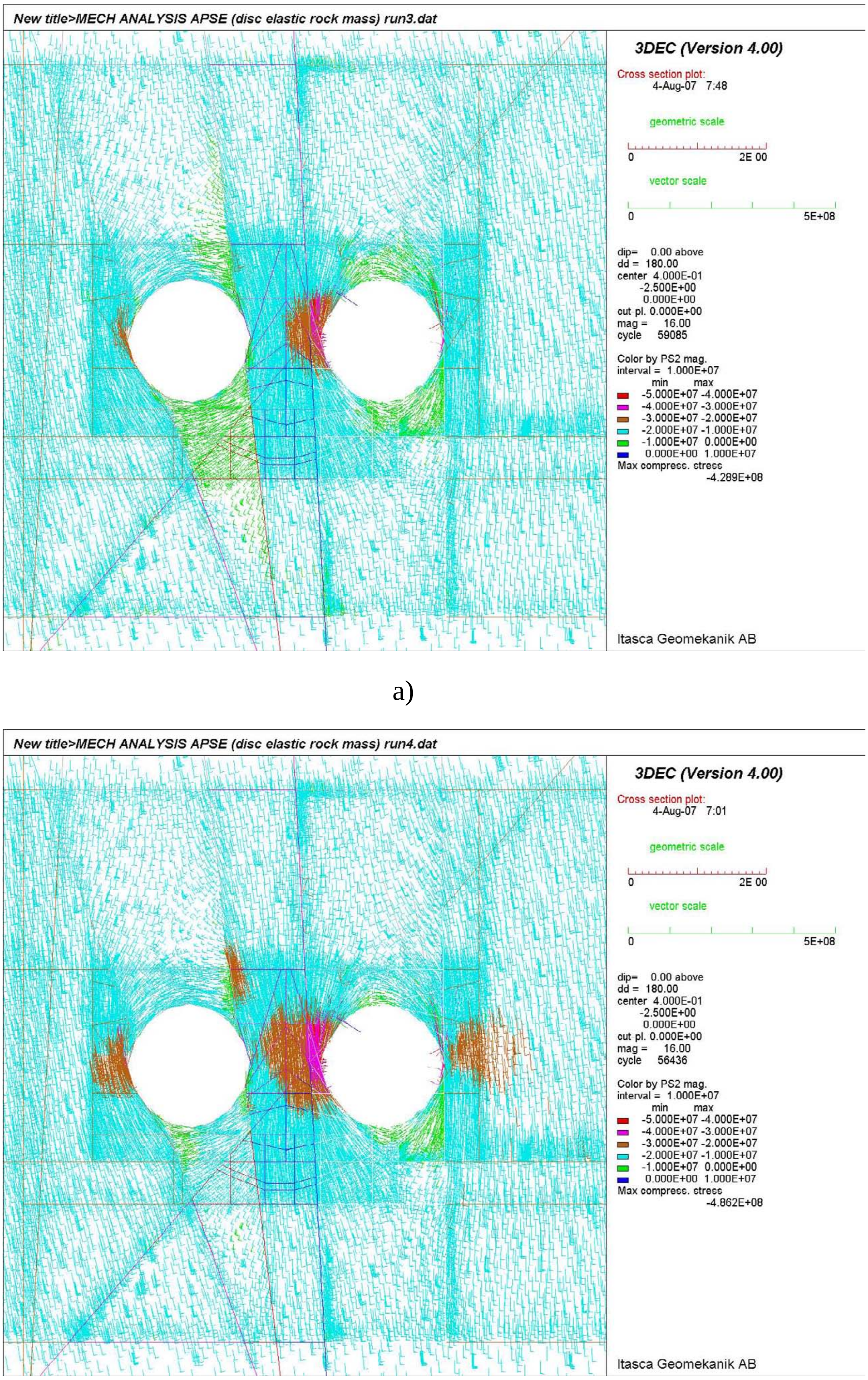

a)

b)

Figure H11. *Horizontal cross-section showing the projected principal stress at 2.5 m depth from the floor of the APSE tunnel after the deposition holes have been excavated (Colors by magnitude of σ_2) for a) Run3 b) Run4.*

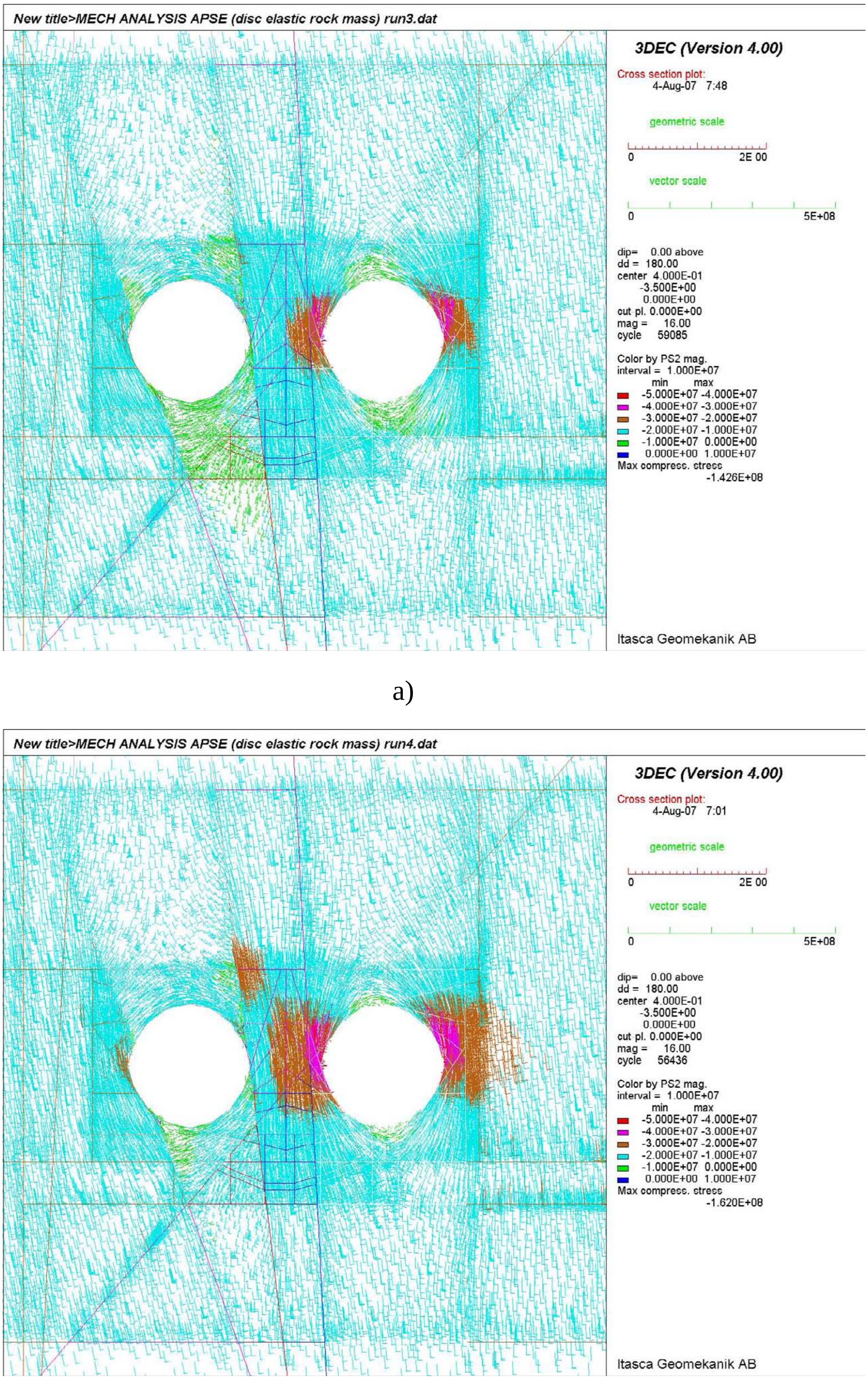

Figure H12. *Horizontal cross-section showing the projected principal stress at 3.5 m depth from the floor of the APSE tunnel after the deposition holes have been excavated (Colors by magnitude of* σ_2*) for a) Run3 b) Run4.*

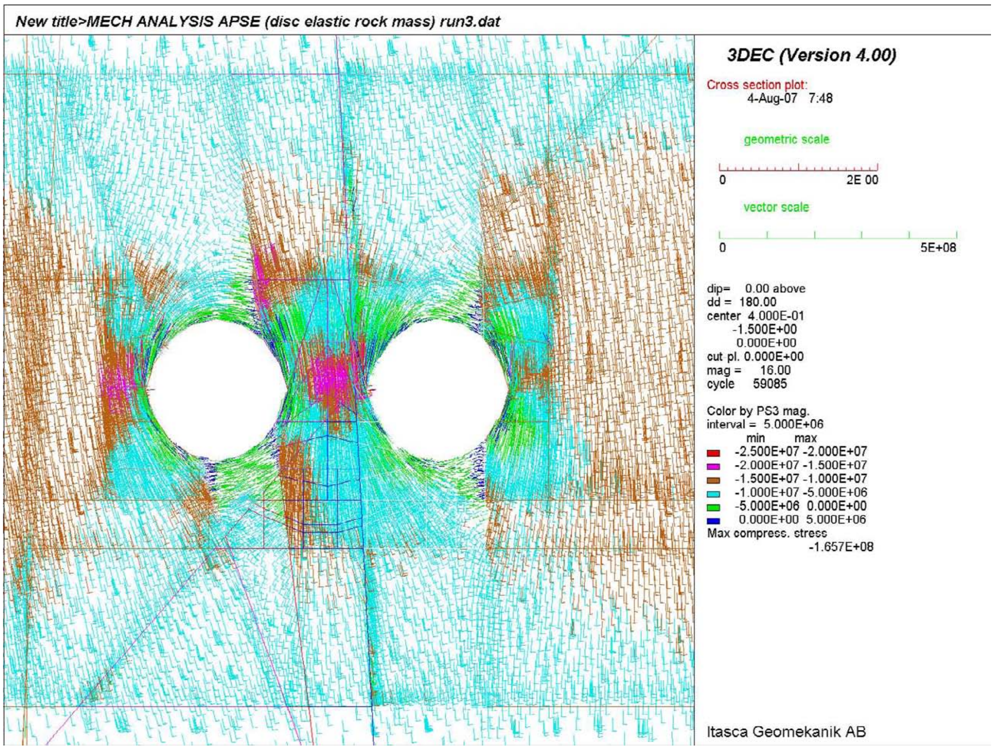

a)

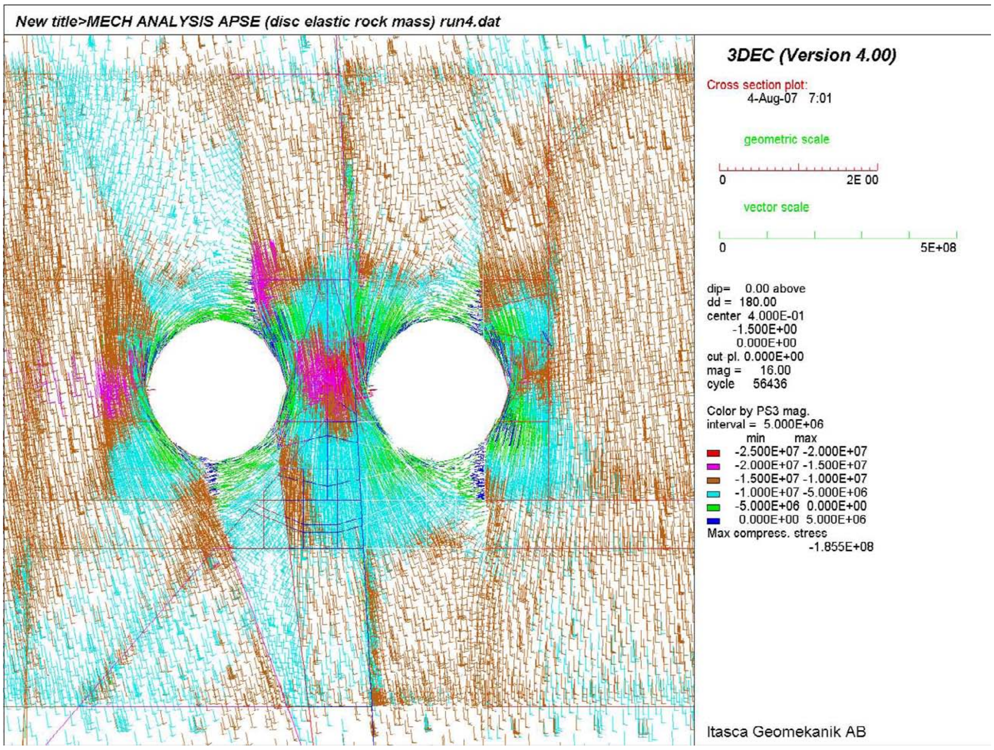

b)

Figure H13. *Horizontal cross-section showing the projected principal stress at 1.5 m depth from the floor of the APSE tunnel after the deposition holes have been excavated (Colors by magnitude of* σ_3*) for a) Run3 b) Run4.*

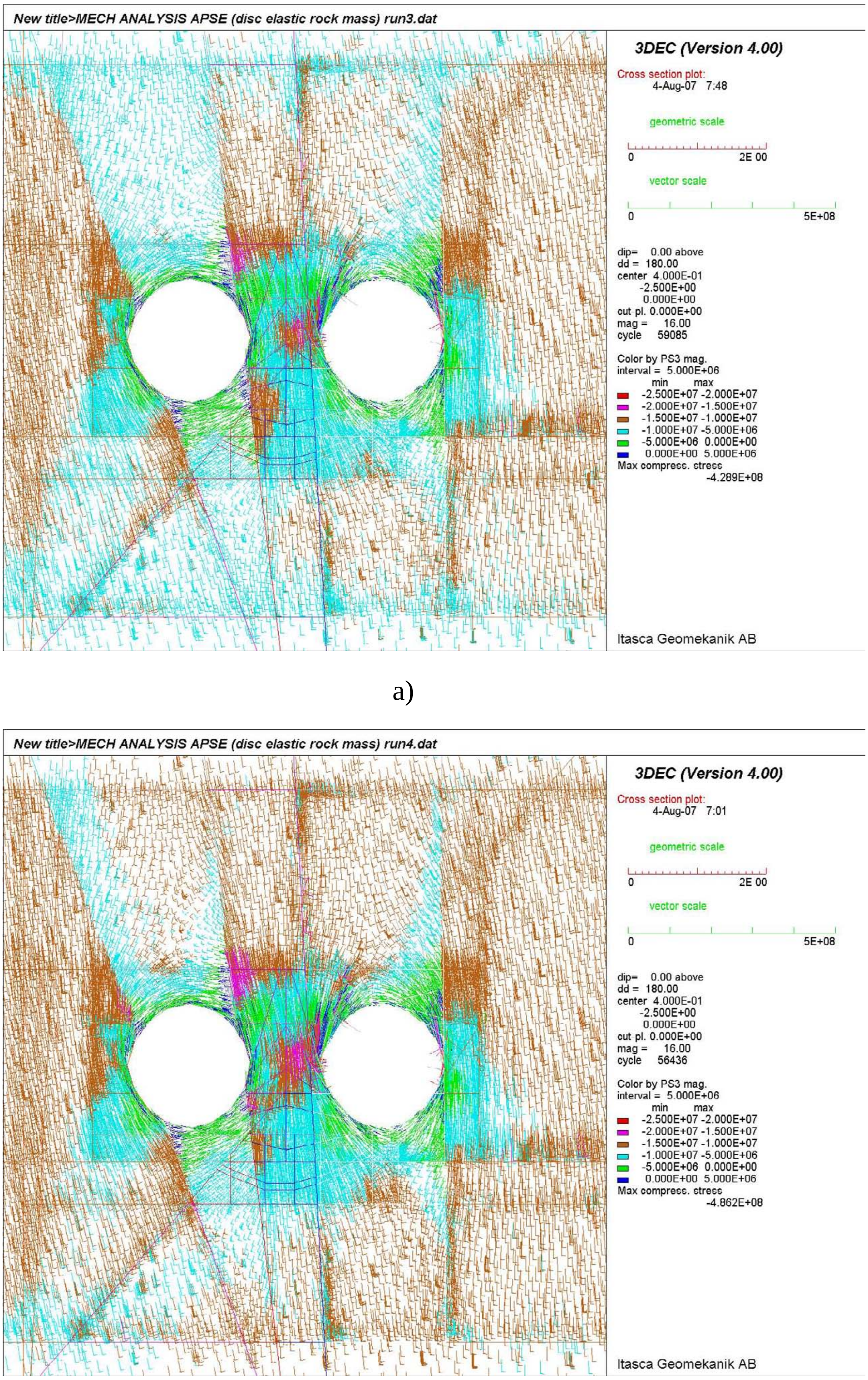

Figure H14. *Horizontal cross-section showing the projected principal stress at 2.5 m depth from the floor of the APSE tunnel after the deposition holes have been excavated (Colors by magnitude of σ_3) for a) Run3 b) Run4.*

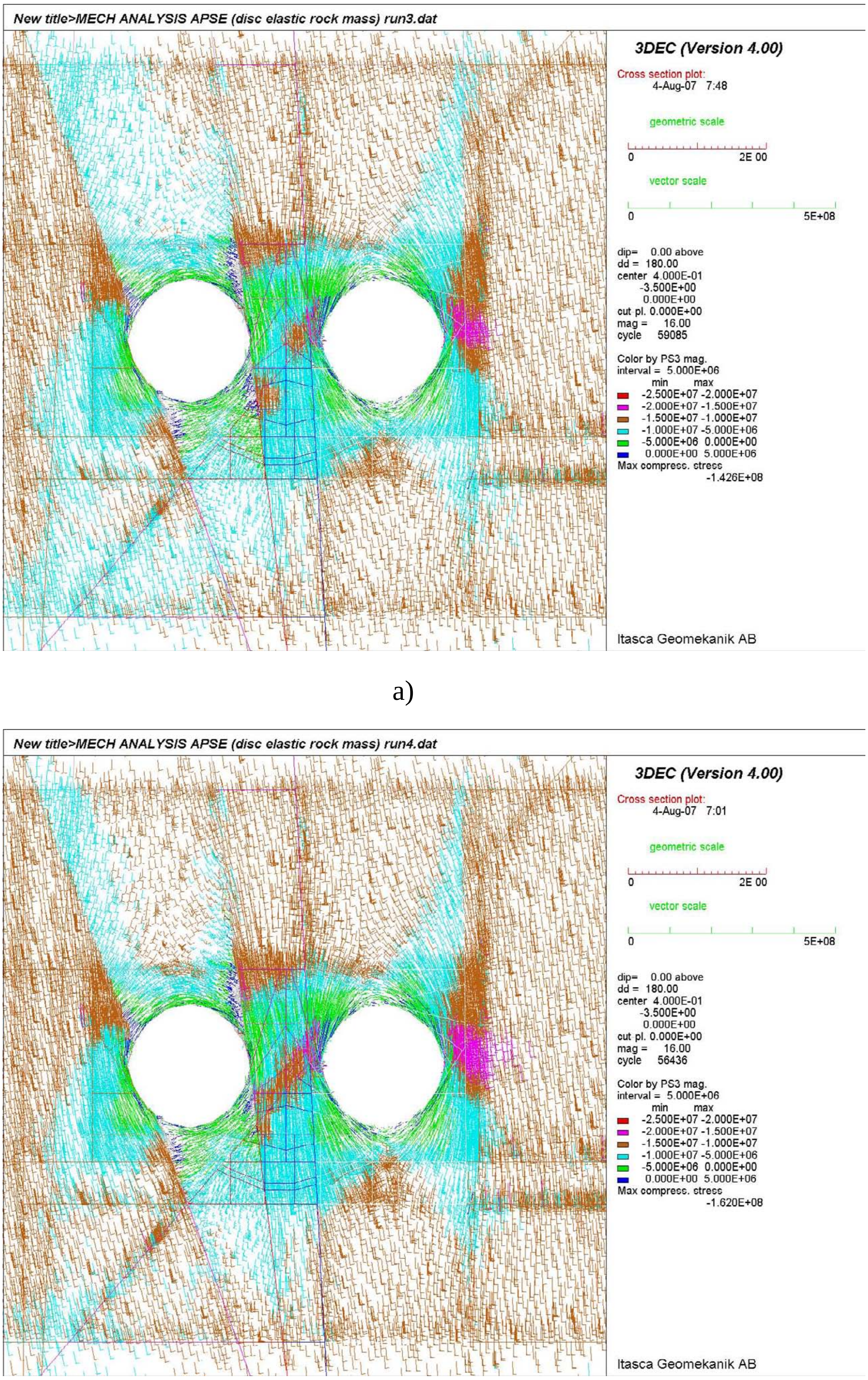

a)

b)

Figure H15. *Horizontal cross-section showing the projected principal stress at 3.5 m depth from the floor of the APSE tunnel after the deposition holes have been excavated (Colors by magnitude of σ_3) for a) Run3 b) Run4.*

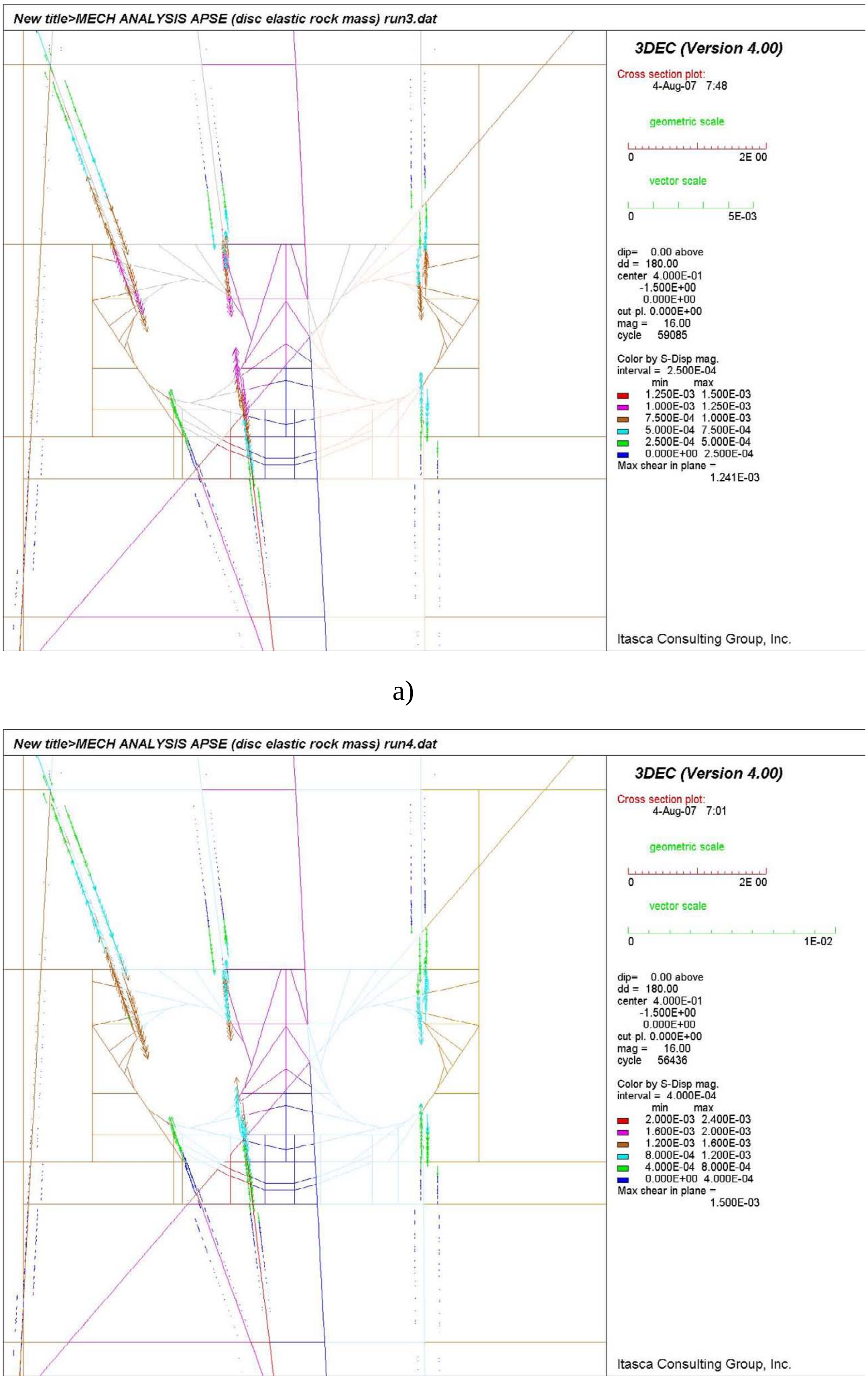

a)

b)

Figure H16. *Horizontal cross-section showing the fracture shear displacement at 1.5 m depth from the floor of the APSE tunnel after the deposition holes have been excavated for a) Run3 b) Run4.*

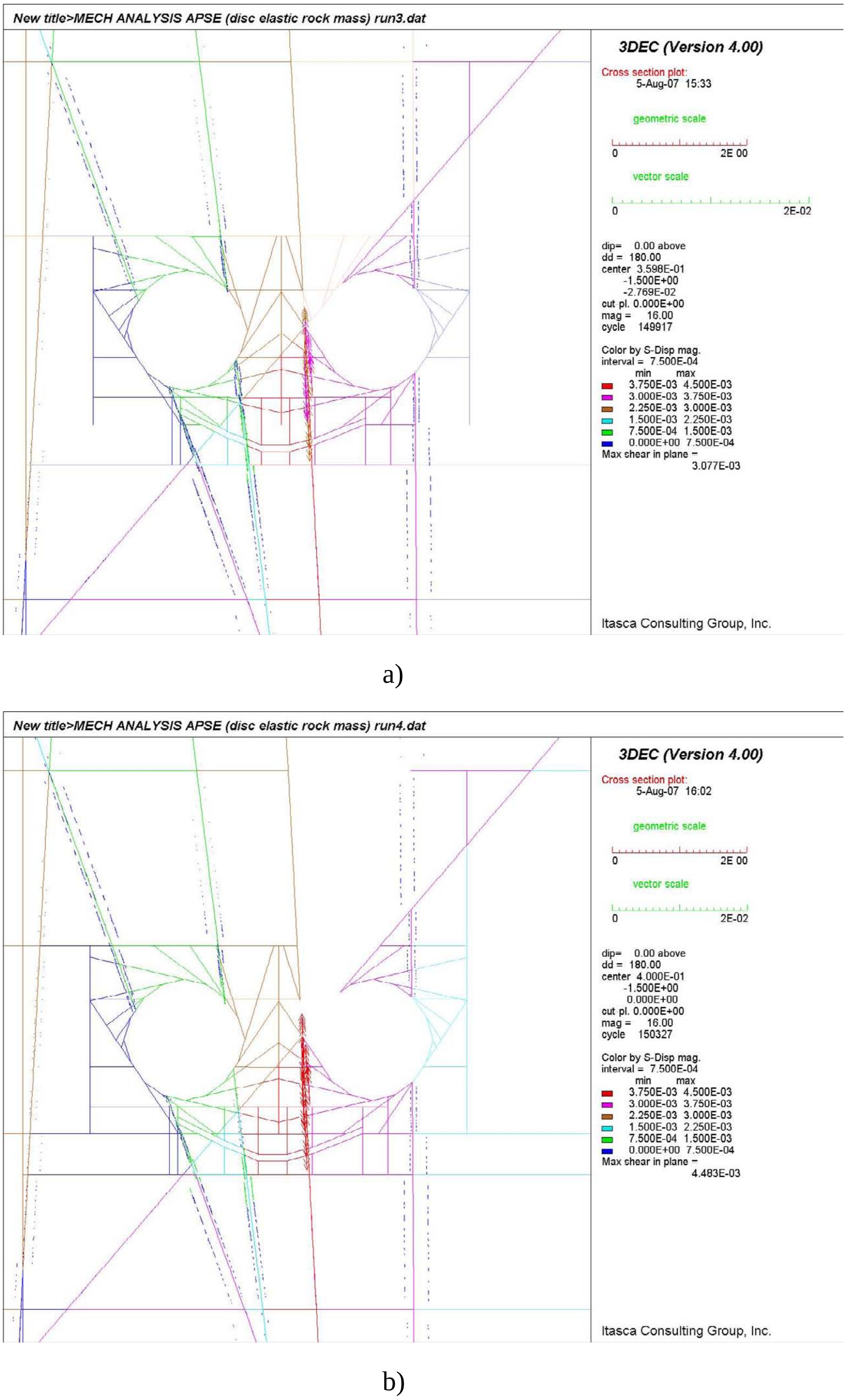

Figure H17. *Horizontal cross-section showing the fracture shear displacement at 1.5 m depth from the floor of the APSE tunnel after the drilling of the de-stressing slot for a) Run3 b) Run4.*

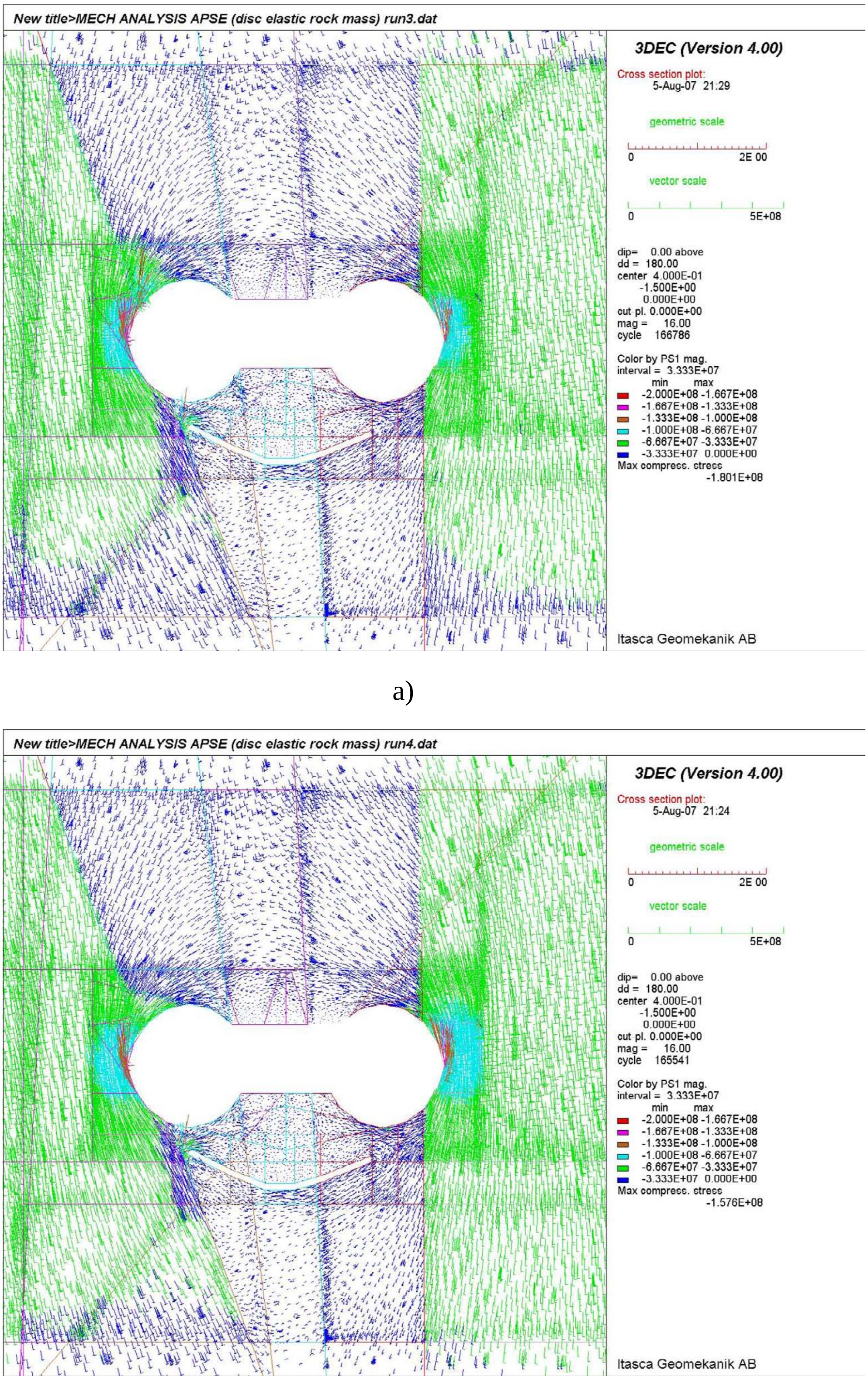

a)

b)

Figure H18. *Horizontal cross-section showing the projected principal stress at 1.5 m depth from the floor of the APSE tunnel after the pillar has been removed (Colors by magnitude of σ_1) for a) Run3 b) Run4.*

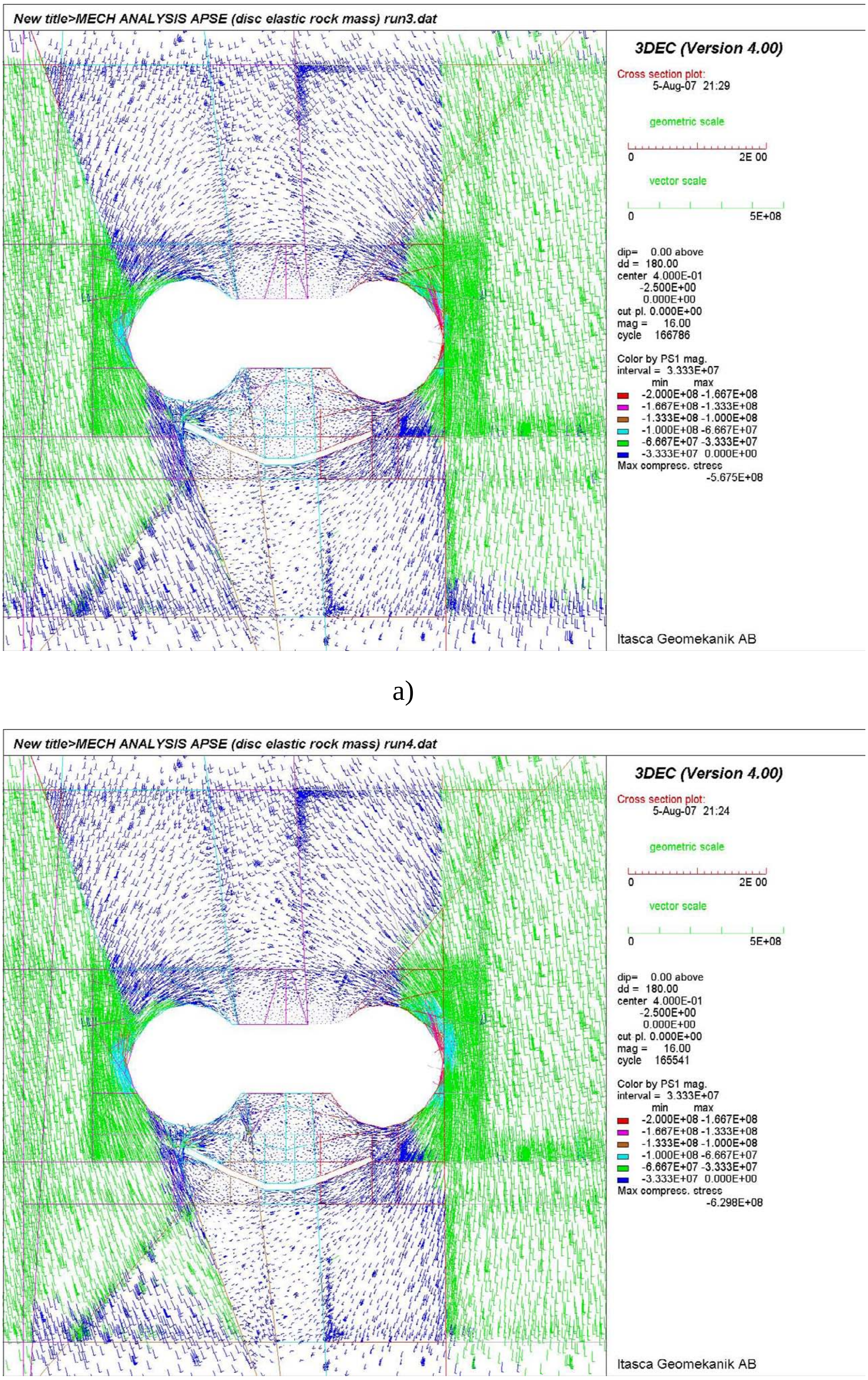

a)

b)

Figure H19. *Horizontal cross-section showing the projected principal stress at 2.5 m depth from the floor of the APSE tunnel after the pillar has been removed (Colors by magnitude of σ_1) for a) Run3 b) Run4.*

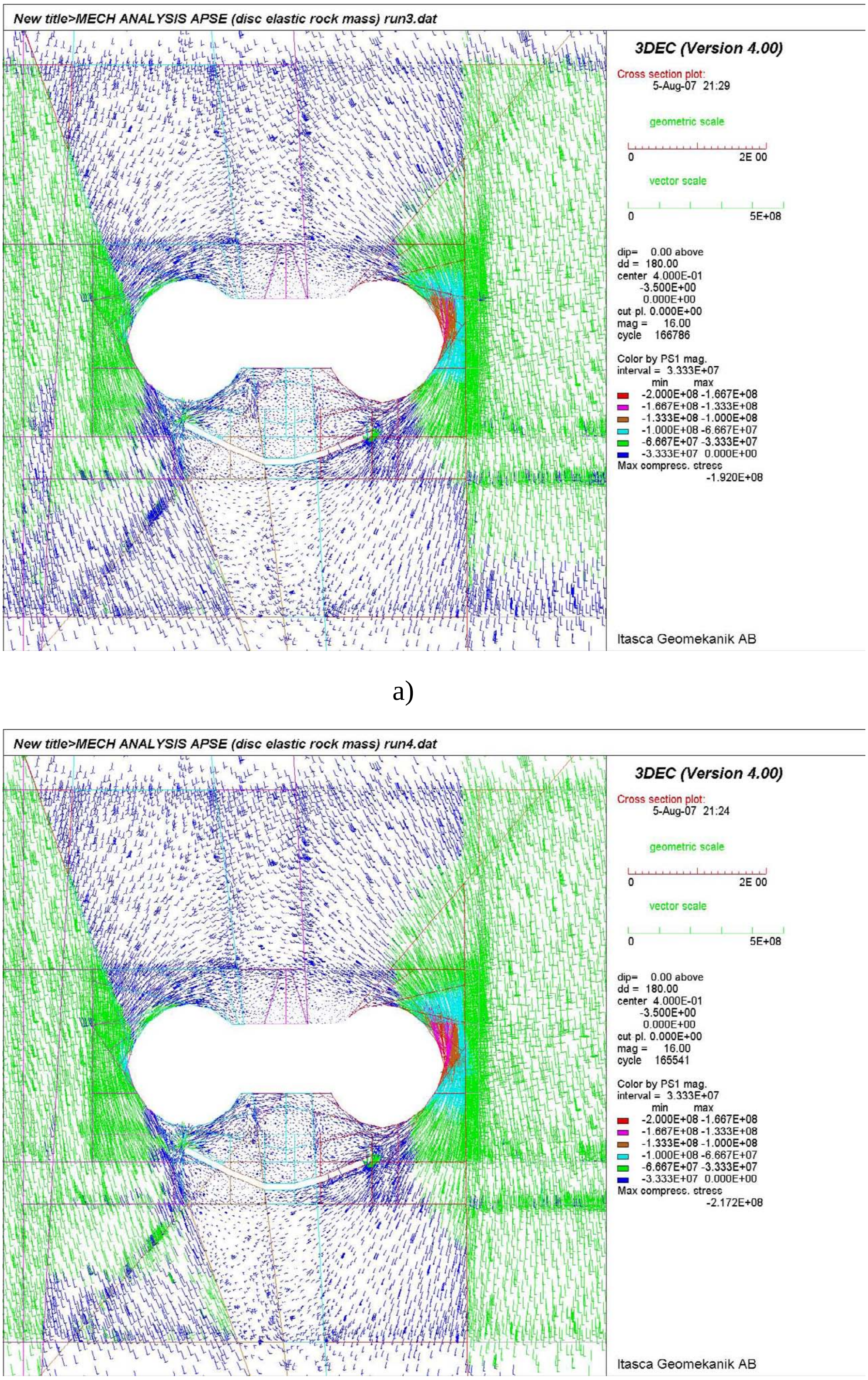

a)

b)

Figure H20. *Horizontal cross-section showing the projected principal stress at 3.5 m depth from the floor of the APSE tunnel after the pillar has been removed (Colors by magnitude of σ_1) for a) Run3 b) Run4.*

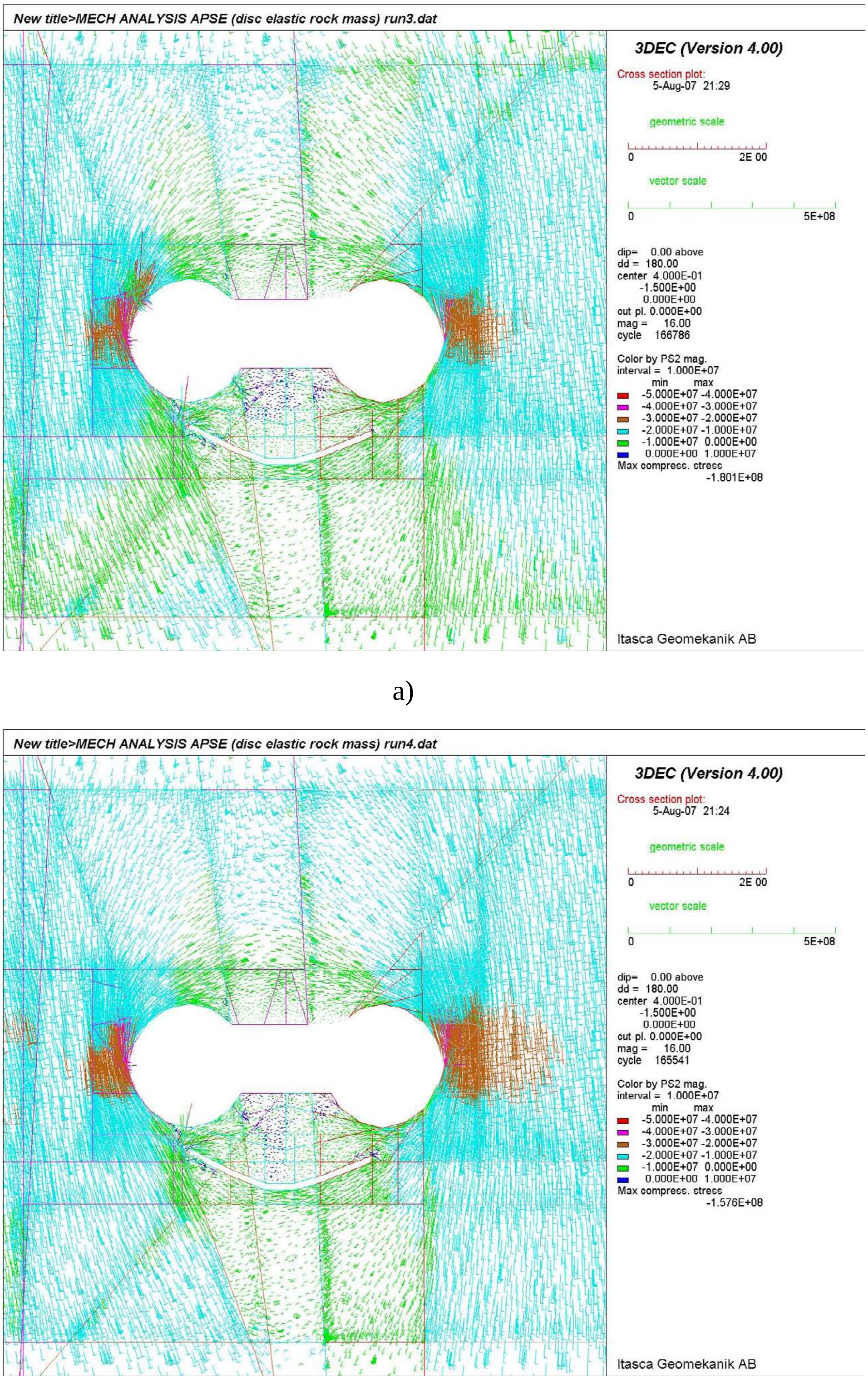

a)

b)

Figure H21. *Horizontal cross-section showing the projected principal stress at 1.5 m depth from the floor of the APSE tunnel after the pillar has been removed (Colors by magnitude of σ_2) for a) Run3 b) Run4.*

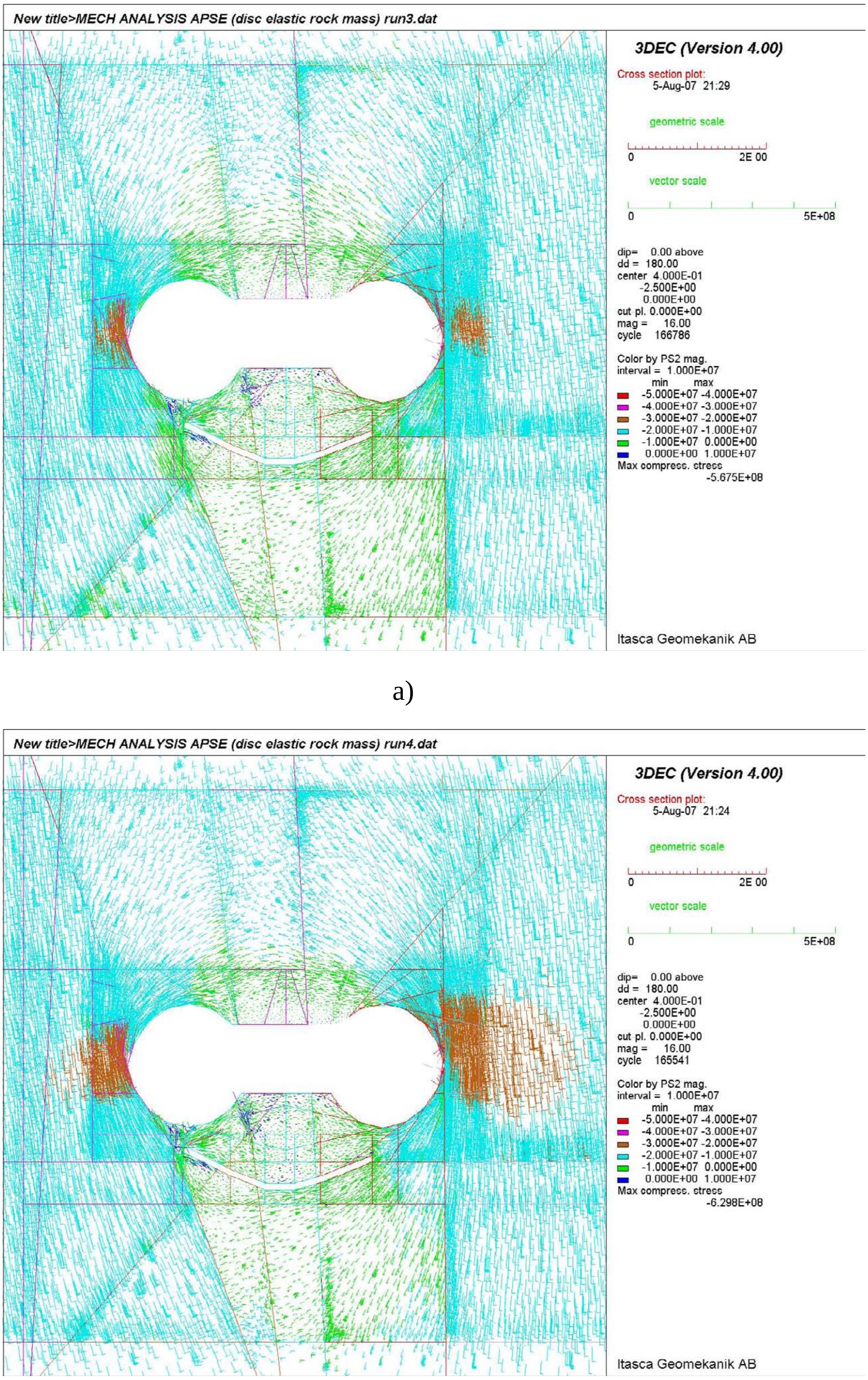

a)

b)

Figure H22. *Horizontal cross-section showing the projected principal stress at 2.5 m depth from the floor of the APSE tunnel after the pillar has been removed (Colors by magnitude of σ_2) for a) Run3 b) Run4.*

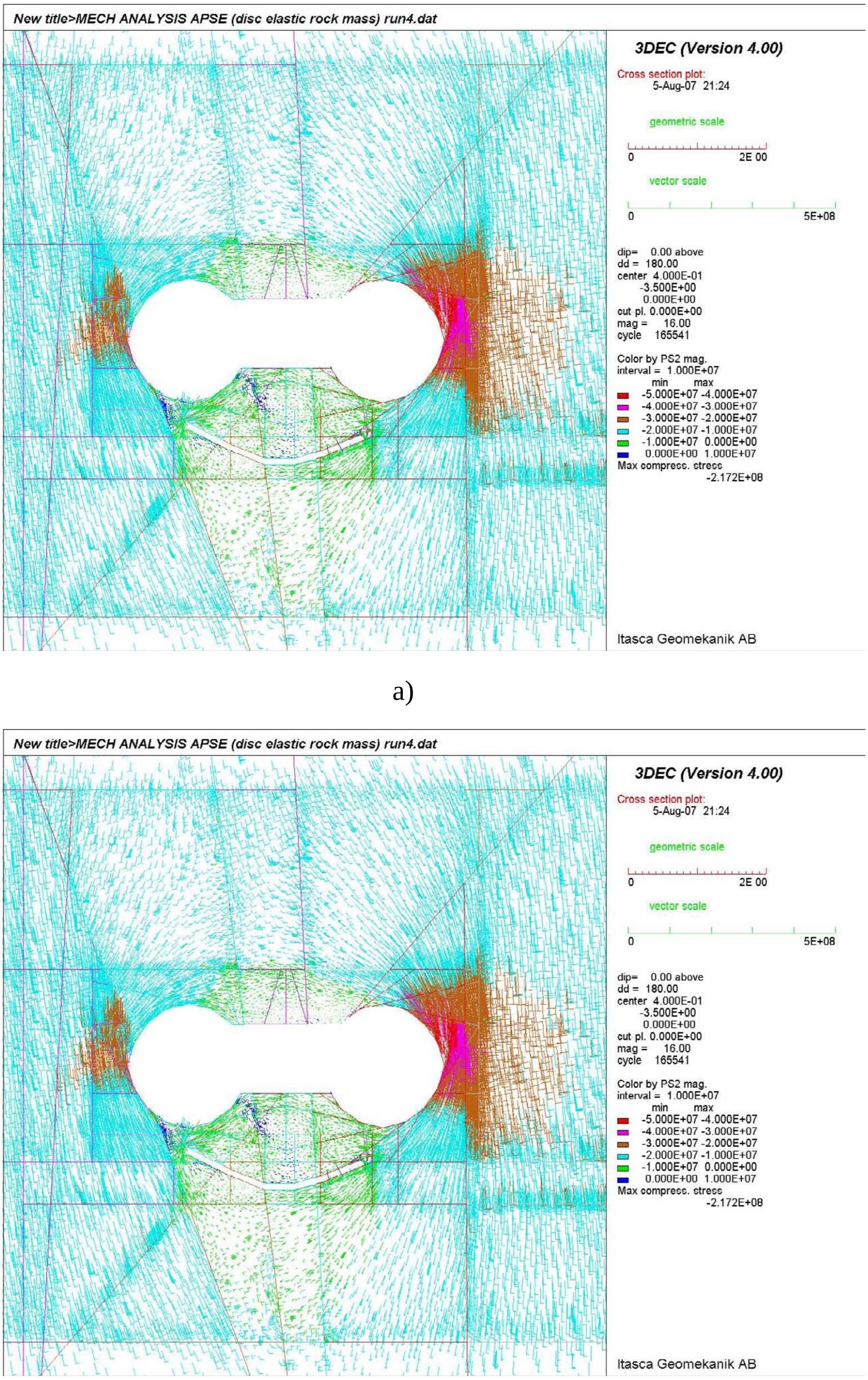

a)

b)

Figure H23. *Horizontal cross-section showing the projected principal stress at 3.5 m depth from the floor of the APSE tunnel after the pillar has been removed (Colors by magnitude of* σ_2*) for a) Run3 b) Run4.*

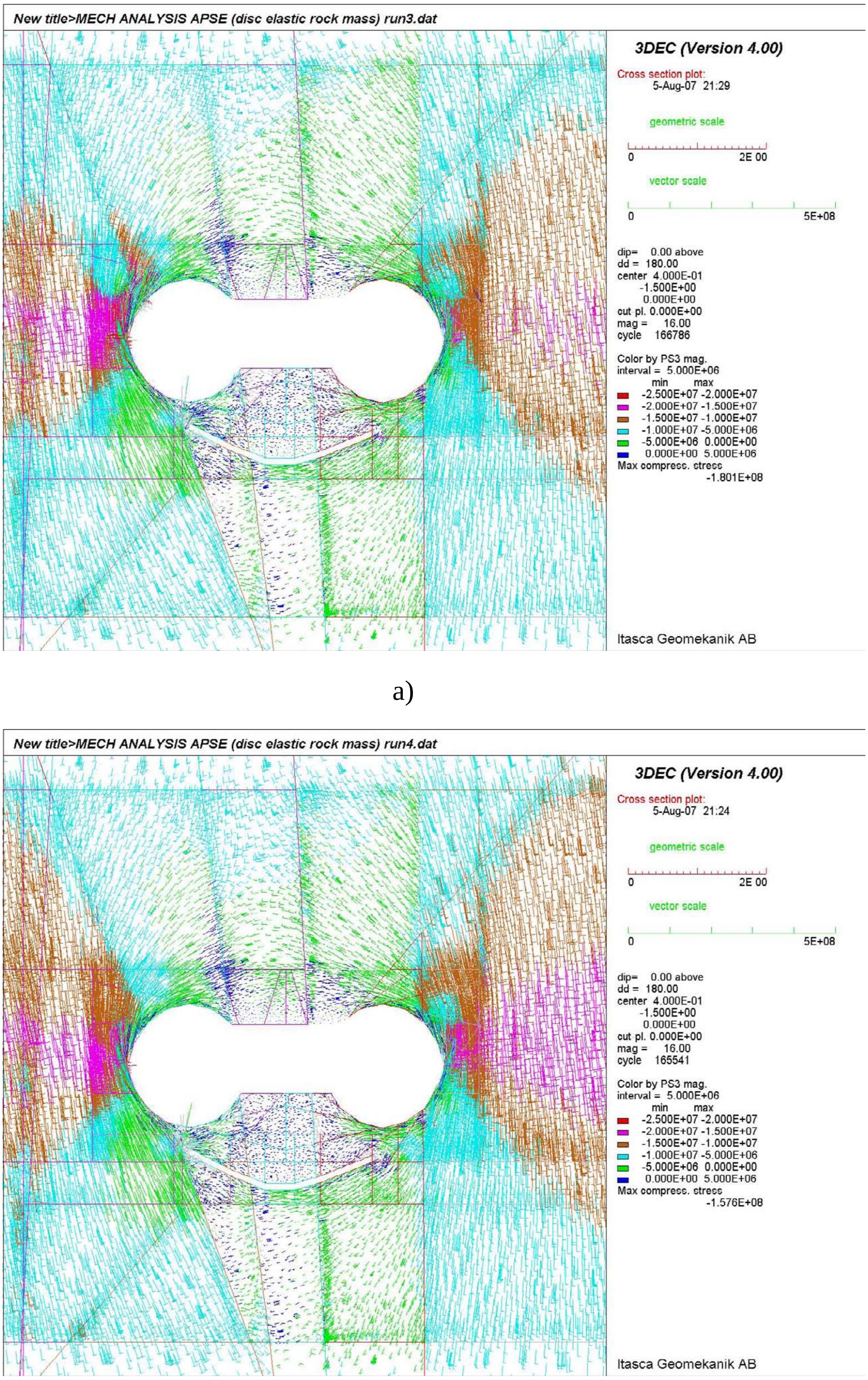

a)

b)

Figure H24. *Horizontal cross-section showing the projected principal stress at 1.5 m depth from the floor of the APSE tunnel after the pillar has been removed (Colors by magnitude of σ_3) for a) Run3 b) Run4.*

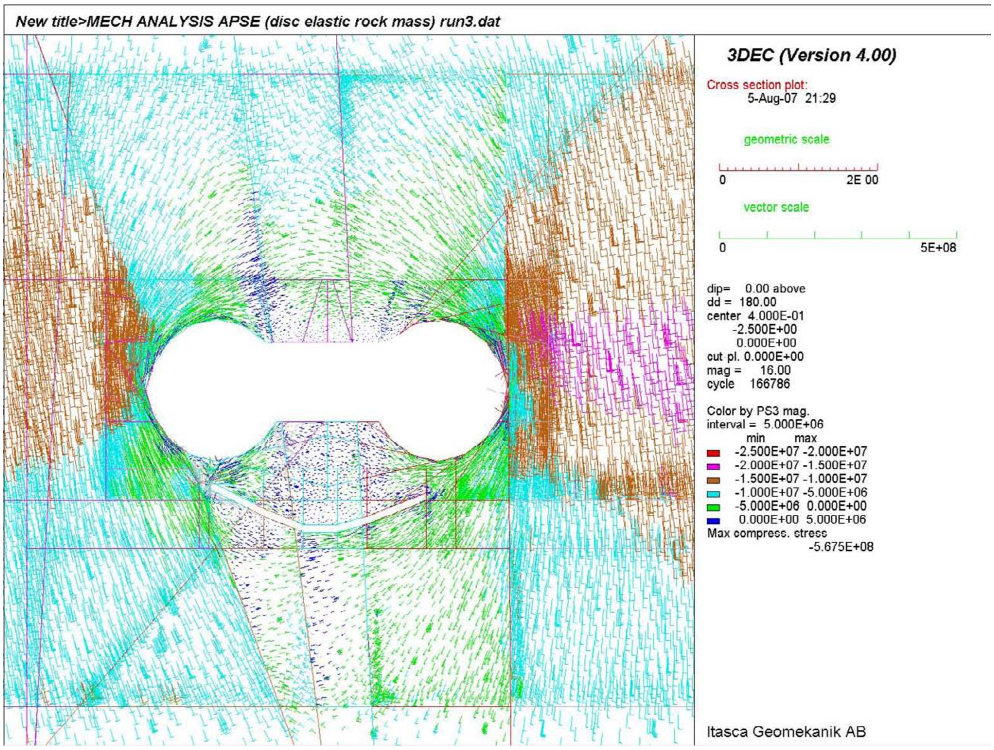

a)

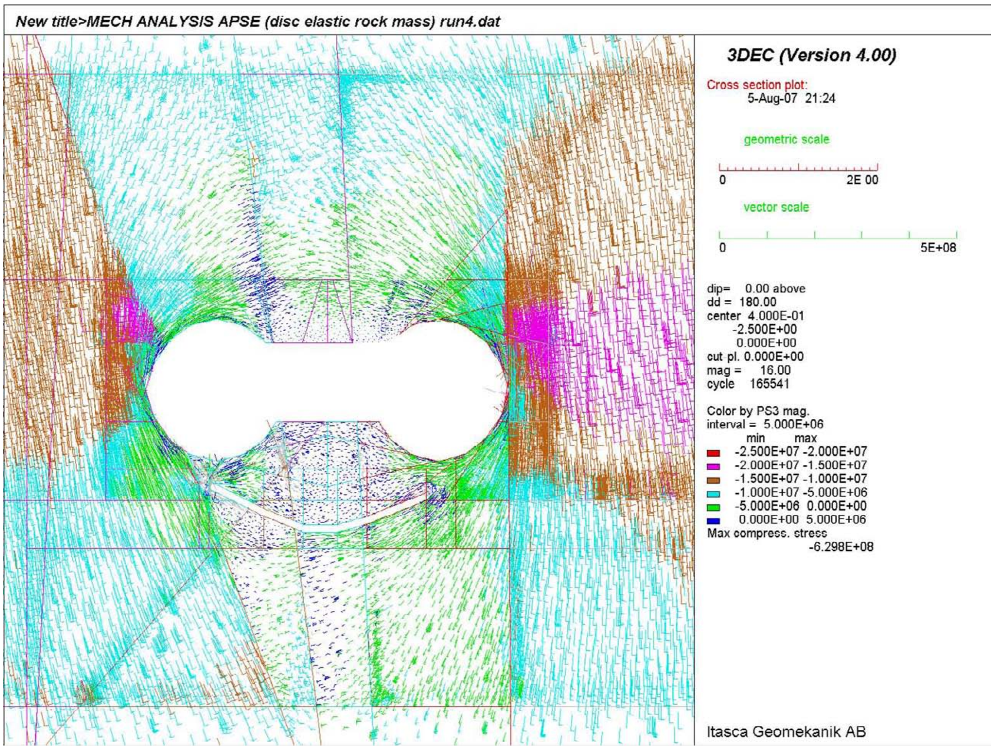

b)

Figure H25. *Horizontal cross-section showing the projected principal stress at 2.5 m depth from the floor of the APSE tunnel after the pillar has been removed (Colors by magnitude of* σ_3*) for a) Run3 b) Run4.*

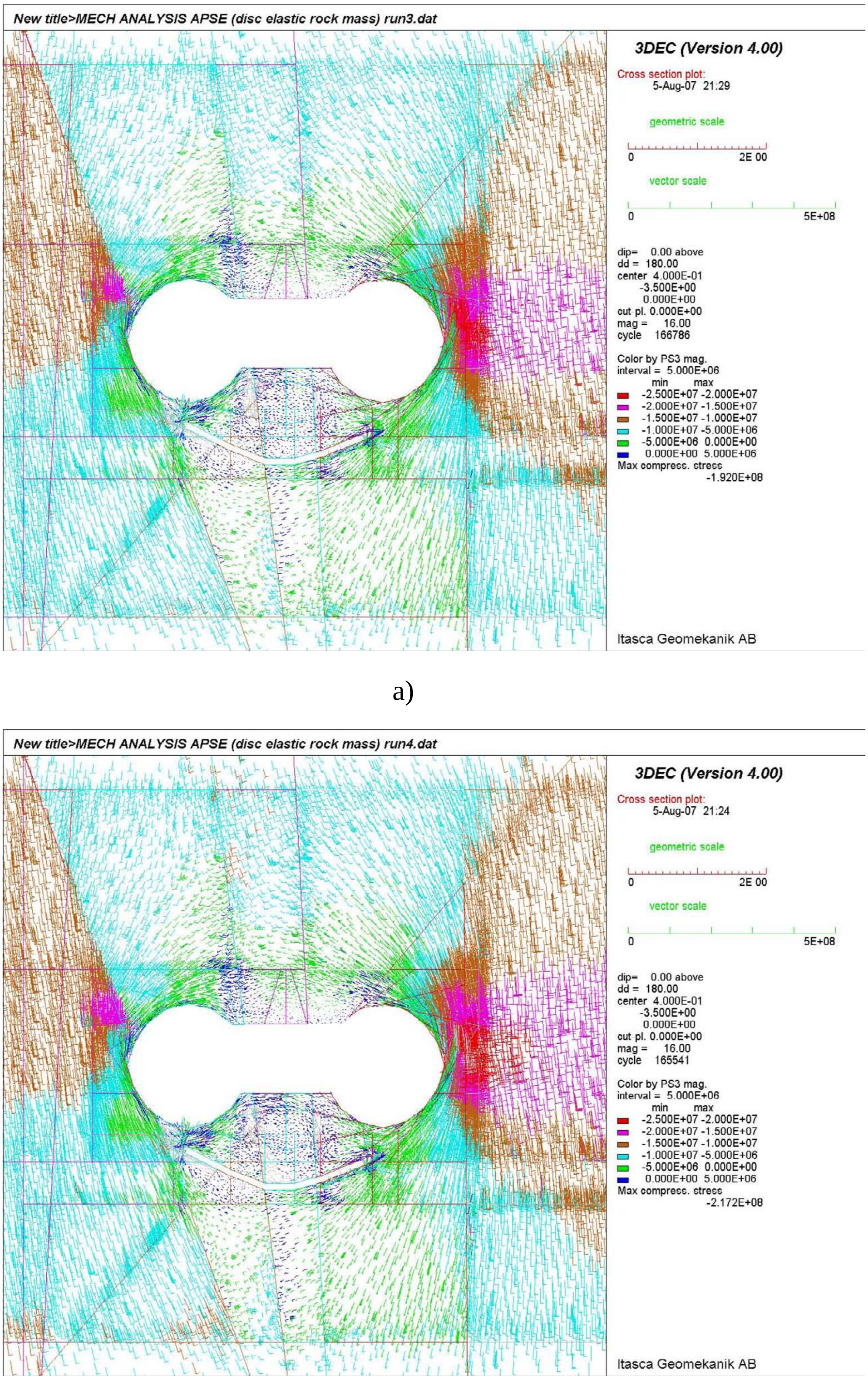

a)

b)

Figure H26. *Horizontal cross-section showing the projected principal stress at 3.5 m depth from the floor of the APSE tunnel after the pillar has been removed (Colors by magnitude of σ_3) for a) Run3 b) Run4.*